

# **Development of a Universal Impeller Test Rig for Scaled Testing of High Performance Impellers**

by

**Luke C. Philogene**

In fulfilment of the academic requirements for the degree of Master of Science in Mechanical Engineering, College of Agriculture, Engineering and Science, University of KwaZulu-Natal.

EXAMINER'S COPY

Supervisor: Prof. Graham D.J. Smith

Co-supervisor: Mr. Michael Brooks

Prof. Jeff Bindon

Dr. Glen Snedden (CSIR)

## DECLARATION – PLAGIARISM

I, Luke Charles Philogene, declare that

1. The research reported in this thesis, except where otherwise indicated, is my original research.
2. This thesis has not been submitted for any degree or examination at any other university.
3. This thesis does not contain other persons' data, pictures, graphs or other information, unless specifically acknowledged as being sourced from other persons.
4. This thesis does not contain other persons' writing, unless specifically acknowledged as being sourced from other researches. Where other written sources have been quoted, then:
  - a. Their words have been re-written but the general information attributed to them has been referenced.
  - b. Where their exact words have been used, then their writing has been placed in italics and inside quotation marks, and referenced.
5. This thesis does not contain text, graphics or tables copied and pasted from the Internet, unless specifically acknowledged, and the source being detailed in the thesis and in the References sections.

Signed:

Date:

.....

Mr. Luke C. Philogene

As the candidate's supervisor I have approved this dissertation for submission.

Signed:

Date:

.....

Prof. Graham D.J. Smith

## **ACKNOWLEDGEMENTS**

To my primary supervisor, Prof. Graham D.J. Smith, your invaluable insight and assistance during the duration of this work is much appreciated. Thanks to my co-supervisors for their input towards this work, in particular Mr. Michael Brooks who initially gave me the opportunity of pursuing this research.

A big thanks must go to Mr. Strini Govender and the rest of the staff in the UKZN mechanical engineering workshop for the aid during the construction of the test rig.

This work was funded by the Armscor BALLAST program.

## ABSTRACT

This dissertation presents the validation of a universal impeller test rig, designed by the author and constructed at the University of KwaZulu-Natal (UKZN). The research was conducted as part of UKZN's Aerospace Systems Research Group's (ASReG) work into liquid rocket propulsion. The rig will be used to evaluate the performance of an impeller, developed as part of ASReG's research, for use in a hypothetical launch vehicle's fuel turbopump. Head rise versus flow rate characteristics, as well as cavitation performance will be assessed by the rig. The power requirements of the impeller necessitated the reduction in rotational speed and geometric size of the test case. Scaling laws and dimensionless numbers were used to predict the test case performance based on the design performance. This predicted performance was then used to determine specific parameters used in the rig design.

Validation of the rig and testing procedures was performed using a standard industrial KSB ETA 125 – 200 centrifugal pump, by comparing the experimental results with those of the supplier. Head rise characteristics were determined by measuring the change in pressure between the inlet and discharge of the pump and then plotted against the flow rate for varying system heads. Cavitation performance was assessed by decreasing the inlet pressure while maintaining a constant flow rate. This was performed at various flow rates within the range of operation. Head breakdown, vibration and noise levels, both in the time and frequency domains, were used to assess the cavitation performance.

The head rise versus flow characteristics of the pump, determined on the rig, showed good agreement with the supplier's data. Cavitation performance, determined by head breakdown, was also in accordance with the supplier. It was found that both the vibration and general noise levels increased, indicating the presence of cavitation, before any head breakdown was detected. By monitoring the level of the high frequency noise in particular,  $> 10$  kHz, the presence of cavitation was detected at a significantly higher inlet pressure than would be suggested by the head breakdown approach.

## TABLE OF CONTENTS

DECLARATION – PLAGIARISM.....	ii
AKNOWLEDGEMENTS.....	iii
ABSTRACT.....	iv
TABLE OF CONTENTS.....	v
LIST OF FIGURES .....	viii
LIST OF TABLES.....	xi
NOMENCLATURE.....	xii
CHAPTER 1: Introduction.....	1
1.1. Aim and Objectives:.....	2
CHAPTER 2: Literature Review .....	4
2.1. Rocket propulsion: .....	4
2.1.1. Fundamentals of rocket propulsion:.....	4
2.1.2. Types of rocket engines: .....	5
2.1.3. Liquid rocket engine configurations: .....	6
2.2. Pipe flow: .....	7
2.2.1. Parameters and basic equations:.....	7
2.2.2. Major and minor losses: .....	8
2.2.3. System head: .....	11
2.3. Non-Cavitating Pump Performance: .....	12
2.3.1. Principles of Operation: .....	12
2.3.2. Secondary Flows: .....	15
2.3.3. Dimensionless Parameters: .....	16
2.3.4. Pump operation: .....	17
2.4.5. Scaling:.....	18
2.4. Suction Performance: .....	19
2.4.1. Suction and Cavitation Parameters: .....	19

2.4.2. Cavitation Inception: .....	21
2.4.3. Types of Cavitation: .....	24
2.4.4. Cavitation Effects: .....	27
2.5. Methods for Detecting Cavitation: .....	28
2.5.1. Performance Degradation: .....	28
2.5.2. Visual Inspection: .....	30
2.5.3. Pressure, Vibration and Noise: .....	30
2.6. Cavitation Test Facilities: .....	33
2.6.1. Aerospace Corporation Test Facility (Ehrlich et al, 2009): .....	33
2.6.2. Pisa Cavitation Test Loop (Rapposelli et al, 2002): .....	34
<b>CHAPTER 3: Test Impeller Performance and Scaling</b> .....	<b>36</b>
3.1. Hypothetical launch vehicle: .....	36
3.1.1. Proposed mission Parameters: .....	36
3.1.2. Launch vehicle configuration: .....	37
3.1.3. Fuel turbopump requirements: .....	41
3.2. Full Scale Impeller Design and Performance: .....	43
3.2.1. Design methodology: .....	44
3.2.2. Final design geometry: .....	45
3.2.3. Performance Data: .....	46
3.3. Scaled Test Impeller: .....	49
3.3.1. Scaling criteria: .....	49
3.3.2. Test impeller performance: .....	53
<b>CHAPTER 4: Test Rig Design</b> .....	<b>55</b>
4.1. Objectives and requirements: .....	55
4.1.1. Testing objectives and requirements: .....	55
4.1.2. Design requirements: .....	56
4.2. Rig Design: .....	56
4.2.1. Drive system arrangement: .....	56
4.2.2. Pipe system: .....	62

4.2.3. Sensors and data acquisition system: .....	67
4.4. Test Rig Operational Envelope: .....	71
CHAPTER 5: Experimental Results .....	75
5.1. KSB ETA 125 – 200 Data:.....	75
5.2. KSB Pump Test Procedure: .....	77
5.3. Experimental Results: .....	78
5.3.1: Performance characteristic curve:.....	78
5.4.2. Effect of cavitation on head rise and determining $NPSH_{3\%}$ : .....	79
5.4.3: Cavitation detection using vibration: .....	83
5.4.4: Cavitation noise analysis:.....	85
CHAPTER 6: Conclusion and Future Work.....	90
6.1. Conclusion: .....	90
6.2: Future Work:.....	93
REFERENCES: .....	95
APPENDIX A: Comparative Data for Hypothetical Launch Vehicle Sizing and Fuel Turbopump Requirements.....	99
APPENDIX B: Specifications of Instrumentation and KSB Pump .....	102
APPENDIX C: Preliminary Scaling Calculations .....	108
APPENDIX D: 1D Test Rig Calculations .....	112
APPENDIX E:Experimental Data and Calculations.....	121

## LIST OF FIGURES

Figure 2.1: Types of rocket engine cycles (Haidn, 2008). .....	7
Figure 2.2: Moody diagram used to determine the Darcy friction factor (Moody, 1944). .....	9
Figure 2.3: Summary of loss coefficients for various pipe fittings (Kudela, 2012). .....	10
Figure 2.4: Parameters used to define the system head. ....	11
Figure 2.5: Generalized impeller blade geometry (Brennen, 1994). .....	12
Figure 2.6: Developed meridional surface and velocity triangle (Brennen, 1994). .....	13
Figure 2.7: Incidence and deviation angles (Brennen, 1994). .....	14
Figure 2.8: Sketch of the secondary flows present in an impeller (adapted from Makay, 1980). .....	15
Figure 2.9: Pump, compressor and turbine impeller types with corresponding specific speed (Sabersky et al, 1989). .....	17
Figure 2.10: Pump operating point, defined by the system head. ....	18
Figure 2.11: Generalized inlet configuration with the relevant NPSH parameters defined. ....	20
Figure 2.12: NPSH <sub>r</sub> trend for a centrifugal pump (Shiels, 1998). .....	21
Figure 2.13: The effect of nuclei on cavitation inception on the same headform (Lindgren and Johnsson, 1966, Johnsson, 1969). .....	22
Figure 2.14: Thermodynamic effect on cavitation performance (Chivers, 1969). .....	24
Figure 2.15: Typical forms of cavitation for an unshrouded axial impeller (Brennen, 1994). ...	25
Figure 2.16: Travelling bubble cavitation on NACA hydrofoil (Kermeen, 1956), and blade cavitation in a centrifugal pump (Sloteman et al, 1991). .....	25
Figure 2.17: Vortex cavitation on a ship impeller (Brennen, 1994), and backflow cavitation in a scaled SSME low pressure LOX turbopump (Braisted, 1979). .....	26
Figure 2.18: Rotating cavitation in a centrifugal pump at off-design conditions (Hofmann, 2001). .....	26
Figure 2.19: Cavitation damage (Gülich and Rösch, 1988). .....	28
Figure 2.20: Effect of cavitation on head rise (Brennen, 1994). .....	29
Figure 2.21: Effect of rotating cavitation on the head rise of two inducers (Kamijo et al, 1977). .....	29
Figure 2.22: Schematic of an optical system used for visual cavitation detection (Baldassarre et al, 1998). .....	30
Figure 2.23: Noise frequency spectrum showing the difference between non-cavitating and cavitating conditions (Čudina, 2002). .....	31
Figure 2.24: Noise level and head rise as a function of cavitation number for a centrifugal pump (adapted from McNulty and Pearsall, 1979). .....	32



Figure 2.25: Vibration levels and head rise as a function of $NPSH_a$ for a centrifugal pump (Černetič et al, 2008).....	32
Figure 2.26: Schematic of the Aerospace Corporation inducer test facility (Ehrlich et al, 2009). .....	34
Figure 2.27: Schematic of the Pisa cavitation test loop (Rapposelli et al, 2002).....	35
Figure 3.1: Turbopump shaft arrangements (Sobin and Bissel, 1974).....	37
Figure 3.2: Propellant feed system schematic with calculated parameters (adapted by Smyth, 2014 from Parsely and Zhang, 2004).....	42
Figure 3.3: 3D model of the final fuel turbopump impeller design (Smyth, 2014). ....	45
Figure 3.4: Head rise versus flow rate of the fuel turbopump impeller (Smyth, 2014). ....	47
Figure 3.5: Efficiency versus flow rate of the fuel turbopump impeller (Smyth, 2014).....	47
Figure 3.6: Power versus flow rate for the fuel turbopump impeller (Smyth, 2014).....	48
Figure 3.7: $NPSH_r$ versus flow rate for the fuel turbopump impeller (Smyth, 2014). ....	48
Figure 3.8: Scaled head as a function of rotational speed and geometric scaling factor.....	51
Figure 3.9: Scaled flow rate as a function of rotational speed and geometric scaling factor. ....	51
Figure 3.10: Scaled power as a function of rotational speed and geometric scaling factor. ....	52
Figure 3.11: Scaled $NPSH_r$ as a function of rotational speed and geometric scaling factor. ....	52
Figure 3.12: Manufactured scaled test impeller, on left, and full scale impeller (Smyth, 2014).53	
Figure 4.1: Uchida hydraulic pump and electric drive motor. ....	57
Figure 4.2: Cross line relief manifold where overheating occurred. ....	58
Figure 4.3: Electrical control circuitry with replacement off breaker. ....	59
Figure 4.4: Hydraulic motor, gearbox and motor assembly.....	59
Figure 4.5: DC motor lead screw arrangement for the Uchida swashplate angle control.....	61
Figure 4.6: Panel containing motor speed display and swashplate angle control switches. ....	61
Figure 4.7: Gearbox polygon shaft profile with defining equations. ....	62
Figure 4.8: Supply tank with base to raise its level. The inlet pipe enters from the bottom and the discharge pipe enters from the top. ....	63
Figure 4.9: Effect of inlet pipe length and diameter on $NPSH_a$ , used to select an adequate pipe diameter.....	64
Figure 4.10: 3D model of the test rig layout. ....	65
Figure 4.11: Position of the valves. The inlet valve is at the bottom and the two discharge valves at the top.....	65
Figure 4.12: A section of the inlet and discharge piping. Holes cut through the wall can be seen on the left. Supports for the inlet line (bottom) and discharge line (top) can be seen.....	66
Figure 4.13: Instrumentation section of the test rig. ....	68
Figure 4.14: Flow meter clamped between flanges in the discharge line. ....	68

Figure 4.15: NI DAQ hardware, power supply, flow meter control box and RTD transmitter used for data acquisition. ....	69
Figure 4.16: Front panel of LabVIEW virtual instrument. ....	70
Figure 4.17: Block diagram of LabVIEW virtual instrument. ....	70
Figure 4.18: Pump inlet pressure as a function of flow rate. ....	71
Figure 4.19: $NPSH_a$ and $NPSH_r$ for the test rig and impeller. ....	72
Figure 4.20: System head curve for the test rig, with no throttling of the inlet or discharge line. ....	73
Figure 4.21: Operational envelope of the test rig. Test impeller performance characteristic curves shown in blue. Design point is shown in green for all flow rates considered. $NPSH_a$ , maximum pressure and system head limits are shown in red. Critical test points are shown in black. ....	74
Figure 5.1: KSB ETA 125 - 200 performance data.....	76
Figure 5.2: Measured pump characteristic curve. ....	79
Figure 5.3: Head rise versus inlet pressure for various flow rates. ....	80
Figure 5.4: Head rise versus $NPSH$ for various flow rates. ....	81
Figure 5.5: Experimental and supplier $NPSH_{3\%}$ curves. ....	82
Figure 5.6: RMS vibration velocity versus $NPSH$ for the seven flow rates tested. Red lines represent the non-cavitating vibration levels. Black lines represent the value of $NPSH$ at which vibration increases due to cavitation. ....	84
Figure 5.7: $NPSH_r$ based on vibration and head rise versus flow rate. ....	85
Figure 5.8: Time domain signal comparisons at non-cavitating and cavitating conditions. The unfiltered signal is shown first followed by low, band and high pass filtered signals. ....	87
Figure 5.9: Difference in the frequency power spectrum at two different cavitation conditions. The unfiltered signal is shown first followed by low, band and high pass filtered signals. ....	87
Figure 5.10: RMS noise levels and head as functions of $NPSH$ , for a flow rate of 5 l/s. ....	88
Figure 6.1: 3D model of proposed modification to the exiting pump housing to accept the scaled test impeller.....	93

## LIST OF TABLES

Table 3.1: Comparison of existing launch vehicle parameters. ....	39
Table 3.2: Summary of proposed launch vehicle parameters. ....	40
Table 3.3: Summary of the fuel turbopump performance parameters. ....	43
Table 3.4: Summary of the full scale and test impeller parameters. ....	54
Table 4.1: Summary of pipe lengths and fittings used the test rig design.....	66
Table A.1: Comparative Data for 2-Stage Lift Vehicles.....	100
Table A.2: Comparative Data for Kerosene Engines (Smyth, 2014).....	101
Table B.1: Type 42 flexible gear coupling specifications.....	105
Table B.2: A-10 pressure transducer specifications.....	105
Table B.3: S-10 pressure transducer specifications. ....	105
Table B.4: SAFMAG beta meter electromagnetic flowmeter specifications.....	106
Table B.5: PT 100 RTD and transmitter specifications. ....	106
Table B.6: Model 2400 vibration sensor specifications. ....	106
Table C.1: Scaled impeller performance data used to compare the effects of rotational speed and geometric scaling factor. ....	110
Table D.1: Scaled $NPSH_r$ data for the test impeller used to compare with $NPSH_a$ . ....	119
Table D.2: Scaled performance data for test impeller used to plot operational envelope.....	119
Table D.3: Scaled design operating point used to plot operational envelope. ....	120
Table E.1: Pump curve experimental data. ....	132
Table E.2: Supplier and experimental $NPSH_{3\%}$ and $NPSH_r$ based on vibration, data.....	133
Table E.3: Suction performance experimental data for 2 l/s.....	133
Table E.4: Suction performance experimental data for 3 l/s.....	134
Table E.5: Suction performance experimental data for 4 l/s.....	134
Table E.6: Suction performance experimental data for 5 l/s.....	135
Table E.7: Suction performance experimental data for 6 l/s.....	136
Table D.8: Suction performance experimental data for 7 l/s. ....	136
Table D.9: Suction performance experimental data for 8 l/s. ....	137

## NOMENCLATURE

### Symbols

a	Hub-to-tip ratio
A	Area [m <sup>2</sup> ]
$\alpha$	Incidence angle [°]
B	Blade height [m]
$\beta$	Flow angle [°]
$\beta_b$	Blade angle [°]
D	Diameter [m]
$\delta$	Deviation angle [°]
e	Surface roughness [m], eccentricity [m]
E	Secondary flow blockage
$\eta$	Efficiency
f	Darcy friction factor
F	Force [N]
g	Acceleration due to gravity [m/s <sup>2</sup> ]
h	Head [m]
$h_f$	Minor friction losses [m]
$h_F$	Major friction losses [m]
$h_{loss}$	Total friction losses [m]
H	Pump head rise [m]
$I_{sp}$	Specific impulse [s]
$K_L$	Friction loss coefficient

L	Pipe length [m]
$\lambda$	Exit swirl parameter
$\dot{m}$	Mass flow rate [kg/s]
$m_i$	Initial mass [kg]
$m_p$	Propellant mass [kg]
$m_s$	Stage dry mass [kg]
$M_f$	Mass fraction
n	Rotational speed [rpm]
N	Specific speed
$N_{ss}$	Suction specific speed
$N_{ss}'$	Corrected suction specific speed
$\Omega$	Rotational speed [rad/s]
p	Pressure [Pa]
$p^T$	Total pressure [Pa]
$p_v$	Vapour pressure [Pa]
$\phi$	Flow coefficient
$\psi$	Head coefficient
Q	Volumetric flow rate [m <sup>3</sup> /s]
R	Ratio of initial-to-burnout mass, radius [m]
Re	Reynolds number
$\rho$	Density [kg/m <sup>3</sup> ]
$\sigma$	Cavitation number
$t_b$	Burn time [s]
T	Temperature [°C]

U	Tip speed [m/s]
v	Fluid velocity [m/s]
$\Delta V$	Increase in velocity [m/s]
w	Relative velocity [m/s]
$\dot{W}$	Power [W]

### Subscripts

1	Upstream, inlet
2	Downstream, outlet
a	Atmospheric
b	Blade
f	Fuel
fs	Free surface
H	Hub
i	Inception
m	Meridional, mean
o	Oxidiser
T	Tip
$\theta$	Tangential, circumferential

### Abbreviations

ASReG	Aerospace Systems Research Group
BEP	Best Efficiency Point
CAD	Computer Aided Design

CFD	Computational Fluid Dynamics
DAQ	Data Acquisition
FFT	Fast Fourier Transform
GPS	Global Positioning System
LEO	Low Earth Orbit
LH <sub>2</sub>	Liquid Hydrogen
LOX	Liquid Oxygen
NASA	National Aeronautics and Space Administration
NB	Nominal Bore
NI	National Instruments
NPSH	Net Positive Suction Head
NPSH <sub>a</sub>	Net Positive Suction Head Available
NPSH <sub>r</sub>	Net Positive Suction Head Required
NPSH <sub>3%</sub>	Net Positive Suction Head 3%
O/F	Oxidiser-fuel ratio
OTR	Overberg Test Range
RMS	Root Mean Square
RP-1	Rocket Propellant 1 (Kerosene)
RTD	Resistance Temperature Detector
SF	Scale Factor
SSO	Sun Synchronous Orbit
TDH	Total Dynamic Head
UKZN	University of KwaZulu-Natal
USB	Universal Serial Bus

## **CHAPTER 1**

### **Introduction**

With the great potential that space holds it is no wonder that we as humans have found ways in which to exploit it to our advantage and in doing so change the way in which we live our lives. Man-made satellites have revolutionised our civilization and have become a vital component in all spheres of life; from our daily interactions to the functioning of multinational companies and governments. Satellite functions include communications, Global Positioning Systems (GPS), scientific experimentation and earth observation to name but a few. Access to this type of information and capabilities can have substantial benefits for development and quality of life on planet Earth.

Africa, in its developing state, stands to gain much from access to satellite resources. African leaders are beginning to identify the opportunities that space offers for the development of their nations. The development of human capital and technological competence with regards to satellite design, manufacture and operation have begun to increase on the continent. Currently a number of African countries own satellites in operation. The majority of these were developed with the aid of more mature space faring nations, however, there are African nations that have shown the ability to design and manufacture locally (Wood and Weigel, 2011). With the growing need for earth observation in Africa and an increasing potential for local design and manufacture, a new issue arises; how to get these satellites into orbit? Currently Africa does not possess any local capability to launch spacecraft into orbit. Reliance on foreign launch resources, which has been the approach up to now, is not ideal. Foreign nations plan missions to meet their own requirements and timelines and therefore place stringent requirements on any third party wanting to utilise their launch capacity. For the African context, this could have the potential to reduce the rate of development in the field and stall the acquisition of space resources for the continent in the near future.

With this issue of a local launch capacity in mind, the University of KwaZulu-Natal's (UKZN) Mechanical Engineering department has begun research into rocket propulsion through its Aerospace Systems Research Group (ASReG). It is the goal of ASReG to increase human capital and technological resources in the field of rocket propulsion. One aspect of this research is regarding liquid rocket propulsion. In this regard, a hypothetical launch vehicle was proposed from which various components could be investigated individually. The general configuration, propellant selection and mass flow rates were determined through a review of



existing launch vehicles, with specific mission requirements in mind. A propellant combination of kerosene (RP-1) and liquid oxygen (LOX) was selected. The first step towards the development of this hypothetical engine was to design the fuel turbopump impeller. Thrust requirements, propellant ratios, supply tank conditions and estimated feed line losses were determined and used to calculate the required performance of the impeller. The design process incorporated mean-line and quasi 3D analyses to arrive at an acceptable solution. The design, developed by Smyth (2014) has been manufactured and verification of its performance, to validate the methodology and design process, is the next step. To this end, CFD and experimental investigations into the impeller's performance are to be conducted.

It is the subject of this work to develop an experimental test rig capable of determining the experimental performance of the impeller, to better inform the design process. The large power requirements of the impeller necessitated geometry scaling and reduction of rotational speed for the test article. Using scaling laws the predicted performance of the test article was determined and used to inform the design of the test rig. Vital parameters were identified, the  $NPSH_a$  among others, to ensure that the rig could provide an adequate operational envelope to allow the required range of testing conditions. The design of the test rig allows for the testing of the non-cavitating performance of the impeller, to determine pump characteristic curve, as well as to assess the cavitation performance. The non-cavitating performance was determined by monitoring the change in pressure across the pump at various flow rates. Cavitation performance was assessed with three methods; the conventional 3% head drop approach, vibration levels and analysis of the noise generated by the cavitation process.

Apart from the design and construction of the test rig, this work presents the validation of the experimental procedures that will be used to assess the impeller's performance. The validation testing was conducted with the use of a KSB ETA 125-200 centrifugal pump. Results of the non-cavitating and  $NPSH_{3\%}$  tests were compared to the supplier's data to determine their accuracy. As vibration and sound levels are system dependent, they are non-standard means of detecting cavitation and do not form part of a supplier's data. Using the 3% approach as a baseline, these techniques were assessed to determine their effectiveness as tools in detecting the presence of cavitation in an impeller.

### **1.1. Aim and Objectives:**

The aim of this work is to provide a means by which the design of the fuel turbopump impeller can be experimentally evaluated. This will allow the design methodology to be assessed and

modified where required to provide a more robust and acceptable solution. Improvements to, and validation of, the design methodology will aid future designs efforts and help to build technological competence in the field.

To achieve the aim of the research, the following objectives had to be met:

- Design and construct a fluid power system, capable of meeting the hydraulic, mechanical and power requirements of the test impeller.
- Identify the parameters and experimental techniques used to define and evaluate the hydraulic performance of an impeller.
- Provide the required instrumentation and systems to implement these experimental techniques.
- Validate the experimental techniques implemented to ensure accuracy and reliability.

## CHAPTER 2

### Literature Review

#### 2.1. Rocket propulsion:

##### 2.1.1. Fundamentals of rocket propulsion:

Like all propulsion systems, a rocket engine's function is to provide thrust in order to propel a mass. Thrust is measured in Newtons and is the force that a propulsion system exerts on the propelled body. All propulsion systems develop thrust through the reaction force generated by the acceleration of a mass, typically a fluid. While many types of rocket concepts exist, such as ion thrusters and nuclear rockets, only chemical rocket engines currently provide enough thrust to successfully escape earth's gravitational field and can therefore be used to propel launch vehicles. Chemical rocket engines, like jet engines, develop their thrust by expanding high pressure, high temperature gas through a nozzle. The high pressures and temperatures are as a result of combusting a fuel and an oxidiser. In conventional propulsion systems oxygen in the air serves as the oxidiser which is combusted with a fuel carried on-board the propelled vehicle. Rocket engines however are required to operate in a vacuum, where no air is present. This makes rockets unique as both the fuel and the oxidiser must be carried on-board the vehicle to allow for operation within a vacuum. The measure of the efficiency of a rocket is known as the specific impulse,  $I_{sp}$ . The specific impulse is defined as:

$$I_{sp} = \frac{F}{\dot{m}g} \quad [2.1]$$

where  $F$  is the thrust in Newtons,  $\dot{m}$  is the total propellant mass flow rate and  $g$  is acceleration due to gravity. The unit for specific impulse is seconds. Specific impulse can be determined for a vacuum or at sea level and describes how well the flow of propellants is converted into thrust.

The primary expression for a launch vehicle's performance is the Tsiolkovsky's rocket equation (Huzel and Huang, 1992), defined as:

$$\Delta V = gI_{sp} \ln(R) \quad [2.2]$$

where  $R$  is the ratio of the vehicle's initial to burn out mass, expressed as:

$$R = \frac{m_i}{m_i - m_p} \quad [2.3]$$

The required delta-V of a vehicle can be calculated using the work of Schilling (2001) and Townsend (1935) based on the specific mission parameters. This in turn can be used to select an appropriate specific impulse and R value for a particular vehicle design. The mass fraction of a rocket is defined as:

$$M_f = \frac{m_p}{m_p + m_s} \quad [2.4]$$

where  $m_p$  is the propellant mass and  $m_s$  is the stage dry mass. The engine burn time can be calculated from the propellant mass flow rate and total propellant mass as follows:

$$t_b = \frac{m_p}{\dot{m}_p} \quad [2.5]$$

### 2.1.2. Types of rocket engines:

Chemical rockets are categorised by the state in which their fuel and oxidiser are stored. There are three general categories; solid, liquid and hybrid rocket motors.

Solid rocket motors are the simplest type of rocket motor. These motors use a solid propellant grain, which is a mixture of fuel and oxidiser. The grain has a cavity formed down its centre that serves as the combustion chamber. Since combustion can only occur at an exposed surface of the grain, the shape and size of the cavity determines the thrust and duration of the burn. Due to their simplicity, high thrust and dense propellants, solid rocket motors provide the best thrust to mass ratio of all rocket motors. However, solid rocket motors cannot be shutoff once ignited and they have the lowest specific impulse of all rocket types. This limits their use to the first stage of launch vehicles and military applications such as missiles.

Hybrid rocket motors are a combination of the liquid and solid types. A solid fuel and liquid oxidiser are used to produce the thrust. In a similar way to solid rockets, the shape and size of the fuel grain cavity affects the developed thrust. Hybrids have an added measure of control by means of the oxidiser flow rate. This makes hybrids more versatile in their operation as they can be shutoff and restarted with the appropriate procedures and systems. Hybrids have a specific impulse between that of a solid and liquid rocket. Hybrids have not been extensively

used for space flight, however research into these types of rockets is ongoing and their applications may increase in the future.

In liquid rockets, liquid fuel and oxidiser are stored separately and combined in the combustion chamber. Liquid rockets are the most efficient, having the highest specific impulse, and versatile of all rocket motors. Control of the thrust can be achieved by varying the propellant flow rates to the combustion chamber. For this reason all current commercial launch vehicles are propelled by liquid rocket motors (Sutton, 2005). Liquid rocket motors are however, the most complex and costly of all the rocket types.

### **2.1.3. Liquid rocket engine configurations:**

Liquid rocket engines require large propellant mass flow rates, delivered at high pressures to the combustion chamber. As weight is of primary importance, pressurisation of the propellant tanks cannot be used, as this results in very thick and heavy tanks being required. High performance, high powered pumps are therefore used, driven by turbines (Mårtensson et al, 2008). To reduce the weight of these systems the turbopumps are run at high speeds, above 10000 rpm. This allows for the physical size to be reduced while still providing the required performance. The high rotational speed creates challenges in terms of the rotodynamics, stability and suction performance of the turbopump assembly.

The way in which the turbines are powered and the propellant is fed to the combustion chamber is referred to as the engine cycle. The engine cycle has a significant impact on the performance of the engine and the requirements of the turbines and pumps (Sobin and Bissel, 1974). There are many variations in engine cycles that have been used, however there are three main types; the gas generator, expander and staged combustion cycle, shown in Figure 2.1.

The gas generator cycle burns a small portion of the fuel and oxidiser flow in a gas generator which is then used to power the turbines. The discharge flow is then either dumped or routed into the nozzle to be expanded with the main flow. The engine cycle has reduced specific impulse, since part of the propellant mass flow is used in the gas generator and not to produce thrust. The gas generator cycle allows for lower output pressures from the pumps, as the turbine and combustion chamber are in parallel.

While all cycles use the propellants for nozzle cooling the expander cycle uses this heat input as the source of energy to power the turbines. This cycle requires a cryogenic fuel. Propellants are vaporised as they pass through the nozzle's cooling channels. The vapour is then passed

through the turbine where it is expanded to power the pump. This cycle is restricted by the amount of heat that can be extracted from the nozzle. Due to the ease at which cryogenic fuels vaporise, this cycle can easily be shutoff and restarted. Adding the long burn times achievable with this cycle makes it suitable for upper stage engines.

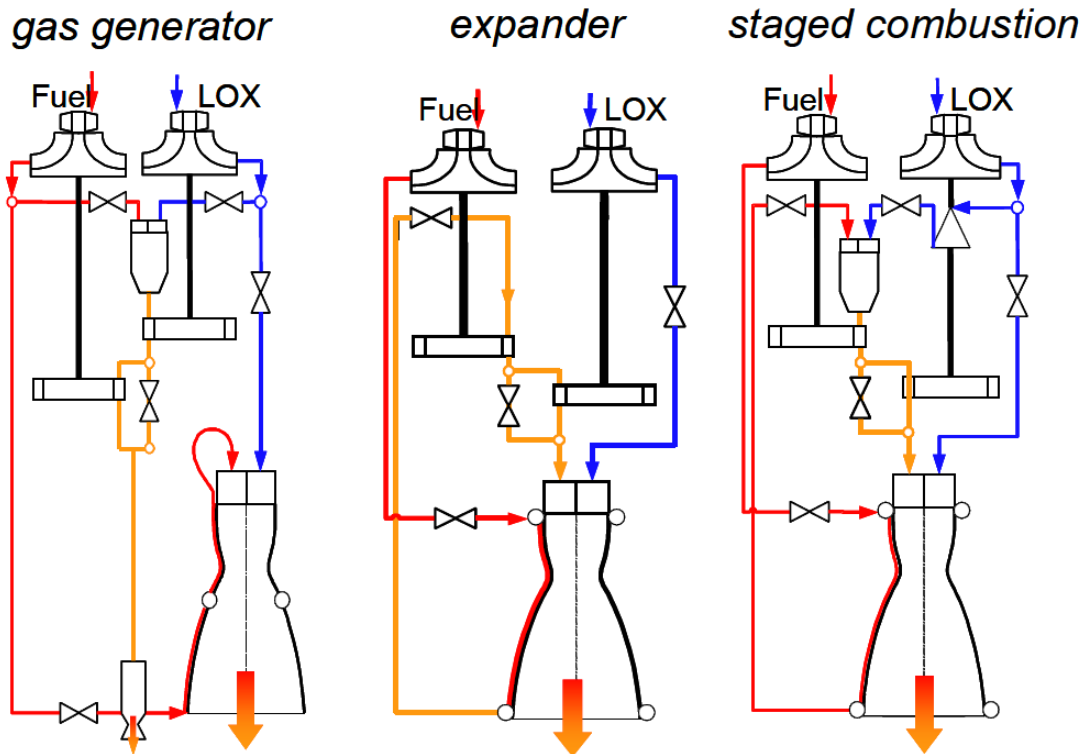


**Figure 2.1: Types of rocket engine cycles (Haidn, 2008).**

The staged combustion cycle is the most complicated cycle but provides the best performance. This cycle makes use of a pre-burner to provide the power for the turbine. Typically a fuel rich mixture is combusted and expanded through the turbine (Parsely and Zhang, 2004). The turbine exhaust is then fed into the combustion chamber where it is burned with the remaining oxidiser. Due to the temperature increase of the fuel, from the pre-burner, this cycle provides very high combustion chamber pressures which aid the performance.

## 2.2. Pipe flow:

### 2.2.1. Parameters and basic equations:

Bernoulli's equation describes the flow of an incompressible, inviscid fluid in a pipe or duct between two points. Bernoulli's equation is defined as:

$$\frac{p_1}{\rho g} + \frac{v_1^2}{2g} + h_1 = \frac{p_2}{\rho g} + \frac{v_2^2}{2g} + h_2 \quad [2.6]$$

The first term is the static head, the second term the dynamic head, both in metres, and the final term is the elevation above or below some reference point. The equation is a mechanical energy balance that compares the total pressures of a flow at two different positions.

For practical calculations incompressibility can be assumed, for low velocity liquid flows, however viscous effects must be considered. The effect of viscosity is to resist flow through friction, which extracts energy from the flow in terms of heat. In terms of Bernoulli's equation, this loss of energy can be represented as a pressure loss. Bernoulli's equation can be modified to incorporate this energy loss:

$$\frac{p_1}{\rho g} + \frac{v_1^2}{2g} + h_1 = \frac{p_2}{\rho g} + \frac{v_2^2}{2g} + h_2 + h_{\text{loss}} \quad [2.7]$$

The  $h_{\text{loss}}$  term on the right hand side accounts for the loss in energy, or pressure, as the fluid flows from point 1 to point 2.

### 2.2.2. Major and minor losses:

In order to determine the operating conditions of a piped system the losses of the system must be calculated. The losses in a piping system are divided into two categories; major and minor losses. Major losses refer to the friction losses that occur in straight sections of pipe. Minor losses are as a result of fittings and bends in the system. The naming of these losses are convention and do not refer to the impact on the system. A system may have larger minor losses than major ones, depending on the design and fittings installed.

The major friction loss in a pipe can be calculated using the Darcy-Weisbach equation as follows:

$$h_F = f \frac{L v^2}{D 2g} \quad [2.8]$$

From this equation, it can be seen that the major losses are related to the physical parameters of the pipe system, the length and diameter, as well as the velocity of the flow. The Darcy friction factor,  $f$ , is an empirical factor that must be determined for a particular system, flow rate and fluid. The Moody chart represents the empirical data used to determine the Darcy friction factor, based on Reynolds number and relative roughness (Moody, 1944), as seen in Figure 2.2.

The relative roughness is a function of the pipe material roughness and diameter. Empirical values for surface roughness,  $e$ , of the pipe material are used to calculate the relative roughness. The Reynolds number, used to define the level of turbulence in the flow, is critical in determining the Darcy friction factor, as turbulence and boundary layer development play a large role in the losses incurred.

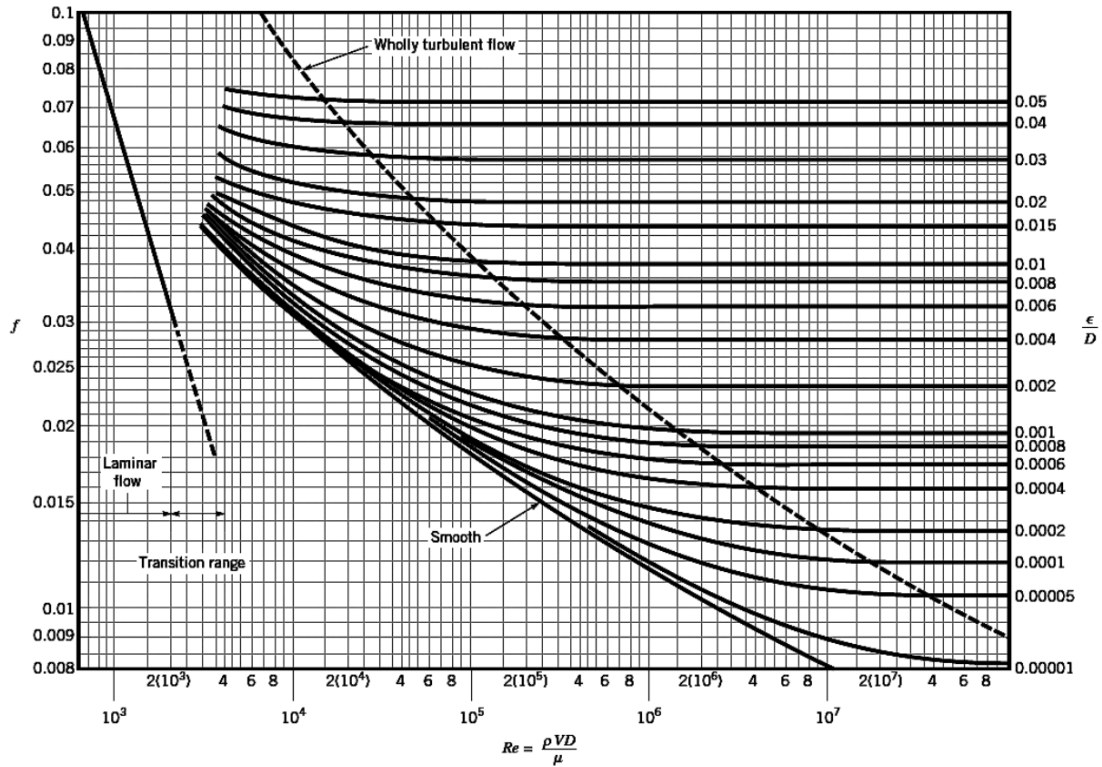


Figure 2.2: Moody diagram used to determine the Darcy friction factor (Moody, 1944).

The Colebrook equation uses all this empirical data to define a relationship between the Darcy friction factor, Reynolds number and the relative roughness (Colebrook, 1938-39). The equation is defined as:

$$\frac{1}{\sqrt{f}} = -2.0 \log \left( \frac{\epsilon/D}{3.7} + \frac{2.51}{Re\sqrt{f}} \right) \quad [2.9]$$

This equation is implicit in  $f$  and requires an iterative solution. Many approximations have been found for the Colebrook equation to allow for an explicit relationship for  $f$  and hence a simpler solution. These approximations are generally only applicable within certain ranges of Reynolds number. The Hagen-Poiseuille equation,  $f = 64/Re$ , defines the Darcy friction factor for laminar flow. This equation represents the straight line starting at the top left of the Moody diagram, Figure 2.2, and therefore only covers very specific flow conditions. Another approximation, known as the Haaland equation, provides an explicit relationship for  $f$  in turbulent flows



(Haaland, 1983), which is the most common type of piped flow. The Haaland equation is defined as:

$$\frac{1}{\sqrt{f}} = -1.8 \log \left[ \frac{6.9}{\text{Re}} + \left( \frac{e/D}{3.7} \right)^{1.11} \right] \quad [2.10]$$

Losses incurred at the inlet to pipes, bends, valves and other fittings are defined as minor losses. To determine the losses through these system components, empirical coefficients are used. The general expression for minor losses is:

$$h_f = K_L \frac{v^2}{2g} \quad [2.11]$$

The coefficient  $K_L$  is a dimensionless number and is specific to a particular fitting or component. For components such as valves this coefficient is dependent on the specific design. For standard fittings such as bends and tees, general coefficients have been determined. Figure 2.3 shows various fittings and their corresponding loss coefficients. For a system with multiple

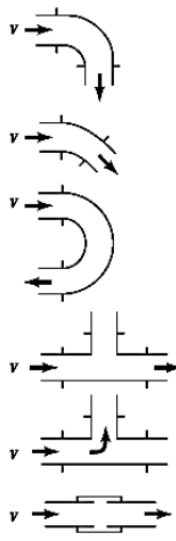
Loss Coefficients for Pipe Components $\left( h_L = K_L \frac{v^2}{2g} \right)$		
Component	$K_L$	
<b>a. Elbows</b>		
Regular 90°, flanged	0.3	
Regular 90°, threaded	1.5	
Long radius 90°, flanged	0.2	
Long radius 90°, threaded	0.7	
Long radius 45°, flanged	0.2	
Regular 45°, threaded	0.4	
<b>b. 180° return bends</b>		
180° return bend, flanged	0.2	
180° return bend, threaded	1.5	
<b>c. Tees</b>		
Line flow, flanged	0.2	
Line flow, threaded	0.9	
Branch flow, flanged	1.0	
Branch flow, threaded	2.0	
<b>d. Union, threaded</b>		
	0.08	
<b>e. Valves</b>		
Globe, fully open	10	
Angle, fully open	2	
Gate, fully open	0.15	
Gate, $\frac{1}{4}$ closed	0.26	
Gate, $\frac{1}{2}$ closed	2.1	
Gate, $\frac{3}{4}$ closed	17	
Swing check, forward flow	2	
Swing check, backward flow	$\infty$	
Ball valve, fully open	0.05	
Ball valve, $\frac{1}{3}$ closed	5.5	
Ball valve, $\frac{2}{3}$ closed	210	

Figure 2.3: Summary of loss coefficients for various pipe fittings (Kudela, 2012).

fittings, the loss coefficient must be determined for each one and then only can the total minor losses for the system be calculated. The sum of the major and minor losses gives the total loss of a system:

$$h_{\text{loss}} = h_F + h_f \quad [2.12]$$

### 2.2.3. System head:

When designing a pipe system or selecting a pump to operate in a system it is required that the resistance of the system be known. The system head curve describes a systems resistance to flow at a particular flow rate. Figure 2.4 shows a generalised pipe system with the parameters relevant to the system head shown.

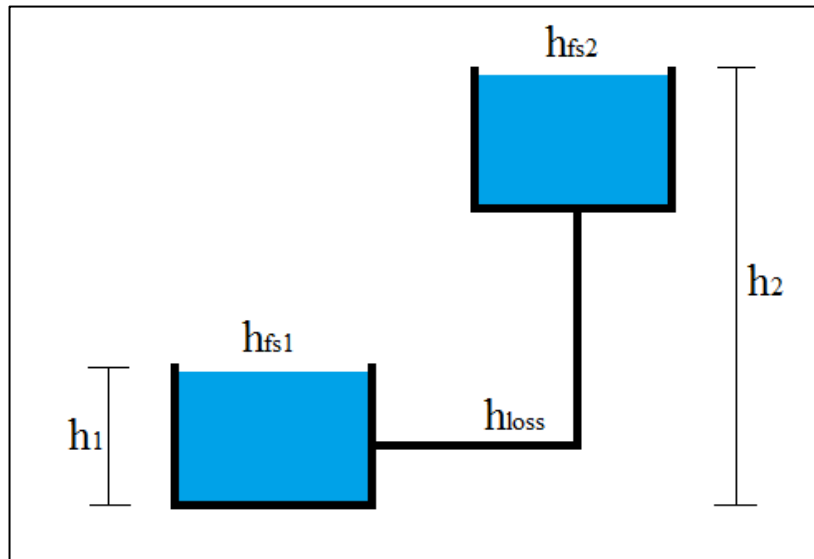


**Figure 2.4: Parameters used to define the system head.**

The system head curve, assuming flow from the bottom reservoir to the top, would be calculated as follows:

$$\text{System Head} = (h_{fs2} - h_{fs1}) + (h_2 - h_1) + h_{\text{loss}} \quad [2.13]$$

The first term in this equation is the difference between the pressures on the free surfaces of the fluid. The second term is the difference in height between the two reservoirs. Together these two terms provide the static component, or offset, of the system head curve. This component must be satisfied before any flow in the desired direction will be established. The last term is the resistance due to the friction developed in the flow. This term is proportional to the square of velocity and will therefore increase dramatically with an increase in flow rate. The system

head can be varied by changing any one of these parameters, however often the free surface pressures and heights are fixed by the requirements of the system. It is simplest to manipulate the loss term to match your system head to a particular value. This can be done by varying the physical parameters of the system, such as pipe length and diameter, however the most practical method is to install throttling valves in the system. This allows for the system head to be varied without changing the system's physical parameters.

### 2.3. Non-Cavitating Pump Performance:

#### 2.3.1. Principles of Operation:

The purpose of a pump is to impart energy to a fluid in order to create flow. In roto-dynamic pumps this energy is imparted to the fluid through the mechanical work done on it by a rotating impeller.

To begin analysing the operation of a roto-dynamic pump the basic geometry must be understood. Figure 2.5 shows a generalized impeller blade with the relevant geometric parameters defined. The inlet and outlet hub and tip radii are shown and are denoted by,  $R_{H1}$ ,  $R_{H2}$ ,  $R_{T1}$  and  $R_{T2}$ , respectively.  $B_1$  and  $B_2$  represent the blade inlet and outlet height. The

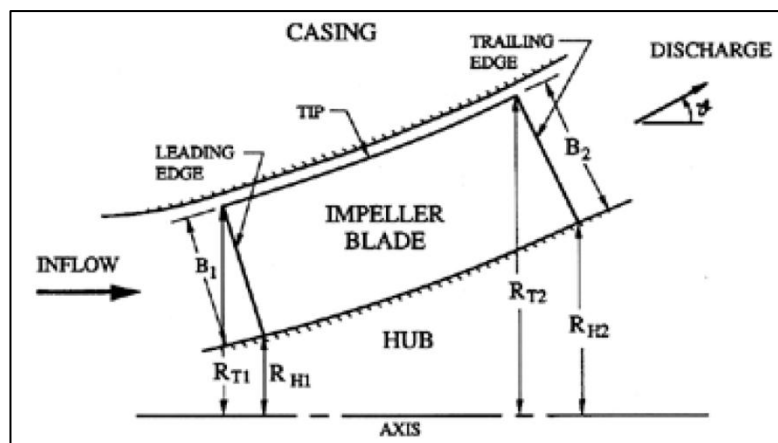


Figure 2.5: Generalized impeller blade geometry (Brennen, 1994).

discharge passage is inclined to the axis of rotation by an angle  $\vartheta$ . In pump design this angle falls in the range,  $0^\circ \leq \vartheta \leq 90^\circ$ , where  $0^\circ$  would represent a purely axial flow machine and  $90^\circ$  would be applicable to a centrifugal impeller. Mixed flow impellers would sit somewhere between these two extremes.

In analysing the flow through an impeller it is useful to define a meridional surface along the blade, as shown in Figure 2.6. This meridional surface represents a stream tube of width  $\delta n$  through the impeller. At any point along the surface the fluid velocity can be defined as a function of its radial position,  $v(r)$ . The fluid velocity relative to the blade velocity,  $\Omega r$ , is denoted by  $w$ . The velocity and relative velocity vectors have components in the meridional and circumferential directions and are denoted by  $v_m$ ,  $w_m$ ,  $v_\theta$  and  $w_\theta$  respectively, as shown in Figure 2.6.

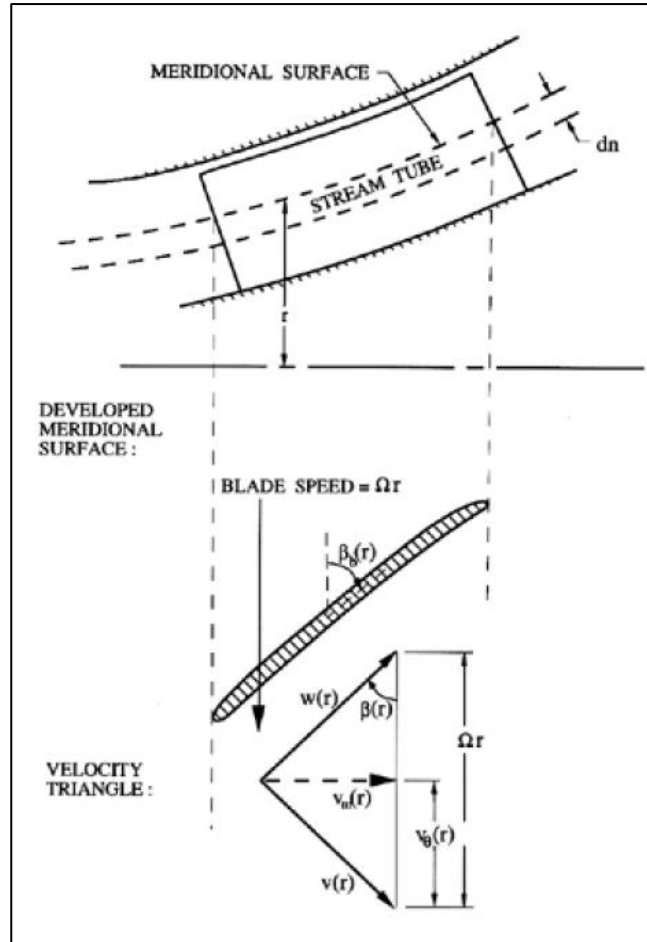


Figure 2.6: Developed meridional surface and velocity triangle (Brennen, 1994).

The flow angle,  $\beta(r)$ , and blade angle,  $\beta_b(r)$ , are defined by the angles made between the relative velocity vector or a tangent to the blade respectively, and a plane perpendicular to the axis of rotation. The incidence angle,  $\alpha(r)$ , is defined at the inlet as the difference between the blade and flow angles:

$$\alpha(r) = \beta_{b1}(r) - \beta_1(r) \quad [2.14]$$

Similarly at the outlet the deviation angle,  $\delta(r)$ , is defined as:

$$\delta(r) = \beta_{b2}(r) - \beta_2(r) \quad [2.15]$$

The deviation angle is related to the solidity of the impeller, which is a geometric ratio between the width of the flow passage between blades and the length of that passage. Figure 2.7 shows the incidence and deviation angles in relation to the blade angles at inlet and outlet.

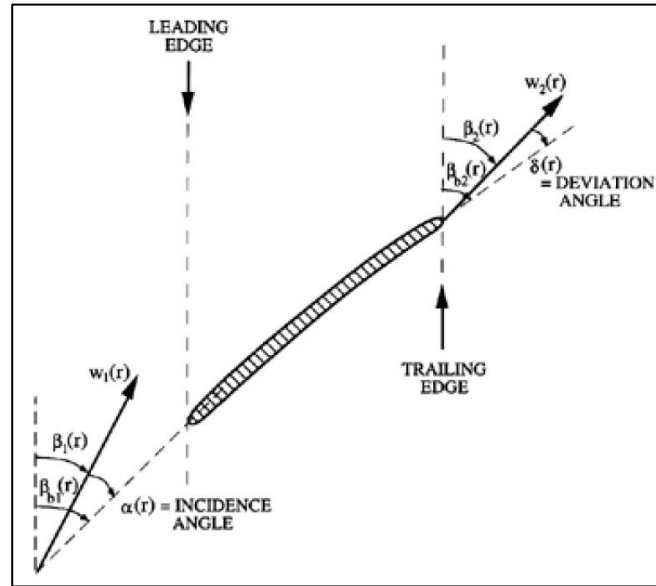


Figure 2.7: Incidence and deviation angles (Brennen, 1994).

When looking at flow along a stream tube the parameters that are important are the static pressure,  $p$ , the total pressure,  $p^T$ , and the velocity,  $v$ . In this analysis the flow is assumed inviscid and incompressible. The total pressure is the total mechanical energy stored within the flow and is defined as:

$$p^T = p + \frac{1}{2} \rho v^2 \quad [2.16]$$

$$p^T = p + \frac{1}{2} \rho (v_m^2 + v_\theta^2) \quad [2.17]$$

The head rise along a stream tube,  $h = (p_2^T - p_1^T)/\rho g$ , is the total change in mechanical energy of the flow as it passes through the impeller. The mass flow through an annular stream tube is defined as follows:

$$\dot{m} = 2\pi r v_m dn \quad [2.18]$$

Where  $n$  is the coordinate normal to the meridional surface. The continuity equation requires that the mass flow rate be constant through the pump. The volumetric flow rate,  $Q$ , can then be calculated using the following integral:

$$Q = \int_{R_H}^{R_T} 2\pi r v_m(r) dn \quad [2.19]$$

and the total dynamic head (TDH) can be calculate using the integral:

$$\text{TDH} = \frac{1}{Q} \int_{R_H}^{R_T} \frac{(p_2^T(r) - p_1^T(r))}{\rho g} 2\pi r v_m(r) dr \quad [2.20]$$

### 2.3.2. Secondary Flows:

In the previous analysis the flow was assumed to travel along a two dimensional asymmetrical meridional annulus defined by the blade geometry, and viscous effects were ignored. When a real pump is considered, many factors contribute to the flow deviating from the idealised flow. All practical fluids have a viscosity and most pumps operate at high Reynolds numbers, typically in fully turbulent conditions (Brennen, 1994). This leads to highly unsteady flow within the impeller passages, with pressure and velocity gradients in all three dimensions. While the flow at the best efficiency point (BEP) of the pump may resemble something like the idealised flow, large deviations may occur at off design conditions (Fraser, 1981). Figure 2.8 shows the flow through an impeller with various secondary flows. At off design conditions, particularly at low flows, recirculation at the inlet and discharge can occur. This is a result of the pressure side of a blade having to do more work at these conditions. This creates a lower

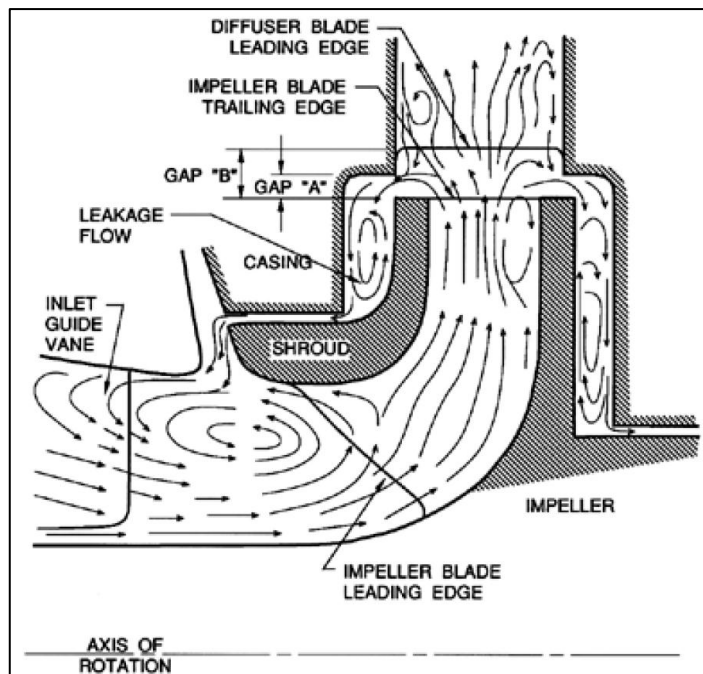


Figure 2.8: Sketch of the secondary flows present in an impeller (adapted from Makay, 1980).

pressure on the suction side of the blades which drives flow back into the impeller at the discharge or back past the inlet plane. The size of the flow passages relative to the pump affect

the development of recirculation and other secondary flows existing in the flow passage. Clearances between an impeller's blades or shroud and the pump casing allow for leakage flows. In the case of unshrouded impellers this tip leakage flow will move from the pressure side of a blade, through the clearance gap to the suction side of the same blade. For both shrouded and unshrouded impellers the leakage flow is driven from the high pressure discharge back to the low pressure inlet. These back flows can protrude many diameters into the inlet flow. Secondary flows have a large impact on the performance of a pump and cause the deterioration of efficiency.

### 2.3.3. Dimensionless Parameters:

The use of dimensionless numbers to describe pump behaviour is very useful in comparing pump performance and forms the basis of any scaling calculations. The primary dimensionless parameter that defines the operation of any pump is the specific speed,  $N$ . The specific speed is derived through the dimensional analysis of the relevant parameters, namely;  $H$ ,  $Q$  and the shaft speed,  $n$ , and is defined as:

$$N = \frac{nQ^{0.5}}{(gH)^{0.75}} \quad [2.21]$$

Different representations of the specific speed exist, depending on the units used. For this work the specific speed, defined by the SI units for each parameter, is used giving a truly dimensionless result. At the beginning of the pump design process  $H$  and  $Q$  are requirements of the system. By selecting a shaft speed, the specific speed can be determined for the operation. The specific speed is independent of size and can be used to determine the type of impeller best suited to the operation. For the typical range of pumps the specific speed ranges from around 0.1 to 5, with centrifugal pumps at the lower end and axial flow pumps the higher, as shown in Figure 2.9. As a performance parameter, the specific speed is normally calculated using the values of head rise and flow at BEP, however it can be determined at any operating conditions.

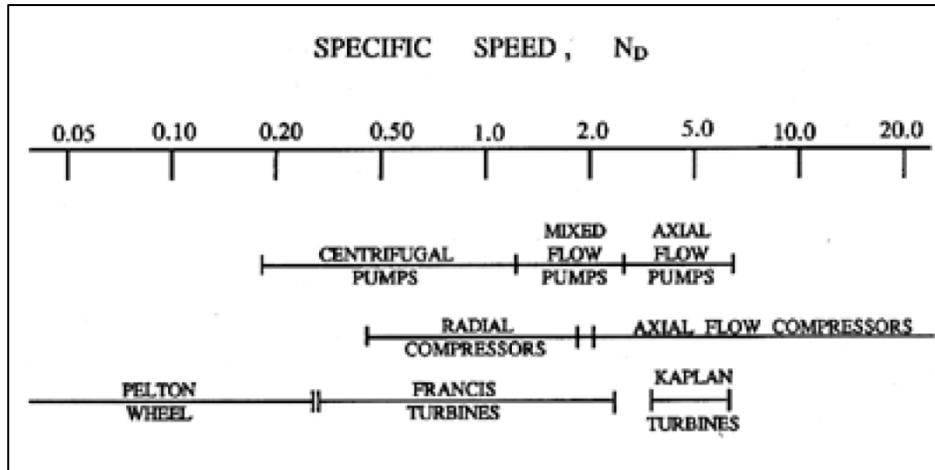


Figure 2.9: Pump, compressor and turbine impeller types with corresponding specific speed (Sabersky et al, 1989).

Additionally, there are two more dimensionless parameters used in describing pump performance, namely; the head coefficient,  $\psi$ , and the flow coefficient,  $\varphi$ . The head and flow coefficients are defined as:

$$\psi = \frac{gH}{R_T^2 \Omega^2} = \frac{gH}{U_T^2} \quad [2.22]$$

$$\varphi = \frac{Q}{AR_T^2 \Omega^2} = \frac{v_m}{U_T} \quad [2.23]$$

Both the head and flow coefficient can be defined at inlet or outlet by using the corresponding values for  $R_T$  and area,  $A$ . The outlet flow coefficient,  $\varphi_2$ , is used when describing performance while the inlet flow coefficient,  $\varphi_1$ , is more applicable when characterising cavitation and suction performance. For particular impeller geometries the head and flow coefficients define the dimensionless performance and are therefore the foundation for any scaling of performance.

#### 2.3.4. Pump operation:

Figure 2.10 presents a typical pump curve with two system head curves overlaid. At low flow rates the pump uses all its power to produce head rise. Power is required to produce flow, therefore as the flow rate is increased, the head rise decreases. At some point along the curve lies the BEP. At this point the pump performs most efficiently, converting input power into head and flow with minimal losses. It is good practice to operate a pump as close to this point as possible. When a pump is installed in a system, the point on its performance curve where it



will operate is defined by the intersection of the pump curve with the system head curve. To match the intersection point with the BEP point, selection of an appropriate pump is required.

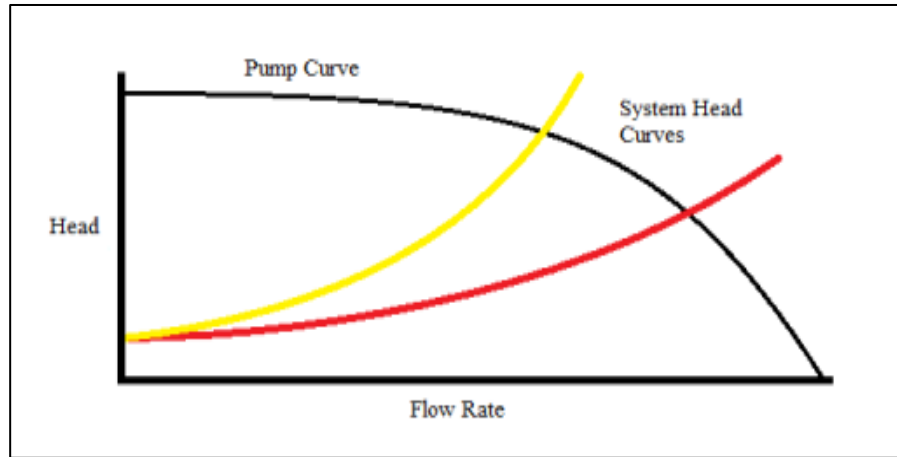


**Figure 2.10: Pump operating point, defined by the system head.**

The system head can also be changed, by valves or other physical changes, to vary the system head curve and hence the intersection point, as in Figure 2.10.

#### 2.4.5. Scaling:

From dimensional analysis, three dimensionless parameters can be derived from the relevant pump parameters of diameter and rotational speed (Timár, 2005). Each one is related to a specific performance parameter of a pump, namely; the head rise, flow rate or power. In relation to the head rise and flow rate, the dimensionless parameters defined are the head and flow coefficients respectively. A power coefficient is defined as well. When relating the performance of two geometrically similar pumps, these dimensionless parameters are used to define the operation of one pump, based on the other one's performance, as described by the affinity laws below:

$$\frac{H_1}{N_1 D_1^3} = \psi = \frac{H_2}{N_2 D_2^3} \quad [2.24]$$

$$\frac{Q_1}{N_1^2 D_1^2} = \varphi = \frac{Q_2}{N_2^2 D_2^2} \quad [2.25]$$

$$\frac{P_1}{\rho_1 N_1^3 D_1^5} = \text{Power Coefficient} = \frac{P_2}{\rho_2 N_2^3 D_2^5} \quad [2.26]$$

From the scaling laws it can be seen that the type of pumped fluid does not affect the developed head or volumetric flow rate. However, required power is affected by the density and hence the pumped fluid.

## 2.4. Suction Performance:

### 2.4.1. Suction and Cavitation Parameters:

To begin looking at suction performance the relevant parameters that describe the suction conditions must be understood. The primary cavitation parameter is the cavitation number,  $\sigma$ , defined as:

$$\sigma = (p_1 - p_v(T)) / \frac{1}{2} \rho U_{T1}^2 \quad [2.27]$$

Where  $p_1$  is some reference pressure, typically the inlet pressure, and  $p_v$  is the vapour pressure of the fluid as a function of temperature,  $T$ . The cavitation number provides a dimensionless description of the cavitation potential of a flow and is the fundamental cavitation scaling parameter (Arndt, 1981). The cavitation number is always defined, whether cavitation is present or not.

Another important parameter in describing suction performance is the Net Positive Suction Head (NPSH). At the inlet of a pump, the NPSH is defined as:

$$\text{NPSH} = (p_1^T - p_v(T)) / \rho g = \pm h_s + h_a - h_{\text{loss}} - h_v(T) \quad [2.28]$$

NPSH represents the total pressure head at inlet above the vapour pressure of the fluid (Schiavello and Visser, 2009). By using the suction static head or lift,  $h_s$ , the absolute pressure head at the fluids free surface,  $h_a$ , and the total friction loss in the inlet piping,  $h_{\text{loss}}$ , as shown in Figure 2.11, the NPSH can be determined. The NPSH of a particular system is a function of the inlet system arrangement and the flow rate. The elevation of the pump or reservoir and the pressure at the fluid free surface can all be used to manipulate the NPSH of a system. The length of the inlet piping, addition of pipe fittings, such as strainers, bends and valves, and the flow rate will affect the total friction loss and therefore the NPSH. Both cavitation number and NPSH can be used to assess the suction performance of a pump.

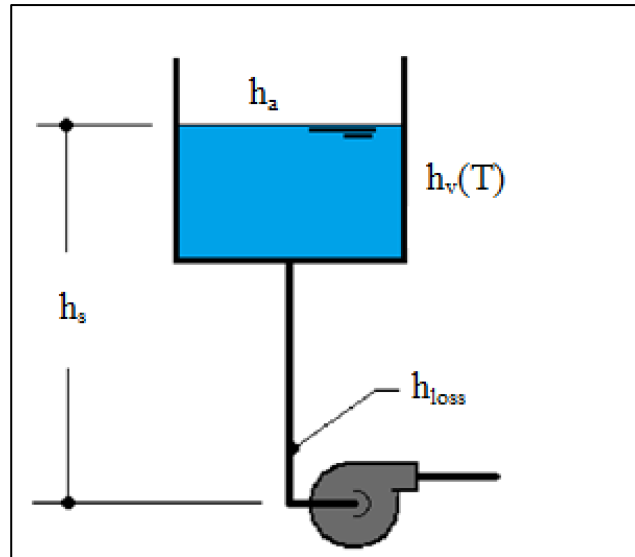


**Figure 2.11: Generalized inlet configuration with the relevant NPSH parameters defined.**

When NPSH is determined for a system, as has been done above, it is often referred to as the NPSH available, or  $NPSH_a$ . This distinction is made in order to differentiate the  $NPSH_a$  from what is known as the required NPSH, or  $NPSH_r$ .  $NPSH_r$  is a specification of the pump itself and is determined by testing. While they are often presented as different parameters,  $NPSH_r$  can be thought of as the critical value of  $NPSH_a$  at which a certain amount of cavitation is present. Typically suppliers would provide a  $NPSH_r$  curve that refers to the level of cavitation at which the head developed by the pump is reduced by 3%,  $NPSH_{3\%}$ , however  $NPSH_r$  can be determined for any level of cavitation within the pump. In order to avoid significant suction related performance degradation it is required that the  $NPSH_a$  be equal to or larger than the  $NPSH_{3\%}$ . It is important to note that cavitation is present within a pump even at values of  $NPSH_a$  that are above the  $NPSH_{3\%}$  requirement (Arndt, 1981). Performance is only affected once the cavitation has developed to a point that the vapour cavities occupy a significant portion of the impeller flow passages. Figure 2.12 shows a typical  $NPSH_r$  trend for a centrifugal pump. It can be seen that  $NPSH_r$  is at its maximum at maximum flow. As flow rate is reduced so too does  $NPSH_r$  until shutoff head is approached. Near shutoff head the pump operates inefficiently with significant recirculation and the majority of the power been converted to heat, causing the  $NPSH_r$  to increase (Shiels, 1998).

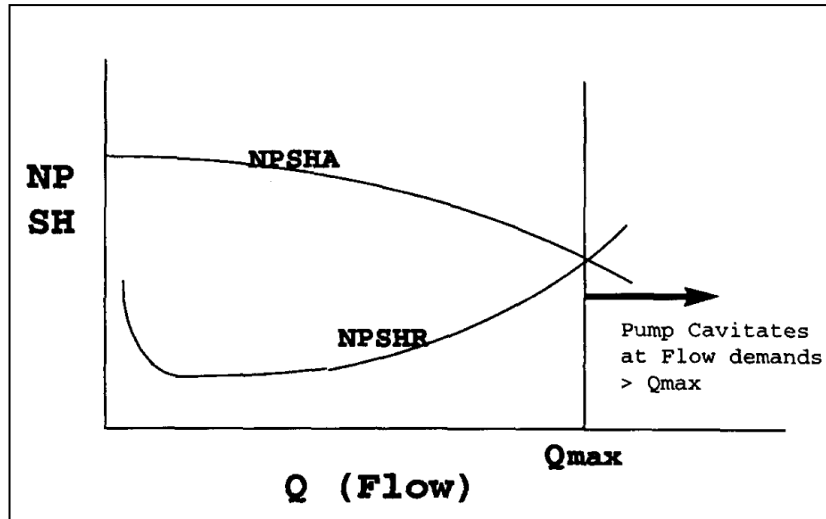


Figure 2.12: NPSH<sub>r</sub> trend for a centrifugal pump (Shiels, 1998).

The final parameter useful in describing suction performance is the suction specific speed,  $N_{ss}$ . Related to the specific speed, the suction specific speed is defined as:

$$N_{ss} = \frac{nQ^{0.5}}{(gNPSH)^{0.75}} \quad [2.29]$$

The suction specific speed can be calculated using either form of NPSH. Typically the suction specific speed is defined using the  $NPSH_{3\%}$  at BEP and is a parameter of the pump, however it can be defined for any point of operation. Another form of the suction specific speed, known as the corrected suction specific speed, can be defined as:

$$N'_{ss} = \frac{N_{ss}}{(1 - a)^{0.5}} \quad [2.30]$$

Where  $a$ , is the hub-to-tip ratio of the impeller. The corrected suction specific speed can be used to compare the suction performance of pumps with different inlet geometries (Furst, 1973).

#### 2.4.2. Cavitation Inception:

Cavitation is defined as the process whereby macroscopic vapour cavities are formed in a flow, as a result of a decrease in pressure, and subsequently collapse when entrained into regions of higher pressure (Brennen, 1995). In the absence of cavitation, the flow inside a pump is a function of the geometry and Reynolds number. It follows that any change in the overall pressure level will cause an equal change in pressure at every point within the pressure field.

As the overall pressure is decreased, eventually some point in the pressure field will reach some critical pressure at which cavitation inception occurs. The incipient cavitation number,  $\sigma_i$ , is defined at this point. This critical pressure is often assumed to be the fluid's vapour pressure, as a general guideline, however large deviations from this assumption are often observed (Brennen, 1994).

Experiments have been performed using pure liquids, contained in very smooth walled containers, showing they can withstand tensions, that is  $(p-p_v) < 0$ , of many atmospheres before the nucleation of macroscopic vapour bubbles occurs (Brennen, 1994). This type of nucleation is referred to as homogenous nucleation and its effects would clearly cause inception to occur at pressures lower than the vapour pressure and hence a smaller value for  $\sigma_i$ , than predicted by the vapour pressure, would be obtained. In practical pump flows however, this typically does not occur since heterogeneous nucleation is the primary source of cavitation. Heterogeneous nucleation refers to the formation of vapour cavities as a result of impurities, or nuclei, in the fluid. Dissolved gas, microscopic vapour/gas bubbles and suspended particles are all nucleation sites for the growth of macroscopic vapour cavities in a flow. In closed-loop systems, cavitation itself may be a source of nuclei as cavities formed may not entirely dissolve by the time they re-enter the pump. Nucleation sites can also exist in the surface defects of the rough solid container walls. The incipient cavitation point is primarily affected by nuclei suspended in the flow and is less so by the contamination of the solid container surfaces (Brennen, 1994). Both the number and size of the nuclei present in a fluid affect the potential for cavitation, where a larger value for either would result in higher values for  $\sigma_i$  than would be expected using the vapour pressure. Figure 2.13 presents cavitation inception data for the same headform,

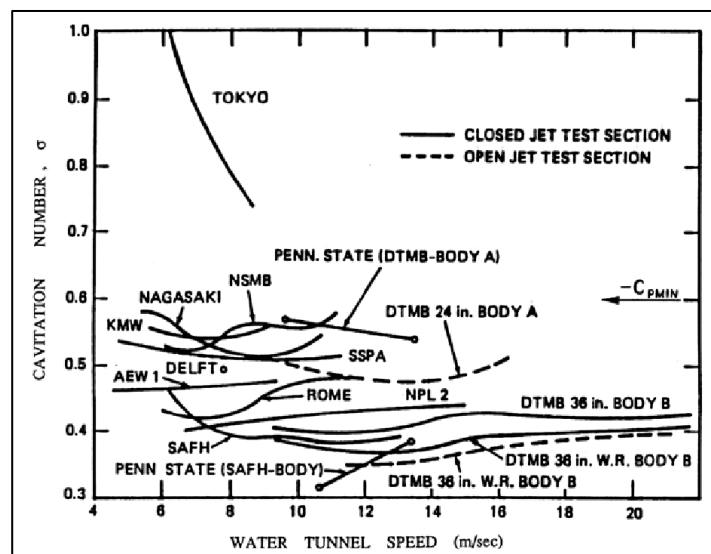


Figure 2.13: The effect of nuclei on cavitation inception on the same headform (Lindgren and Johnsson, 1966, Johnsson, 1969).

tested at different facilities. The large variations in results can be attributed to the difference in nuclei populations between the facilities. Once cavitation nuclei pass into regions of low enough pressure to cause growth, it takes a finite time before the nuclei reach a visible, or macroscopic, size. The time that a nucleus experiences a significant enough pressure gradient to cause growth while passing through an impeller is known as the residence time. If the residence time is too short, nuclei, even though they may experience an adequate reduction in pressure to force growth, will pass into a higher region of pressure before the cavity is allowed to grow to a stable, macroscopic size. Therefore a flow with a short residence time may have a lower value of  $\sigma_i$  than another flow with the same pressure field, but longer residence time.

The effects of turbulence and viscosity on cavitation inception must be addressed. Generally, the flow through most pumps is not only highly turbulent but unsteady as well (Brennen, 1994). This environment is conducive to the development of vortices and other turbulent losses. The pressure in the centre of a vortex can be significantly lower than the mean pressure of the flow and any nuclei entrained could possibly cavitate even if the remainder of the flow is above the critical pressure level. Nuclei entrained into a vortex may also have a longer residence time than would otherwise be expected as the vortex action may seek to confine it to its centre. Research has shown that smaller nuclei are more susceptible to be drawn into vortices and this may be as a result of the vortex lines stretching and repelling the larger diameter bubbles. Secondary flows within the pump also create turbulence and cause large shear stresses in the fluid that work to lower the local pressure and may result in the promotion of cavitation inception. Turbulent effects cause the observed  $\sigma_i$  to be larger than would be otherwise expected.

Finally the effects of temperature on inception must be considered. In general, temperature will increase the value of  $\sigma_i$  by increasing the vapour pressure of the fluid. There is however another effect of temperature on cavitation inception that is less obvious. In certain circumstances, increased temperature can delay the onset of cavitation, thereby improving the cavitation performance of an impeller as seen in Figure 2.14. It can be seen that under the same operating conditions, an increase in temperature allows for operation at lower cavitation numbers. This effect of temperature on cavitation inception is called the thermodynamic effect. The residence time plays a significant role in whether or not this thermodynamic effect will be significant. To understand the mechanism by which this effect works, it is necessary to consider the dynamics of bubble growth (Brennen, 1995). At low temperatures the vapour density inside a bubble or cavity is low compared to high temperatures. To sustain bubble growth, vaporisation along the vapour-fluid interface must occur. Higher temperatures would then require a significantly higher rate of vaporisation, due to the higher vapour density, to sustain the same volume growth rate as a low temperature bubble or cavity. As a result, more heat must be conducted to the

interface for high temperatures. The thermal boundary layer at the vapour-fluid interface, developed in high temperature flows, is therefore significantly larger than for low temperature flows. The vapour inside a cavity at high temperatures is therefore at a significantly lower temperature than the bulk fluid, to sustain the large thermal gradient. This results in a lower pressure inside the cavity than would be expected, leading to a slowing of the bubble growth. With small residence times, this slowing of the bubble growth can delay the inception of cavitation and improve the cavitation performance of a pump. However, if significant residence time is available then the thermodynamic effect becomes less significant.

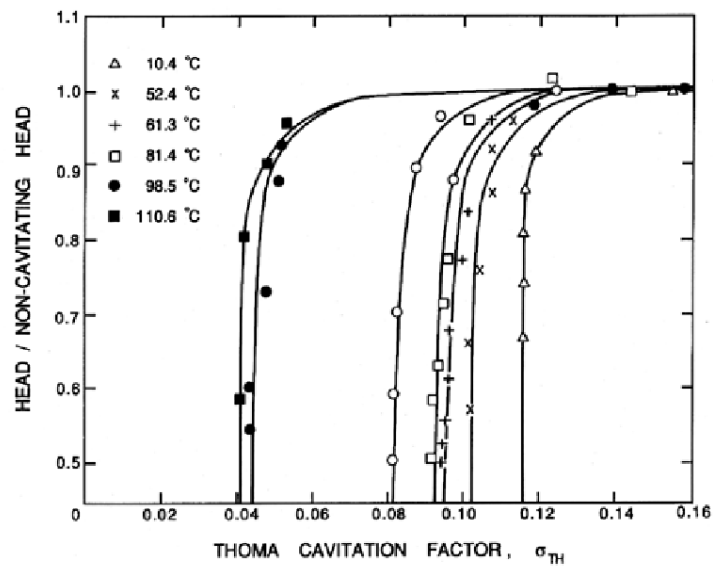


Figure 2.14: Thermodynamic effect on cavitation performance (Chivers, 1969).

### 2.4.3. Types of Cavitation:

As the pressure level is decreased beyond the inception level and significant time is allowed, the cavitation will grow and begin to take on certain forms based on the level of development. Figure 2.15 depicts some typical forms of cavitation, particularly for an unshrouded axial impeller. These developed forms of cavitation are not affected by the factors that affect inception and are primarily a function of the overall pressure level (Brennen, 1994).

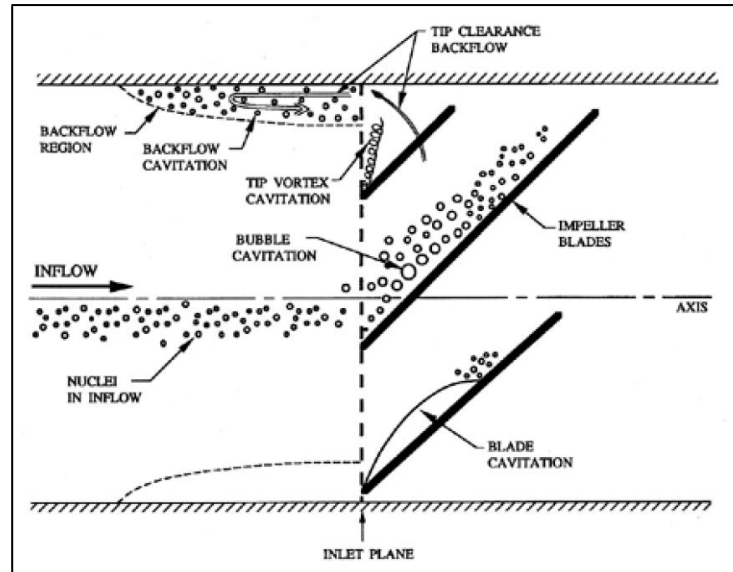


Figure 2.15: Typical forms of cavitation for an unshrouded axial impeller (Brennen, 1994).

Typically in pumps, cavitation will first appear as travelling bubbles in the flow on the suction side of a blade. These bubbles will appear randomly, as nuclei are randomly positioned in the fluid, and generally do not persist deep into the flow passage of the impeller, often as far as the next blade's leading edge. As the pressure level is decreased further, the cavitation bubbles will grow until they begin to combine with the surrounding bubbles to form vapour filled cavities. Typically these vapour filled cavities will attach to any nearby surfaces. This type of cavitation is referred to generally as attached cavitation or, more specifically for turbo-machinery, as blade cavitation. In some extreme cases, these vapour filled cavities can extend into the outlet flow of the machine. In such cases the cavitation is termed 'super cavitation'. Figure 2.16 shows travelling bubble cavitation on a hydrofoil on the left, and blade cavitation in a centrifugal pump on the right.

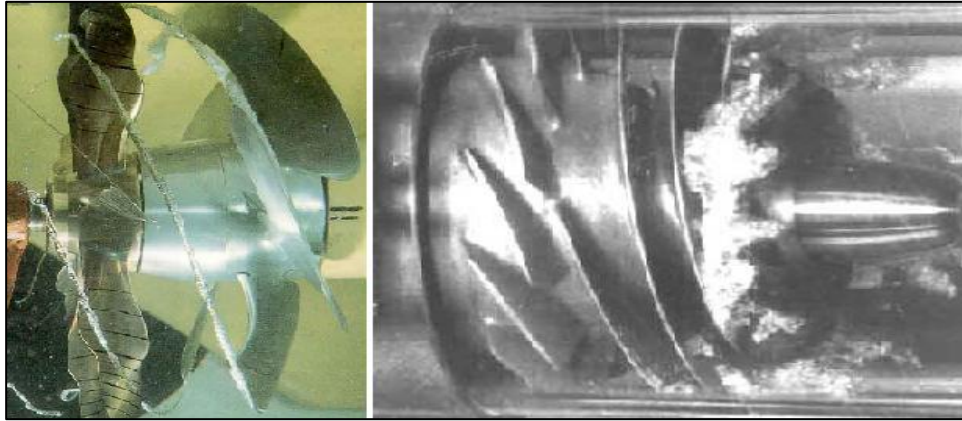


Figure 2.16: Travelling bubble cavitation on NACA hydrofoil (Kermeen, 1956), and blade cavitation in a centrifugal pump (Sloteman et al, 1991).

As mentioned earlier, cavitation may result from the decrease in pressure created at vortex cores. Vortex cavitation is another form of cavitation that may develop in an impeller. In



unshrouded impellers, tip vortex cavitation, as shown in Figure 2.17 on the left, is often the first to appear. Secondary flows, such as recirculation and backflow, may also be the cause of cavitation due to the large shear stresses and turbulence they introduce into the flow. An example of backflow cavitation is shown on the right of Figure 2.17. The cavitation bubbles can be seen to protrude upstream of the inlet plan.



**Figure 2.17: Vortex cavitation on a ship impeller (Brennen, 1994), and backflow cavitation in a scaled SSME low pressure LOX turbopump (Braisted, 1979).**

Rotating cavitation is a form of cavitation that may not appear in all impeller designs. This form of cavitation generally occurs at flow rates significantly lower than the BEP flow. Figure 2.18 shows snapshots of an impeller experiencing rotating cavitation. A cavity forms in one of the blade passages and the blockage caused by the cavity alters the flow into the adjacent passages. The altered flow then causes cavitation to form in the adjacent passages and alleviates the cavitation in the original passage. Rotating cavitation is usually a precursor to other flow instabilities such as auto-oscillation and surge.

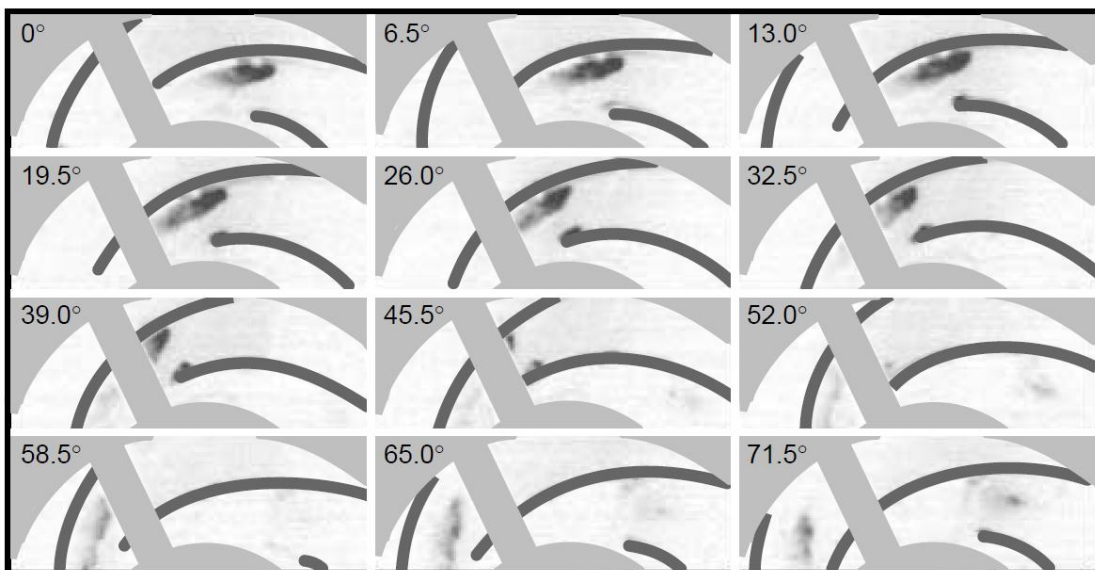


**Figure 2.18: Rotating cavitation in a centrifugal pump at off-design conditions (Hofmann, 2001).**

#### 2.4.4. Cavitation Effects:

In almost all pump applications cavitation is an unwanted phenomenon that should be avoided as much as possible, however, practical implications may require operation with a certain amount of cavitation. It is therefore important to understand the effects that cavitation can have on a pumps performance and reliability.

As mentioned above, cavitation can affect the hydraulic performance of a pump once substantial vapour has developed in the impeller. This leads to a reduction in output head, flow, efficiency and in extreme cases can cause ‘vapour locking’ of the impeller, whereby a complete breakdown of performance occurs. While performance loss can have severe consequences for the system the pump serves, it can be avoided by the proper design of the suction line to meet the NPSH requirements of the pump.

There are however, other effects of cavitation that appear even when the NPSH requirements are met. When cavitation bubbles implode they do so with a significant amount of energy. This creates large pressure waves which propagate through the fluid and the solid structures of the pump. An increase in vibration and sound levels are a result of these pressure waves (Baldassarre et al, 1998). Increased vibration can have negative effects on the pump and system components such as bearings, seals and couplings. Apart from the increase in vibration and sound, pressure pulsations as a result of cavitation can have a much more direct effect on the pump components. If a cavitation bubble implodes close enough to a solid surface a micro-jet is formed that directs the implosion towards that solid surface. This direction of the implosion, as well as the pressure spike the implosion creates, can damage the solid surface of the pump or impeller. Continual repetition of bubbles imploding near a particular area of an impeller can result in severe damaging and in some cases complete failure of the pump. Cavitation damage is a type of fatigue damage and generally presents itself as pitting of the solid material, as seen in Figure 2.19. Cavitation can also affect the flow field of an impeller by creating blockages which force the fluid to accelerate through the now reduced flow passages or take a different route through the impeller. This may cause instability in the flow and fluctuations in the output of the impeller which may have significant adverse effects for components and systems fed by the pump.

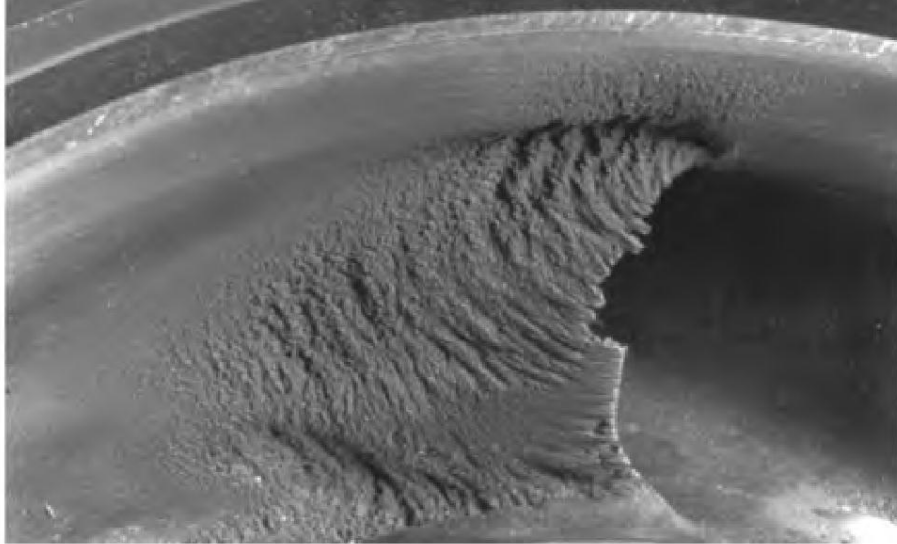


**Figure 2.19: Cavitation damage (Gülich and Rösch, 1988).**

## **2.5. Methods for Detecting Cavitation:**

### **2.5.1. Performance Degradation:**

The easiest method of detecting cavitation is to monitor the degradation of a pump's performance. It is for this reason that most pump suppliers specify their suction requirements based on cavitation induced performance loss. Figure 2.20 shows the effect on the head coefficient of a pump as a result of decreasing cavitation number at a constant flow coefficient. It can be seen that the head coefficient remains reasonably constant until the cavitation number is significantly reduced and the head coefficient begins to decline. Following this a gradual reduction in head coefficient is observed, as cavitation begins to occupy significant volumes in the flow passages. At some critical value of cavitation number the cavitation present in the flow passages is significant enough to cause head breakdown and the head coefficient reduces significantly with a small reduction in cavitation number. While this is the primarily used method for rating a pumps cavitation performance, it provides the least information with regards to the types and development of cavitation and it can tell one little about cavitation inception. Figure 2.21 is an example of how this method can detect certain types of cavitation.

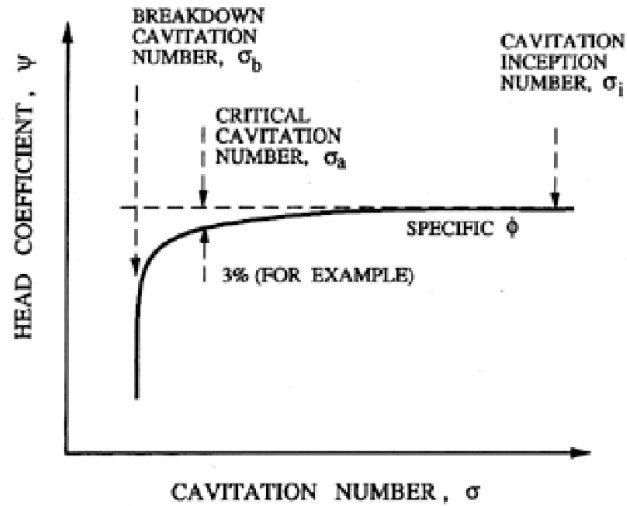


Figure 2.20: Effect of cavitation on head rise (Brennen, 1994).

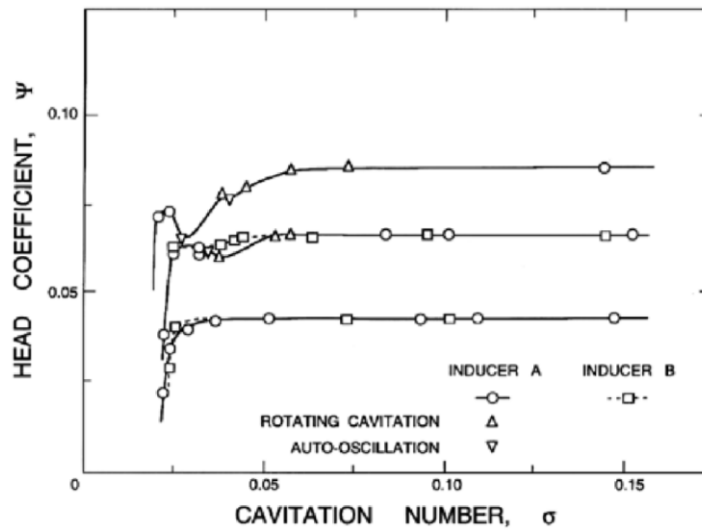


Figure 2.21: Effect of rotating cavitation on the head rise of two inducers (Kamijo et al, 1977).

The top two curves in the figure show a saddle, with a local minimum head coefficient, before head breakdown occurs. This gradual reduction in head coefficient is due to rotating cavitation, which does not present itself in the bottom curve. To learn more about inception and to detect more general forms of cavitation, other methods must therefore be implemented.

### 2.5.2. Visual Inspection:

Visually assessing a flow to determine the extent of cavitation is another method that can be used. Visual inspection can provide great insight into cavitation inception, cavitation structures and development within a flow. For this reason many research efforts regarding cavitation have employed test sections that allow for visual access to the flow. While this method is attractive for research, in practice it can prove tricky to implement. Figure 2.22 show a sketch of a system used for visual cavitation detection. Stroboscopic lighting and high speed photography are used to capture images of the impeller flow conditions. The camera is generally synchronised with the impeller shaft to ensure that images are taken at the correct point in the rotation of the impeller. The difficulties in providing visual access to the complex geometry of most pumps and the resources required to allow for usable information to be obtained, means that in many cases this method may be unfeasible.

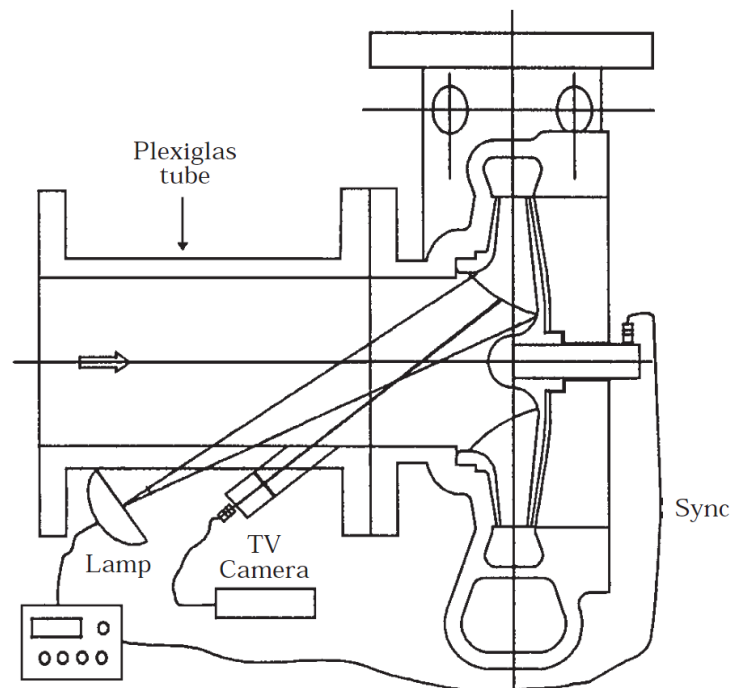


Figure 2.22: Schematic of an optical system used for visual cavitation detection (Baldassarre et al, 1998).

### 2.5.3. Pressure, Vibration and Noise:

Pressure waves, created by collapsing bubbles or cavities, and the associated vibration and noise are another means by which cavitation can be detected and assessed. Figure 2.23 shows the spectral distribution of sound between 100 and 10000 Hz for a pump. The thick line

represents operation without any cavitation, while the thin line was recorded under cavitating conditions. It can be seen that cavitation noise is broad band in nature, affecting all frequency in the band measured. This is a result of the random positioning and size of nuclei as well as the turbulence of the flow. In some cases cavitation noise can be found to affect specific discrete frequencies. In Figure 2.23 it can be seen that the emitted noise shows a significant increase at the frequency of 147 Hz, which is related to the blade passing frequency of the particular impeller (Čudina and Prezelj, 2008). The range and intensity of cavitation noise is dependent on the size and lifespan of the bubbles or cavities that are creating it. Small bubbles or cavities, typically present at cavitation inception and early development, will grow and collapse rapidly, producing high frequency noise and vibration. This noise is typically in the ultrasound range, between 20 kHz and 400 kHz (Koivula et al, 2000). As pressure is reduced, residence time is increased, allowing cavities to grow larger and remain at reduced pressure for longer. These larger bubbles or cavities emit noise and vibration at lower frequencies which can be heard with the human ear.

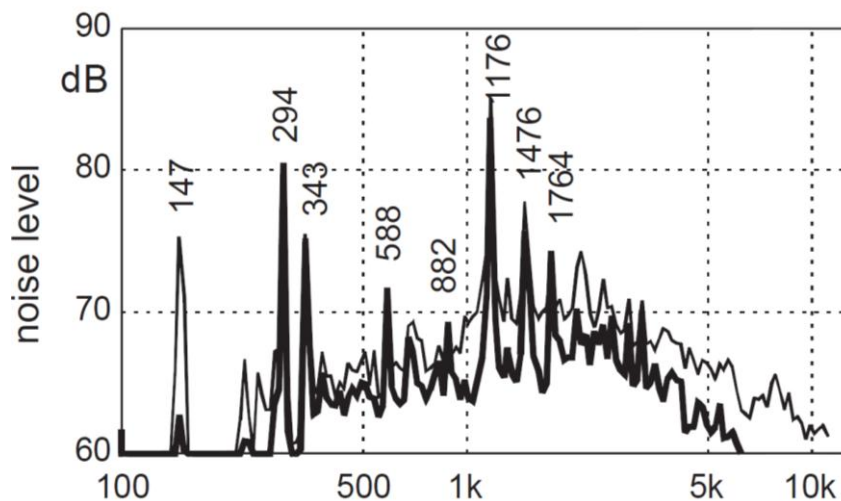


Figure 2.23: Noise frequency spectrum showing the difference between non-cavitating and cavitating conditions (Čudina, 2002).

Figure 2.24 shows the overall level of the noise signal as a function of cavitation number. Displayed as well is the head rise curve, also a function of cavitation number. The data is for a constant flow rate. The noise level can be seen to increase at the point of cavitation inception. The small cavities present at this point are not large enough to affect the head rise of the pump. As cavitation number is further reduced, the noise level increases, owing to the greater number and size of the bubbles or cavities present in the flow. Further reduction in cavitation number causes a peak in the noise level followed by a rapid decline. This decline in noise level is a result of large volumes of vapour forming in the impeller. These large vapour cavities have higher compressibility than the liquid and act to damp out the noise (Schiavello and Visser,

2009). Only after this point of large scale cavitation development, can any reduction in head be detected. In a similar way to the noise level, the vibration caused by cavitation can be seen to increase with decreasing cavitation number, as in Figure 2.25.

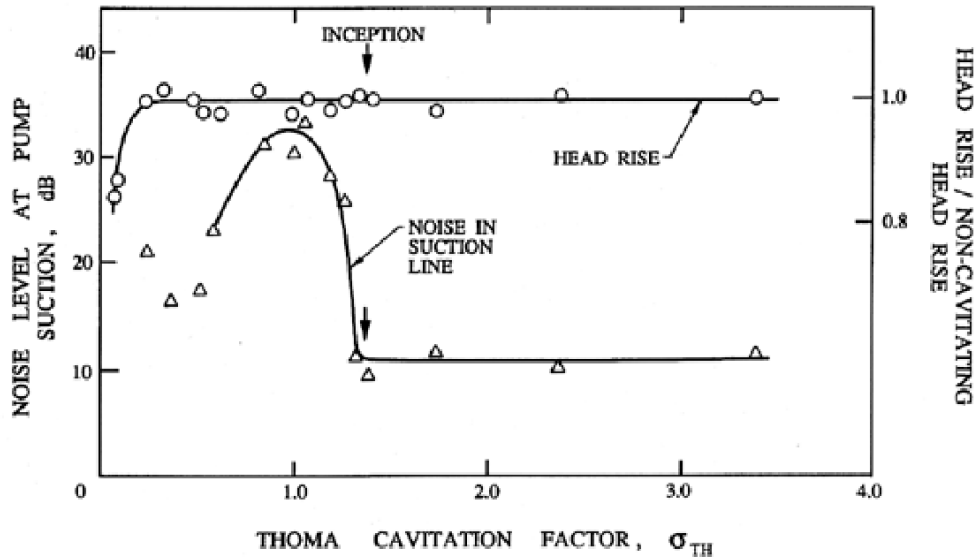


Figure 2.24: Noise level and head rise as a function of cavitation number for a centrifugal pump (adapted from McNulty and Pearsall, 1979).

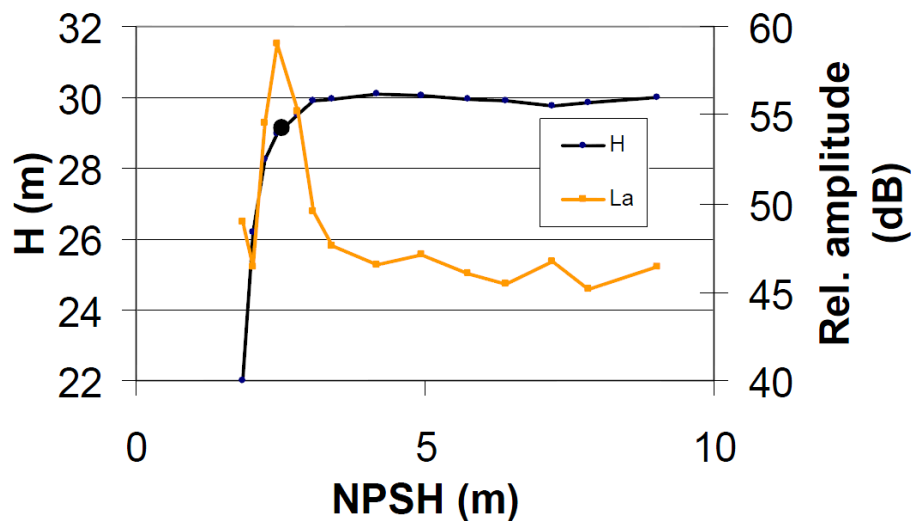


Figure 2.25: Vibration levels and head rise as a function of  $NPSH_a$  for a centrifugal pump (Černetič et al, 2008).

This approach to cavitation detection has many advantages over the other methods. Noise produced from cavitation is present as soon as cavitation occurs. For this reason, provided a sensitive enough sensor is used, cavitation noise or pressure waves can be used to detect inception. This method is much simpler to implement than visual inspection while providing a significant amount of information with regards to the cavitation development (Koivula et al, 2000). High response pressure transducers can also be used to measure the pressure

fluctuations as cavities implode. Hydrophones can be installed in the flow and can be used to measure the ultrasonic sound emitted from small cavities. The use of microphones, positioned externally to the pump casing, has successfully been used to detect cavitation in the audible range of 20 Hz to 20 kHz (Čudina, 2002). However, environmental and machinery noise can affect the results obtained with this method. It is therefore necessary to identify the contribution from the environment and machinery to the overall noise levels as well as the distribution in the frequency domain. Appropriate filters can then be applied to help isolate the cavitation noise from the other contributing factors. Accelerometers are also used to detect the vibration of surfaces as a result of cavitation.

## **2.6. Cavitation Test Facilities:**

### **2.6.1. Aerospace Corporation Test Facility (Ehrlich et al, 2009):**

The aerospace corporation developed a cavitation test loop for inducer cavitation testing. The facility was designed with a modular shaft and housing section to accept a number of different inducer designs. The supporting structure was designed such that it had no modes of vibration within the expected range of cavitation induced vibration. The facility uses water as a substitute for cryogenic propellants. Heating of the water was implemented to ensure accurate similarity between the fluid properties of the test and actual fluids. Figure 2.26 shows a schematic of the facility. An 830 litre pressure vessel was used as the fluid reservoir. System pressure could be altered by adjusting the pressure in the ullage volume at the top of the tank. A deaeration system was employed to reduce the nuclei content of the system. The flow passes through a flow conditioner before it reaches the test article to ensure a uniform velocity profile at the inlet. The test inducer is placed at the top right of the facility with its axis of rotation in the vertical direction. This was done to eliminate the hydrostatic gradient present in horizontal setups, cause by the difference in height between the top and bottom of the inlet flange. The facility allows for visual assessment of the flow and cavitation in the test inducer. A toroidal collector was used to accept the discharge from the test inducer and direct it to the discharge piping. A silent valve was fitted to the discharge piping inside the tank to provide control of the system flow while reducing the impact of the high velocity flow on the fluid inside the tank. A flow meter in the discharge line and sensors attached to the test inducer housing provide measurement of the relevant parameters.



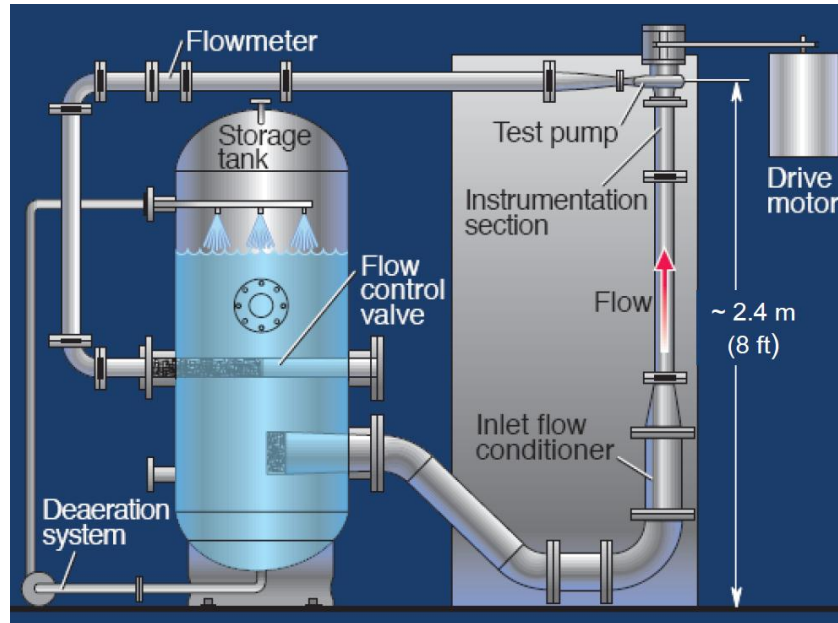


Figure 2.26: Schematic of the Aerospace Corporation inducer test facility (Ehrlich et al, 2009).

### 2.6.2. Pisa Cavitation Test Loop (Rapposelli et al, 2002):

The Pisa test loop was designed to investigate the rotodynamics of an impeller under both cavitating and non-cavitating conditions. In particular the steady and unsteady fluid forces, as a result of the impeller's whirl motion, were of interest. The facility also uses water as a surrogate for actual propellants. Figure 2.27 shows a schematic of the test facility. It is a closed loop, recirculating system. The tank on left can be pressure controlled to vary the inlet pressure to the test impeller. Flow meters in the suction and discharge line allow for flow rate measurement. The test section, around the pump housing, is fitted with the necessary pressure, temperature and force sensors required. Apart from the primary drive motor, a second motor is used to impart a whirl velocity to the impeller to determine the effects that this motion has on the forces experienced by the impeller. A silent throttle valve is installed in the discharge line. Control of the water quality, in terms of nuclei content, was also implemented in the design. The system can also simulate flow instabilities, such as auto-oscillation, to test the effects on the impeller's performance.

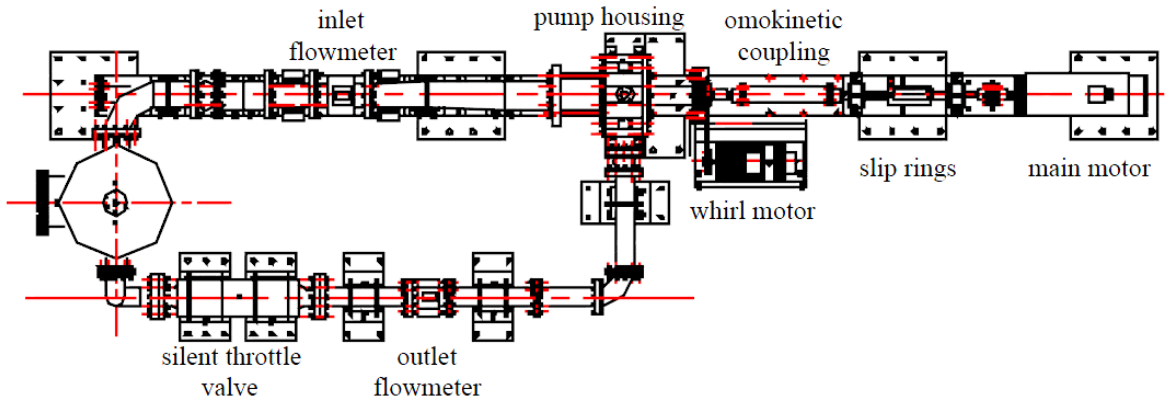


Figure 2.27: Schematic of the Pisa cavitation test loop (Rapposelli et al, 2002).

## CHAPTER 3

### Test Impeller Performance and Scaling

This chapter presents the design of a fuel turbopump impeller for use in a hypothetical commercial launch vehicle. A hypothetical launch vehicle was proposed to meet requirements of the South African space and satellite industry. From the specifications of the launch vehicle and mission parameters, the turbopump impeller's required performance was deduced. One dimensional mean-line and quasi-3D multi-stream tube analyses were used in the design of the impeller. The design performance of the impeller is presented. Scaling of the impeller was done to allow for lab scale testing. Scaling investigations were conducted to determine how the relevant parameters should be scaled. The expected performance of the test impeller is presented. Sizing of the hypothetical launch vehicle and the design of the full scale impeller was the work of Smyth (2014) and is summarised here. The scaled test impeller was developed by Smyth (2014) with the aid of the author.

#### **3.1. Hypothetical launch vehicle:**

##### **3.1.1. Proposed mission Parameters:**

The specifications for the launch vehicle were developed to meet the requirements of the local satellite industry. The launch vehicle mission requirements were to launch a payload of between 50 and 500kg into a 500km sun synchronous orbit (SSO) from the Denel Overberg Test Range (OTR). South Africa has the capacity to produce earth-observation microsatellites, with masses less than 100kg. SunSpace, a local satellite manufacturer, have built three satellites and developed a range of designs for satellites weighing between 50 and 500 kg (Campbell, 2008). The proposed vehicle would provide a means to launch these satellites locally. Heavier payloads could also be launched into lower earth orbits (LEO) with these specifications.

### 3.1.2. Launch vehicle configuration:

Selection of the engine cycle was the first step in defining the proposed launch vehicle. A two stage vehicle was required to achieve the mission parameters. The fuel turbopump impeller considered in the design was to function in the first stage of the launch vehicle. For this reason the expander cycle was not considered as it is best suited for upper stage engines. The staged combustion cycle was ruled out due to the complexity of the engine. The gas generator cycle was selected as the engine configuration for the launch vehicle. Since this configuration is the most common type of engine cycle in use and the reliability and simplicity of this cycle makes it the most suitable choice for this work.

The mechanical arrangement of the turbopump had to be selected in order to fully define the engine configuration. Figure 3.1 shows the three general arrangements of turbopumps. Use of gear couplings between the turbines and pumps, as in early designs, allows for each to operate at their optimal speeds. This method has fallen out of favour due to the added weight of the couplings. Fixed shaft arrangements, single or dual, have become the preferred method. Single shaft arrangements are the simplest and lightest method however efficiency is negatively impacted. The launch vehicle will make use of a dual shaft arrangement. Although this arrangement increases the overall weight of the system it allows for a more efficient design as each turbopump set can be optimised for its particular requirements (Huzel and Huang, 1992). This allows for the fuel turbopump to be developed independently of the oxidiser turbopump, thus simplifying the design for both.

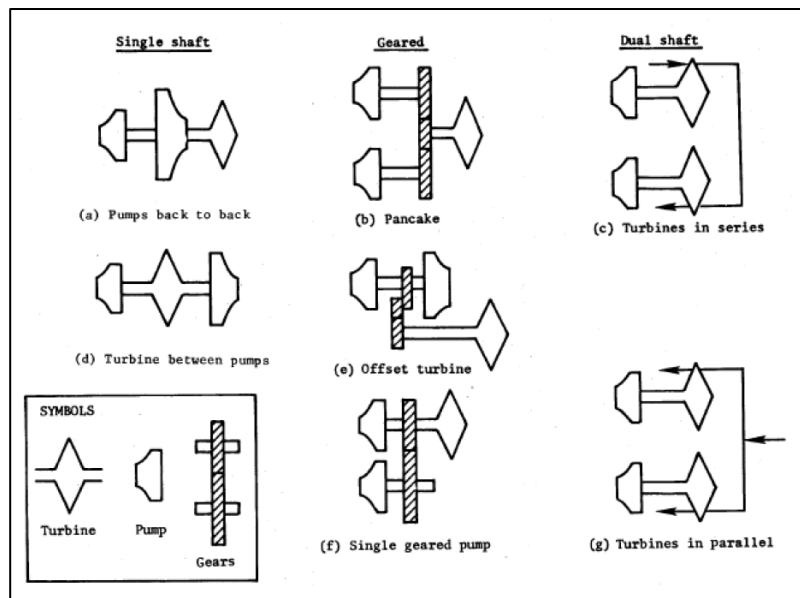


Figure 3.1: Turbopump shaft arrangements (Sobin and Bissel, 1974).

Propellant combinations are vital in determining the performance of an engine cycle. Practically there have been three combinations that have been primarily used, namely; liquid oxygen (LOX) and liquid hydrogen (LH<sub>2</sub>), LOX and kerosene (typically RP-1), and nitrogen tetroxide (N<sub>2</sub>O<sub>4</sub>) and hydrazine (N<sub>2</sub>H<sub>4</sub>). The N<sub>2</sub>O<sub>4</sub>/N<sub>2</sub>H<sub>4</sub> combination has the lowest specific impulse of the three, between 318.7 and 341.5s. The combination is also highly toxic. For these reasons it was not considered for use in the proposed vehicle. The combination of LOX and LH<sub>2</sub> is the best performing combination, giving a theoretical specific impulse of 455.3s (Huzel and Huang, 1992). However LH<sub>2</sub> is notoriously difficult to store and handle. Its low density means that to provide the required mass flow rates, high powered pumps are required. This makes a system utilising this propellant combination expensive and unsuitable for application in this work. The LOX/RP-1 propellant combination was therefore selected for use in the proposed vehicle. The higher density and non-cryogenic nature of RP-1 means that a system using this combination is simpler and cheaper than the LOX/LH<sub>2</sub> combination. This combination is also not as hazardous and is more efficient, with a theoretical specific impulse of 358.2s, than the N<sub>2</sub>O<sub>4</sub>/N<sub>2</sub>H<sub>4</sub> combination (Huzel and Huang, 1992). With the propellant combination selected, the oxidiser/fuel (O/F) ratio for the combustion chamber and gas generator had to be determined. This selection was based on the temperatures achieved in the combustion process. For the combustion chamber, an O/F ratio of 2.5 was selected, as this provides the highest temperature, and therefore most efficient burn (Parsley and Zhang, 2004). Turbine inlet temperatures typically cannot exceed 900 to 1200 K, depending on the materials used. For this reason a fuel lean or rich mixture had to be used in the gas generator to reduce the temperature of the combustion gasses entering the turbines. For this work, a gas generator O/F ratio of 0.32 was used, which produces a combustion temperature of 894.8 K.

To facilitate the selection of appropriate design parameters for the proposed launch vehicle, a review of existing launch vehicles was conducted. Five launch vehicles were identified, having similar mission requirements and therefore expected performance to the proposed vehicle. The selected launch vehicles were the Falcon 1e, Angara 1.1, Kosmos 3M, Delta II (without boosters) and Strela. All are two stage, light lift vehicles capable of achieving LEO. A summary of these vehicles parameters, used for selecting the proposed vehicles parameters, is shown in Table 3.1. The payloads listed in Table 3.1 were calculated using software called Silverbird Astronautics Launch Vehicle Performance Calculator, developed by Schilling, based on the proposed mission and each particular launch vehicle's parameters. This provides a means to draw comparisons based on the particular mission requirements. The software considers the various parameters of the launch vehicle and mission to determine the payload capacity.

**Table 3.1: Comparison of existing launch vehicle parameters.**

	<b>Falcon 1e</b>	<b>Angara 1.1</b>	<b>Kosmos 3M</b>	<b>Delta II (mod)</b>	<b>Strela</b>
<b>Stage 1 Thrust (vac) [kN]</b>	615.6	2084	1728	1085.8	2070
<b>Payload – Schilling [kg]</b>	412	1177	993	773	817
<b><math>\Delta V_1/\Delta V_2</math></b>	1.092	1.54	0.575	1.19	0.848
<b>Stage 1 <math>M_f</math></b>	0.939	0.930	0.939	0.944	0.940
<b>Stage 2 <math>M_f</math></b>	0.881	0.825	0.929	0.863	0.862
<b>Fairing Mass [kg]</b>	136	710	348	841	700

Of the five launch vehicles considered only two, the Falcon 1e and Delta II, use a LOX/RP-1 combination and the gas generator cycle. Selection of a suitable specific impulse for the proposed launch vehicle was therefore based on these two launch vehicles, as well as a review of other launch vehicles using the same configuration. It was found that the specific impulse for the first stage of vehicles using this specific configuration of engine falls predominantly in the range of 300 s to 340 s, in a vacuum, with a typical combustion chamber pressure of 50 bar. A conservative value of 300 s in a vacuum or 273 s at sea level, was selected therefore for the proposed vehicle, operating with a chamber pressure of 50 bar. The second stage specific impulse was selected to be 320 s.

The first stage thrust for the proposed vehicle was conservatively selected to be 1000 kN, in a vacuum. This value was chosen by comparing the thrust of the five launch vehicles considered and the difference between their payload capacities and the required payload capacity. With the first stage specific impulse and thrust defined, the total propellant mass flow was calculated to be 339.9 kg/s.

A second stage thrust of 35 kN, in a vacuum, was selected for the proposed launch vehicle. Mass fractions for the first and second stages were selected to be 0.9375 and 0.875 respectively. These values are conservative in comparison to existing launch vehicles in order to ensure that they are achievable. A fairing mass of 200 kg was selected for the proposed launch vehicle. This was chosen by comparing the fairing mass of the considered launch vehicles along with the difference between their payload capacities and the required payload capacity of the proposed launch vehicle.

The delta-V calculated for the proposed mission, using Schilling's method, was 10225 m/s. This is the total delta-V for both stages and must therefore be achieved through the contribution of both. The delta-V ratio of the two stages was selected to be 1.33. This was chosen based on

the delta-V split of the Falcon 1e, Angara 1.1 and the Delta II. The other two launch vehicles make use of a missile derived first stage and were therefore not considered for comparison.

A summary of the proposed launch vehicle parameters is shown in Table 3.2. The validity of the proposed vehicle and mission were assessed using the Silverbird software. A Schilling payload capacity of 529 kg was determined for the vehicle and mission parameters. Therefore the selected parameters were considered feasible in attaining the mission requirements of a 500 kg payload into a 500 km SSO from OTR. It must be noted that although the selected parameters were adequate to achieve the mission objectives, in practice these parameters would need to be achieved with the appropriate design of the various components of the launch vehicle. As this work is focused on the fuel turbopump impeller, it was sufficient to simply select the parameters in order to determine realistic requirements of the impeller. Additionally, only parameters required to determine the fuel impeller performance and the feasibility of the proposed mission were considered.

**Table 3.2: Summary of proposed launch vehicle parameters.**

		Vehicle Parameter	
Stage 1		Propellant Combination	LOX/RP-1
		Engine Cycle	Gas Generator
		Dry Mass [kg]	2718.5
		Propellant Mass [kg]	40777
		$M_f$	0.9375
		R	7.25
		Thrust (Vac) [kN]	1000
		Thrust (S.L.) [kN]	910.3
		$I_{sp}$ (Vac) [s]	300
		$I_{sp}$ (S.L.) [s]	273
		Chamber Pressure [bar]	50
		O/F Ratio (CC)	2.5
		O/F Ratio (GG)	0.32
		Propellant Mass Flow Rate [kg/s]	339.9
		Burn Time [s]	119.97
	Delta-V [m/s]	5828.2	
Stage 2		Dry Mass [kg]	388.21
		Propellant Mass [kg]	2717.5

	$M_f$	0.875
	R	4.06
	Thrust (Vac) [kN]	35
	$I_{sp}$ (Vac) [s]	320
	Propellant Mass Flow Rate [kg/s]	11.15
	Burn Time [s]	243.65
	Delta-V [m/s]	4396.7
<b>General Parameters</b>	Fairing Mass [kg]	200
	Liftoff Mass [kg]	47301.21
	Delta-V Ratio	1.33
	Total Delta-V [m/s]	10225
	Payload – Schilling [kg]	529

### 3.1.3. Fuel turbopump requirements:

The propellant combination, total propellant mass flow rate, O/F ratio and chamber pressure, determined previously, form the basis from which the fuel turbopump performance requirements were determined. To fully define the performance requirements of the fuel turbopump, the system head must be defined.

Losses through the injectors and propellant feed line mean that the outlet pressure of the turbopump will be significantly higher than the required chamber pressure of 50 bar. These losses were determined based on recommendations from literature and comparison with existing turbopump systems. An injector loss of 20%, of the combustion chamber pressure, is recommended to sustain a stable combustion pressure (Huzel and Huang, 1992, Haidn, 2008). Typically, fuel would be pumped through the feed system into channels in the nozzle, for regenerative cooling of the nozzle and preheating of the fuel, before it enters the injectors. These losses are highly dependent on the design of the particular system; however recommendations suggest that a value of 15 bar, for the losses in the feed line and cooling channels is reasonable (Boysan, 2008). An outlet pressure of 75 bar was therefore selected, which correlates with the NASA estimate of a 50% higher turbopump outlet pressure than combustion chamber pressure. A pump inlet pressure of 3.5 bar was selected in accordance with other LOX/RP-1 systems (Sobin, 1974). The LOX turbopump would have to operate at the same output pressure in order to match the gas generator inlet pressure.



Optimal gas generator cycle engines use less than 4% of the total propellant mass flow rate for driving the turbines (Parseley and Zhang, 2004). Using the upper limit of 4%, the combustion chamber and gas generator mass flow rates were calculate to be 326.83 kg/s and 13.07 kg/s respectively. The O/F ratios for the combustion chamber and gas generator were then used to determine the total fuel mass flow rate required. The flow rates of RP-1 for the combustion chamber and gas generator were calculated to be 93.38 kg/s and 9.9 kg/s respectively, giving a total propellant mass flow rate of 103.28 kg/s. In the same way the oxidiser mass flow rates were calculated to be 233.45 kg/s and 3.17 kg/s for the combustion chamber and gas generator respectively, giving a total of 236.62 kg/s of LOX.

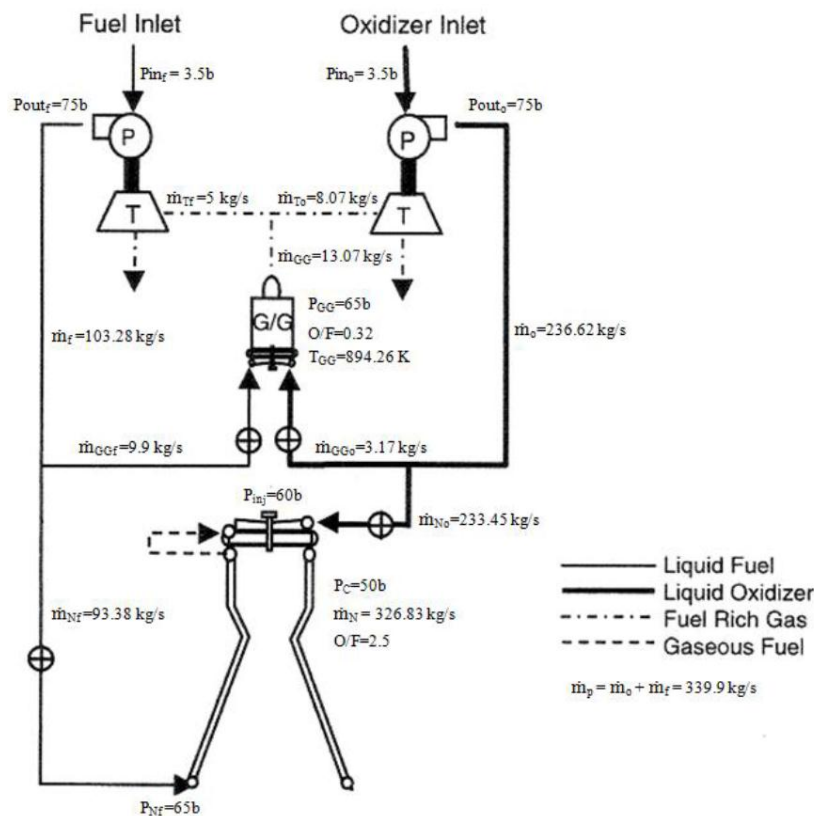


Figure 3.2: Propellant feed system schematic with calculated parameters (adapted by Smyth, 2014 from Parseley and Zhang, 2004).

The pump power requirements were determined using an efficiency of 70%. The fuel and oxidiser pump power requirements were calculated to be 1304 kW and 2113 kW respectively. The total mass flow rate to the gas generator was split using the ratio of pump powers to give fuel and oxidiser turbine mass flow rates of 5 kg/s and 8.07 kg/s respectively. Turbines pressure ratios can be as high as 20, however a conservative value of 10 was use to define the turbine output power. A turbine efficiency of 70% was used to calculate the power output. The fuel and oxidiser turbine output powers were calculated to be 1768 kW and 2854 kW respectively. These preliminary calculations suggest that adequate power is available to

overcome mechanical losses and power the propellant pumps. A schematic of the engine cycle is shown in Figure 3.2 with the calculated parameters shown. Table 3.3 shows the performance parameters defined for the fuel turbopump, which will be used as targets in the design process. Comparative rocket engine data can be found in Appendix A.

**Table 3.3: Summary of the fuel turbopump performance parameters.**

		Parameters	
<b>Pump</b>	$p_{in}$ [bar]	3.5	
	$p_{out}$ [bar]	75	
	$\dot{m}$ [kg/s]	103.3	
	$\rho_{RP-1}$	809	
	$\dot{W}$ [kW]	1304	
<b>Turbine</b>	$p_{in}$ [bar]	65	
	$p_{out}$ [bar]	1	
	$\dot{m}$ [kg/s]	5	
	O/F	0.32	
	$T_{in}$ [K]	894.7	
	$\dot{W}$ [kW]	1581	

### 3.2. Full Scale Impeller Design and Performance:

The requirements developed for the fuel turbopump set out the design space. Software packages PUMPAL and AxCent were used in the design of the impeller, implementing 1D mean-line and quasi-3D multi-stream tube analyses. An iterative approach was taken in the design of the fuel turbopump impeller. Inlet and discharge parameters were investigated with 1D mean-line analysis in PUMPAL. Once acceptable design parameters were established for the inlet and discharge, the through blade characteristics of the impeller were analysed in AxCent.

### 3.2.1. Design methodology:

The design of the fuel turbopump impeller began with the development of a base line design from which individual parameters could be assessed to arrive at the final design. This process made use of the requirements determined above and empirical data from literature. Suction performance is of vital importance in the design of turbopumps and for this reason was the start of the design process. To maintain simplicity of design, a separate axial inducer, to improve suction performance, was not considered. This placed restrictions on the inlet design parameters to ensure adequate suction performance. Literature suggested that the lowest feasible flow coefficient, without the use of an inducer, for turbopump design was 0.2 (Sobin, 1974). This value was used to determine the optimal suction performance based on the Brumfield Criterion. The Brumfield Criterion determines the most efficient suction performance possible based on flow coefficient, blade cavitation number and corrected suction specific speed (Japikse, 2001). Baseline values for corrected suction specific speed and blade cavitation numbers were determined to be 58.64 and 0.087 respectively. A value of 0.355 for the hub-to-tip ratio was selected based on recommendations from literature (Japikse et al, 1997). The suction specific speed could then be calculated, and along with the required flow rate and NPSH, the rotational speed of the impeller was calculated to be 14500 rpm. With the primary operational characteristics of the impeller defined, the specific speed was calculated to be 1633 (U.S), which is a typical value for Francis type impellers. The rotational speed and hub to tip ratio were then used to define the inlet geometry. The inlet tip diameter was selected based on a relationship with the flow coefficient. With considerations for inlet blockages, a tip diameter of 108.6 mm was calculated.

Based on the inlet design, the discharge parameters could then be determined. Developed head is affected by the outlet diameter, exit blade height, exit blade angle and number of blades. A 6 blade design was selected based on recommendations from literature and to avoid excess blockage at the inlet. The exit blade angle has a large impact on the developed head and stability of the impeller. Large angles provide the best head rise characteristic, reducing the diameter required, but are unstable. Rocket turbopumps require very stable operation and for this reason a smaller exit blade angle of 30 degrees, in the range recommended, was selected. The exit swirl parameter, expressed as the ratio of exit tangential velocity to meridional velocity, was also used to define the outlet geometry of the impeller based on the outlet flow conditions. A value of 4.6 was selected based on empirical data (Japikse et al, 1997). PUMPAL was then used to determine the most efficient combination of outlet diameter and blade height, based on the prescribe blade angle, blade number, exit swirl parameter and the required performance. An outlet diameter of 176.2 mm was determined..

With the baseline inlet and outlet parameters defined an investigation into the specific parameters was conducted using PUMPAL. This allowed for the optimisation of each parameter to arrive at the final parameters for inlet and discharge design. AxCent was then used to define the through blade geometry by determining the blade angle distributions and overall shape of the impeller. The primary goal of the through blade analysis was to ensure that the blade loading was acceptable, as well as to assess the diffusion characteristics of the impeller in order to control the development of secondary flows and other related flow conditions.

### 3.2.2. Final design geometry:

The final geometry of the impeller was generated in AxCent based on the approach described above. A 3D model of the final fuel turbopump impeller design is shown in Figure 3.3. It

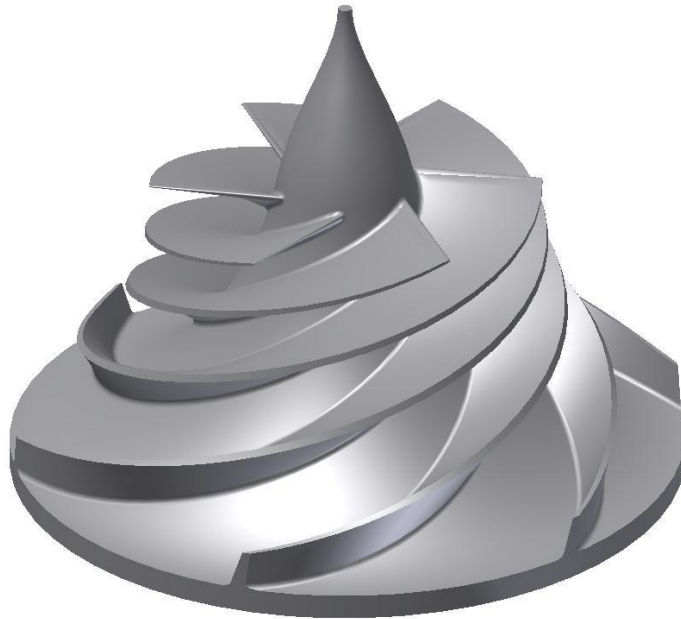


**Figure 3.3: 3D model of the final fuel turbopump impeller design (Smyth, 2014).**

consists of 6 full length 3-D blades with a wrap angle of 240 degrees. The impeller has inlet and outlet diameters of 108.6 mm and 186.7 mm respectively and an axial length of 140 mm. The impeller is of the Francis type, accepting flow axially and discharging it in the radial direction. The axial design of the inlet allows for some of the benefits of an inducer to be gained, improving suction performance, without the inclusion of an actual inducer. The 3-D nature of the impeller means that the blade angles vary along the both the blade length and height. The inlet blade angles vary, from 13.1 degrees at the tip to 30 degrees at the hub, in order to maintain a constant incidence angle, accounting for the radial change in blade velocity. An exit blade angle of 26 degrees was set for the impeller. Blade thickness varies along the

length to ensure structural rigidity base on the expected blade loading. Fillets were place at the intersection of the blades and hub to reduce the root stress on the blades. A summary of the impeller geometry is presented in Table 3.4.

### 3.2.3. Performance Data:

The performance of the impeller was determined in PUMPAL. Data points for flow rates varying from 40% to 130%, in intervals of 15%, of the design flow were considered. Rotational speed was also varied, in increments of 25%, from 50% to 125% of the design speed. Plots of head, power and efficiency, as functions of flow rate and rotational speed, were then developed.

Figure 3.4 shows the head rise of the impeller as a function of the flow rate. The design point is circled, with a head rise of 889 m and flow rate of 0.126 m<sup>3</sup>/s. For RP-1, the head rise relates to an outlet pressure of 74.9 bar. It can be seen that the design operating point lies on the point of greatest negative gradient. This was achieved through the design process to ensure the most stable operation possible. This point lies beyond the maximum efficiency of the impeller, as seen in Figure 3.5. This is often the trade-off made in rocket turbopump design as stability is of greater importance than efficiency. The design point has an efficiency of 80.3%.

The power requirements of the impeller are shown in Figure 3.6. The design point has a power requirement of 1127.8 kW. The effects of increasing rotational speed can clearly be seen in Figure 3.6 and will be an important factor in determining the scaled parameters of the test impeller. The NPSH requirements of the impeller are shown in Figure 3.7. The design value of 43.51 m, or 3.5 bar, was stipulated in the outline of the proposed launch vehicle and was met through the design of the inlet parameters. A summary of the impeller performance is shown in Table 3.4.

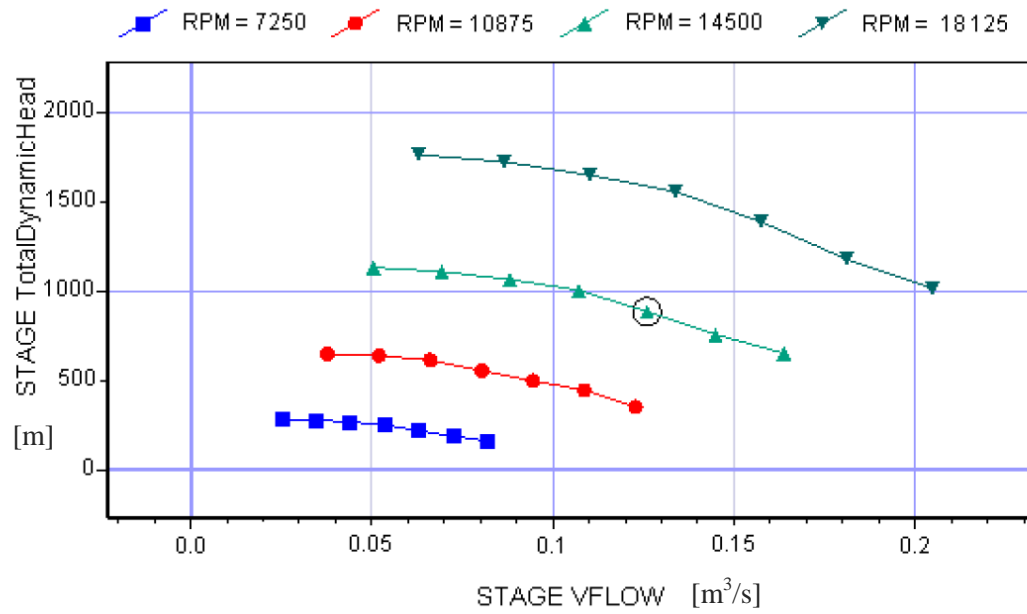


Figure 3.4: Head rise versus flow rate of the fuel turbopump impeller (Smyth, 2014).

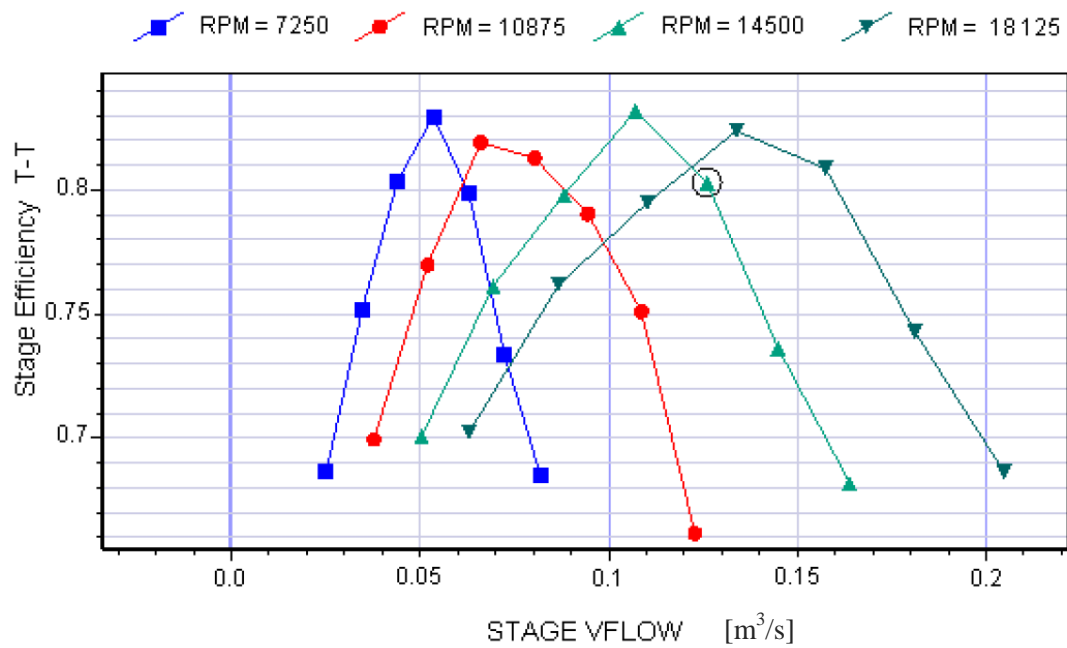


Figure 3.5: Efficiency versus flow rate of the fuel turbopump impeller (Smyth, 2014).

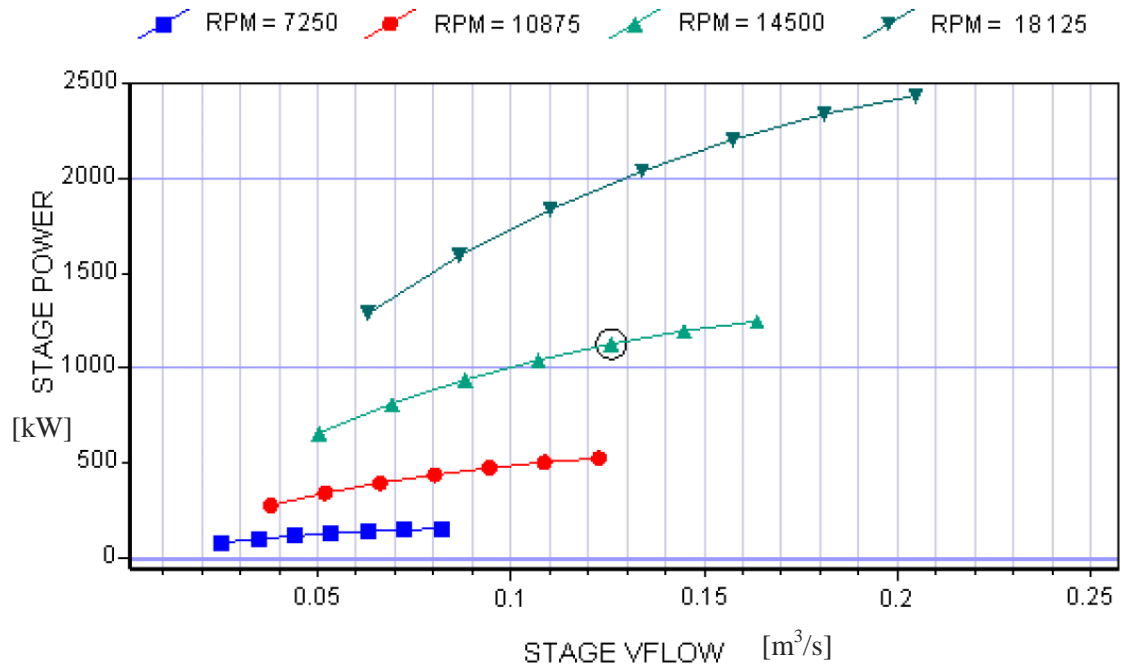


Figure 3.6: Power versus flow rate for the fuel turbopump impeller (Smyth, 2014).

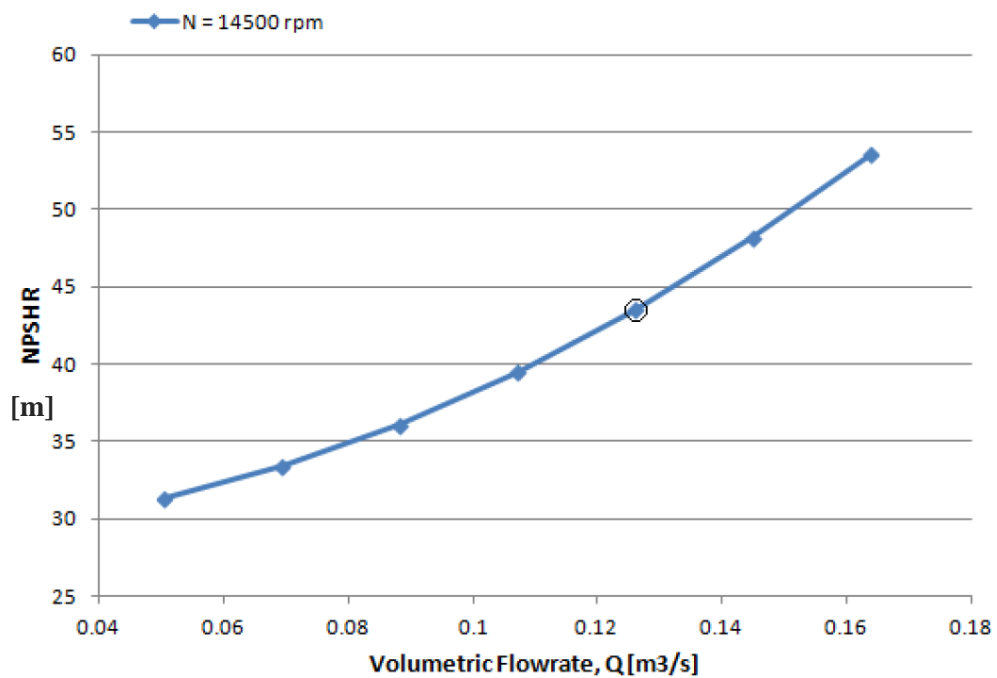


Figure 3.7: NPSH<sub>r</sub> versus flow rate for the fuel turbopump impeller (Smyth, 2014).

### **3.3. Scaled Test Impeller:**

The high performance of the full scale impeller, particularly with regards to rotational speed and power requirements, as well as the high NPSH requirements make the testing of the full scale design unfeasible on the laboratory scale. For this reason the test impeller would be required to operate at scaled conditions, reducing the rotational speed, diameter or both, in order to reduce the requirements of the test rig. Constraints on the test rig design, as a result of the available resources, facilitated the selection of the scaled test impeller rotational speed and diameter.

#### **3.3.1. Scaling criteria:**

Although the actual parameters of the test rig were unknown, parameters such as available power and inlet static head, for operation without a pressure vessel, were estimated based on the available space and resources in the laboratory. A maximum power and inlet static head of 65 kW and 4 m respectively were used as limiting factors for determining the parameters of the scaled test impeller. High rotational speeds were also considered to be a limiting factor. The expected performance of the scaled test impeller would then be used as targets to be met in the design of the test rig.

For a consistent geometry, rotational speed and impeller size are the two parameters that determine the performance of an impeller, as defined by the affinity laws. Scaling impeller size requires that all geometric parameters be reduced or increased by the same amount. This ensures geometric similarity and therefore consistent flow and head coefficients. Scaling of surface roughness and other small geometric features is required for strict adherence to the scaling laws. This can be difficult to achieve and can affect the accuracy of the predicted performance based on the scaling laws. Scaling rotational speed is considered to be more accurate than geometric scaling, provided the Reynolds number remains in the fully turbulent regime where the effects are fairly consistent. Reduction in rotational speed also aids in eliminating vibration and rotodynamic effects on the impeller, shaft and bearings. A compromise between rotational speed and geometric scaling, with the aim of maintaining both as close to the design condition as possible, was the aim of this scaling procedure.

The primary objective of the test rig is to verify the design operating point of the impeller. For this reason the design point performance parameters were used in the scaling investigation to



assess the final parameters of the test impeller. Figures 3.8 to 3.11 show the scaled performance, calculated using the affinity laws, for a range of rotational speeds and geometric sizes. Rotational speed was varied from 2000 rpm to 15000 rpm and geometric size from 50% to 100% of the full scale impeller. Figures 3.8 and 3.9 show the scaled head rise and flow rate characteristics of the impeller. While head rise and flow rate do not represent limiting factors in the design of the rig, knowledge of these parameters is vital in the selection of adequate piping and other system components such as sensors. Figure 3.10 shows the scaled power requirements of the impeller. With a limit of 65 kW, only points that lie on the dark blue of the plot can be considered. Full design speed or size can be achieved; however a significant reduction in the other parameter is required, which is not feasible. Rotational speeds of between 5000 rpm and 10000 rpm would allow for a geometric scaling factor of between 0.7 and 1 to be used. This range would satisfy the power limitations of the rig and allow for a good compromise between scaling of rotational speed and geometric size. The scaled  $NPSH_r$  of the impeller is shown in Figure 3.11. As suction performance is dependent on a number of factors, not considered in this simple scaling investigation, the scaled values were considered as a guide in selecting an appropriate scaled design. Actual suction performance would then be determined using PUMPAL software once the final scaling parameters are determined. Once again the dark blue represents the range in which the  $NPSH_r$  of the impeller can be met by the available static head of the rig. Rotational speed of below 6000 rpm allow for geometric scaling factors of between 0.7 and 1. With the required scaling ranges determined, based on power and  $NPSH_r$ , the final test impeller parameters can be determined. Scaling calculations and data can be found in Appendix C.

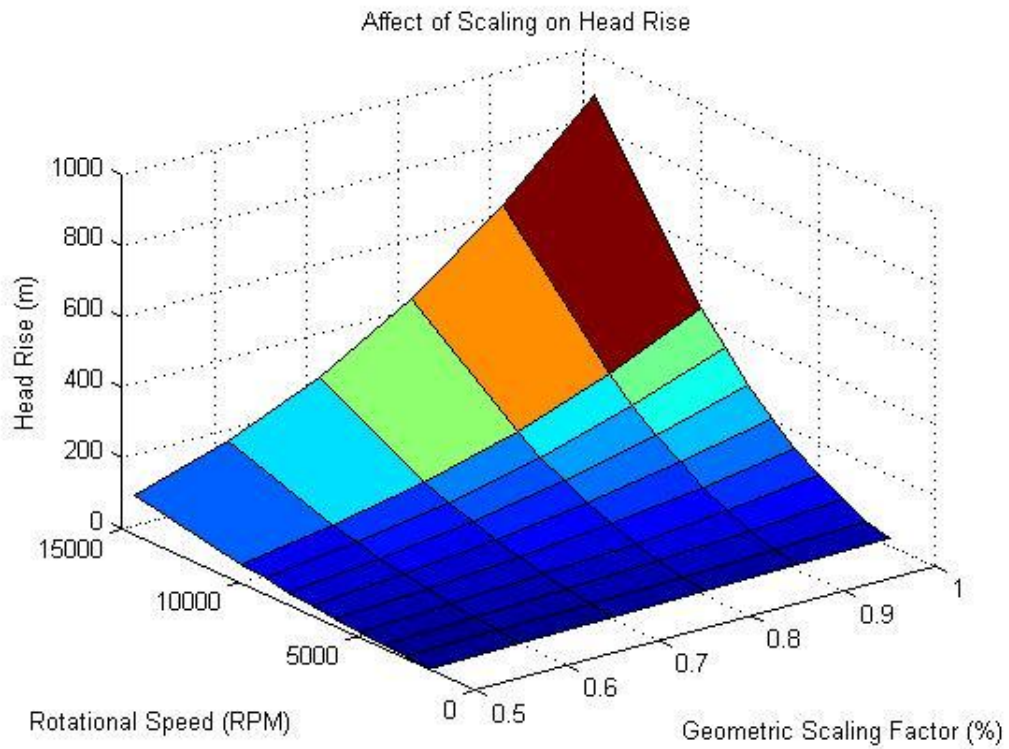


**Figure 3.8: Scaled head as a function of rotational speed and geometric scaling factor.**

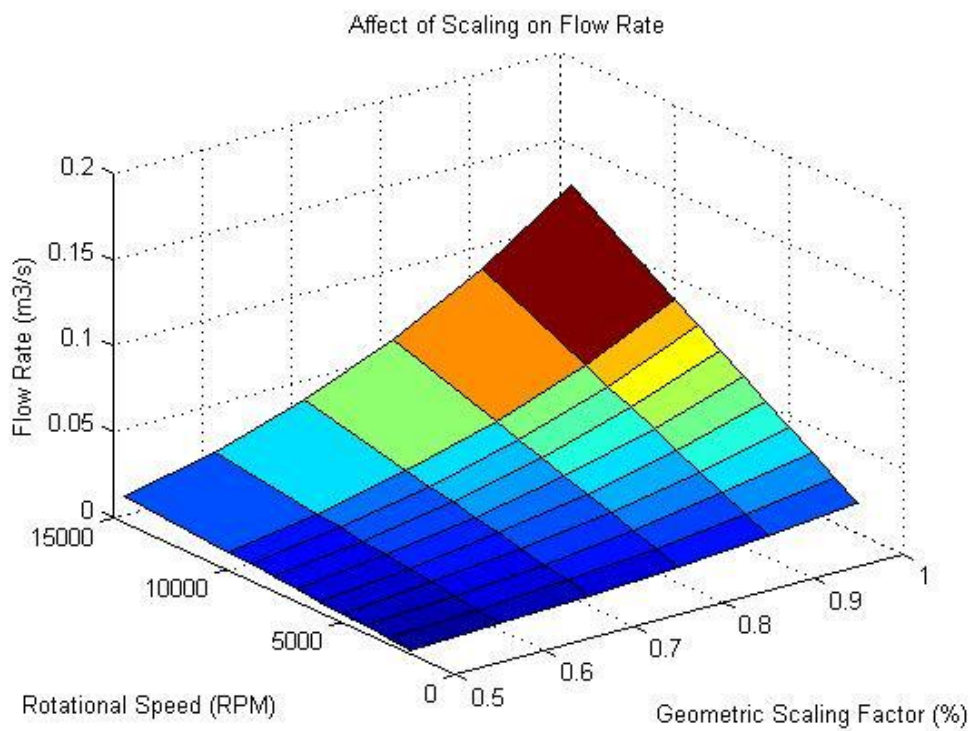


**Figure 3.9: Scaled flow rate as a function of rotational speed and geometric scaling factor.**

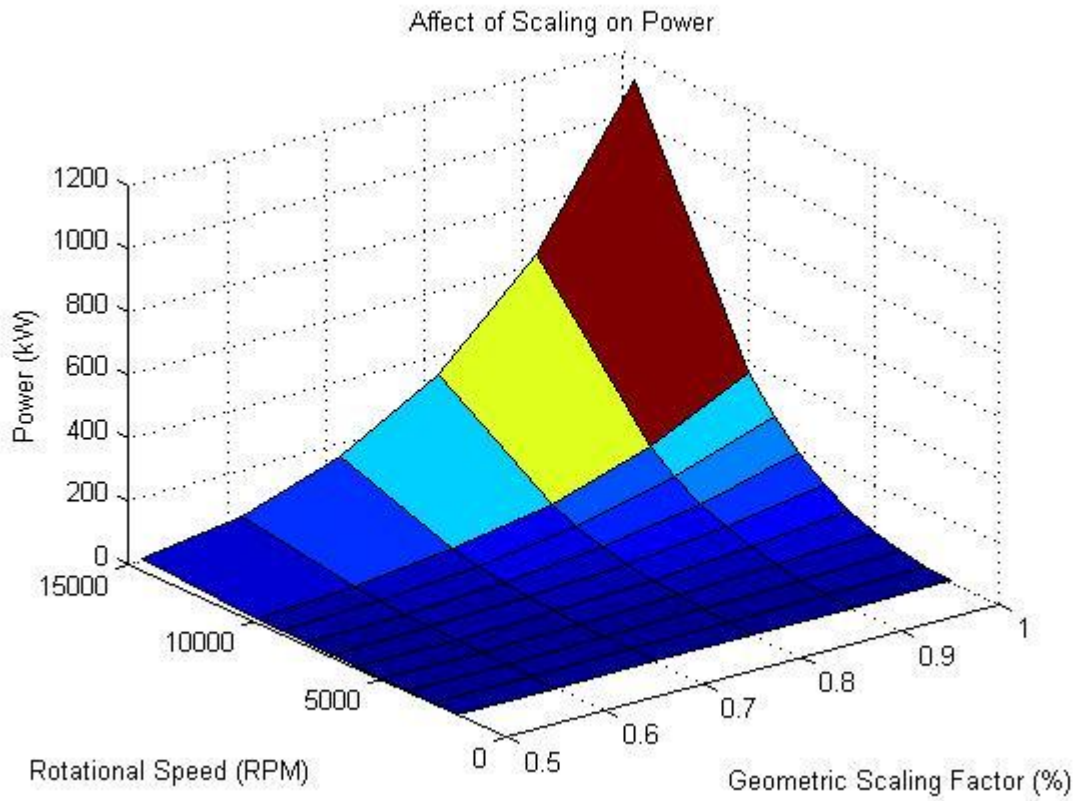


**Figure 3.10:** Scaled power as a function of rotational speed and geometric scaling factor.

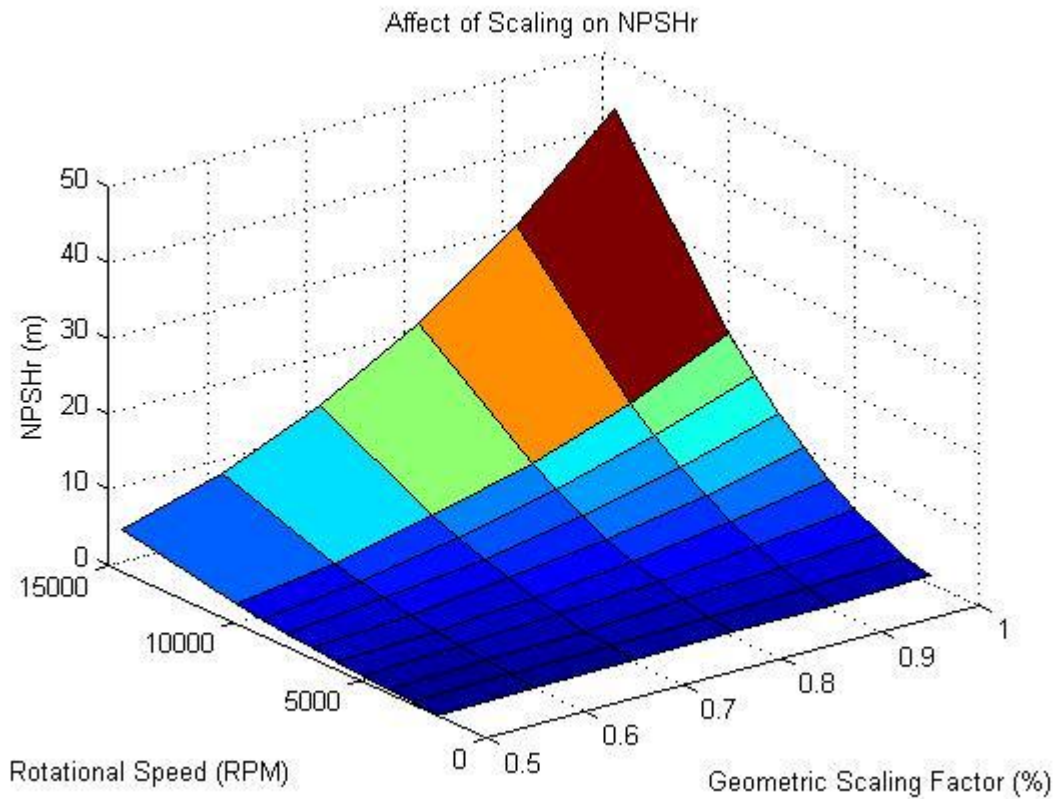


**Figure 3.11:** Scaled NPSH<sub>r</sub> as a function of rotational speed and geometric scaling factor.

### 3.3.2. Test impeller performance:

From the range determined above, final scaling parameters were selected for the impeller. A geometric scaling factor of 0.8 and a rotational speed of 5000 rpm were used in the design of the test impeller. These parameters were selected primarily on the suction requirements and to keep the geometric scaling to a minimum. The test impeller was then developed using the same PUMPAL models as the full scale, using the scaled parameters. The test impeller would then have inlet and discharge diameters of 86.88 mm and 149.36 mm respectively, with an axial length of 112 mm. The PUMPAL design for the test impeller was not completely geometrically similar. This was a result of the attempt to maintain similar flow conditions between the two impellers. The scaled design aimed to maintain the dimensionless parameters of the full scale. For this reason, adjustment of various parameters, such as the exit swirl parameter, were made. This produced a design slightly different in geometry to the full scale impeller, while maintaining constant performance parameters such as flow and head coefficients. Figure 3.12 shows both the full scale and test impellers where the reduction in size is evident.

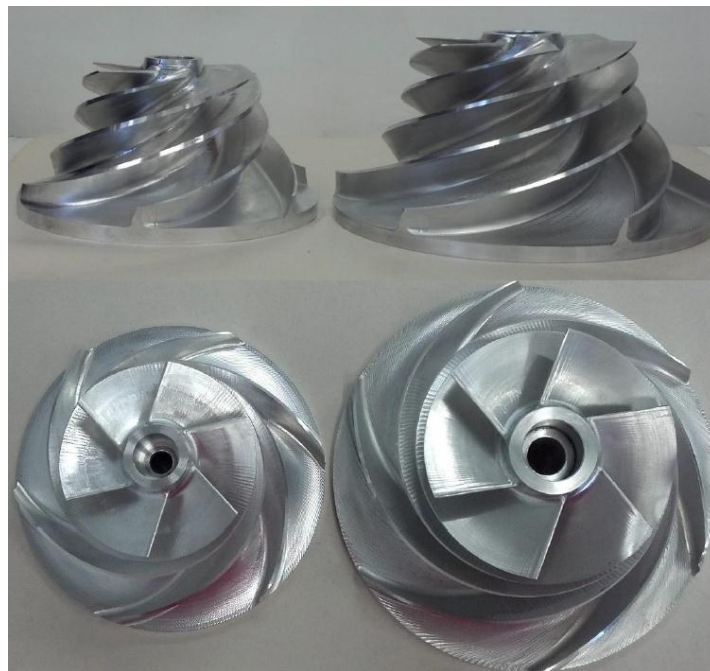


**Figure 3.12: Manufactured scaled test impeller, on left, and full scale impeller (Smyth, 2014).**

PUMPAL was then used to determine the performance of the test impeller. The test impeller design flow rate was therefore  $0.022 \text{ m}^3/\text{s}$  with a head rise of 67.7 m. Under these conditions, the  $\text{NPSH}_r$  for the impeller was 3.5 m. The power requirements of the test impeller were 15 kW. Table 3.4 shows a summary of the test impeller parameters and performance along with the full scale performance for comparison.

Table 3.4: Summary of the full scale and test impeller parameters.

	Parameter	Full scale	Test impeller
Dimensionless Parameters	Specific Speed ( $N_s$ )	1633 (U.S)	1630.5 (U.S)
	Head Coefficient ( $\psi$ )	0.463	0.444
	Inlet Flow Coefficient ( $\phi_{1t}$ )	0.2	0.21
	Corrected Suction Specific Speed ( $N_{ss}'$ )	58.64	56.18
	Blade Cavitation Number ( $\sigma_b$ )	0.087	0.091
	Exit Swirl Parameter ( $\lambda_{2m}$ )	3.9	4.0
	Secondary flow blockage (E)	0.54	0.56
Performance Parameters	Flow Rate [ $m^3/s$ ]	0.126	0.022
	Mass Flow Rate [kg/s]	103.3	18.02
	Head [m]	889	67.7
	Rotational Speed [rpm]	14500	5000
	NPSH <sub>r</sub> [m]	43.51	3.5
	Efficiency [%]	85.3	85.3
	Power [kW]	1127.8	15
Geometric Parameters	Inlet Diameter [mm]	108.6	86.88
	Outlet Diameter [mm]	186.7	149.36
	Axial Length [mm]	140	112
	Inlet Hub Blade Angle [ $^\circ$ ]	30	30.9
	Inlet Tip Blade Angle [ $^\circ$ ]	13.1	13.5
	Exit Blade Angle [ $^\circ$ ]	26	26
	Exit Absolute Flow Angle [ $^\circ$ ]	14.39	14.05

The scaled test impeller experimental results can be compared directly to the PUMPAL performance prediction of the scaled test impeller as the exact design point can be tested. This allows for a direct assessment of the accuracy of the design software predictions. This assessment will provide insight into the accuracy of the full scale, software predicted performance. Scaling of the test results to the full scale conditions will be done to experimentally predict the full scale performance. Scaling over such a large range however, can lead to inaccuracies in the scaled results. Therefore a comparison between the experimentally developed performance and the software predicted performance, with knowledge of the strengths and weaknesses of both methods, will be used to predict the actual performance of the full scale impeller.

## CHAPTER 4

### Test Rig Design

This chapter presents the design of the test rig. The objectives are presented along with any specific requirements, such as the NPSH requirements of the test impeller. Preliminary design considerations are addressed and the final design is presented. The operational envelope of the test rig is developed to determine the range of operation. All calculations and data presented in this chapter can be found in Appendix D.

#### 4.1. Objectives and requirements:

The aim of the test rig is to provide a means by which the designed test impeller can be hydraulically tested to determine the accuracy of the performance predicted by Smyth, using the design software, and hence inform the design process for future iterations.

##### 4.1.1. Testing objectives and requirements:

To achieve the above aim the following objective, obtained through testing, must be met:

- Determine the impeller characteristic curve, head rise versus flow rate.
- Determine the suction performance, plot the  $NPSH_{3\%}$  curve.
- Investigate Cavitation induced vibration and noise to identify the presence of cavitation.

Based on these testing objectives the requirements of the test rig were identified to be:

- Determine the head rise across the pump, knowledge of the inlet and outlet pressures, for varying system heads and flow rates.
- Determine change in TDH with a reduction in  $NPSH_a$ .
- Monitor vibration and noise levels while reducing  $NPSH_a$ .

#### **4.1.2. Design requirements:**

In order to meet the test requirements, the design of the test rig must provide the following (Patel and Bro):

- Fluid source and sink.
- Pipe work to route the fluid from source to pump to sink.
- Volute, shaft and bearing assembly to house the test impeller.
- A power source to drive the impeller with the ability to vary the speed.
- Independent control of the inlet and system head.
- Sensors and data acquisition system to measure the required parameters.

#### **4.2. Rig Design:**

As cost was a primary concern, where ever possible, use of existing components and cheaper solutions were implemented, although the use of stainless steel piping was considered mandatory to avoid fouling of the pumped fluid supply.

##### **4.2.1. Drive system arrangement:**

The test rig made use of an existing hydraulic pump and motor system to drive the pump. The drive system formed part of an existing turbine blade test rig that was modified for the purpose of this work. Use of this system meant that the design of the test rig had to be adapted to the constraints, primarily spacial, imposed by the setup of the previous rig.

The hydraulic drive made use of a Uchida, variable swashplate, hydraulic pump powered by a 75 kW electric motor, shown in Figure 4.1. As the Uchida had not been operated for a number of years, there were issues that had to be resolved before use. Damaged hydraulic hoses and the oil filter were replaced. The oil cooler in the sump of the Uchida was cracked. Brazing of the cooler's copper pipes was required to prevent leakage of cooling water into the oil supply. During initial operation of the hydraulic system, other issues arose. It was found that, while increasing the swashplate angle, thereby increasing the flow rate to and speed of the hydraulic motor, a point was reach at which no change in motor speed occurred. Increasing the swashplate angle further resulted in a rapid rise in the oil temperature and the electric current

drawn. Upon inspection of the system the problem was traced to the cross line relief manifold, shown in Figure 4.2. Inlet and outlet hoses for the delivery and return lines were connected to the manifold. Two pressure relief shuttle valves were installed in the manifold. Under normal operation, flow moves directly through the manifold from delivery inlet to outlet, then to the hydraulic motor and back through the return ports in the manifold. In the case of over pressurisation of the delivery, the shuttle valves open and allows flow directly from the delivery to return line, bypassing the motor. Increased temperatures at the delivery inlet and outlet ports, as well as at the return outlet port were noticed. It was concluded that the shuttle valves had opened prematurely. This resulted in flow passing directly through the valve, from the delivery to the return lines, creating a large temperature rise as the viscous oil was driven through the small clearances of the shuttle valves, while the flow to the motor remained constant. This accounted for the increase in the current drawn as the Uchida flow rate had increased and therefore required more power, even though no increase in motor speed occurred. To eliminate the problem, the shuttle valves were blocked so that they could not open. This meant that the outlet pressure of the Uchida had to be monitored during operation to ensure pressures didn't exceed the maximum limit.



**Figure 4.1: Uchida hydraulic pump and electric drive motor.**



Issues with the electrical control circuitry, shown in Figure 4.3, had to be resolved before use. It was found that the circuitry behaved erratically when the off-breaker was triggered. Either a dip in power would occur but the motor would continue to operate, or the power would trip. Testing of the control circuitry revealed that the off-breaker switch had a fault. The off-breaker switch was replaced; the new white switch can be seen in Figure 4.3. This final problem was therefore eliminated and the hydraulic pump could then be operated continuously without overheating or incurring electrical faults.

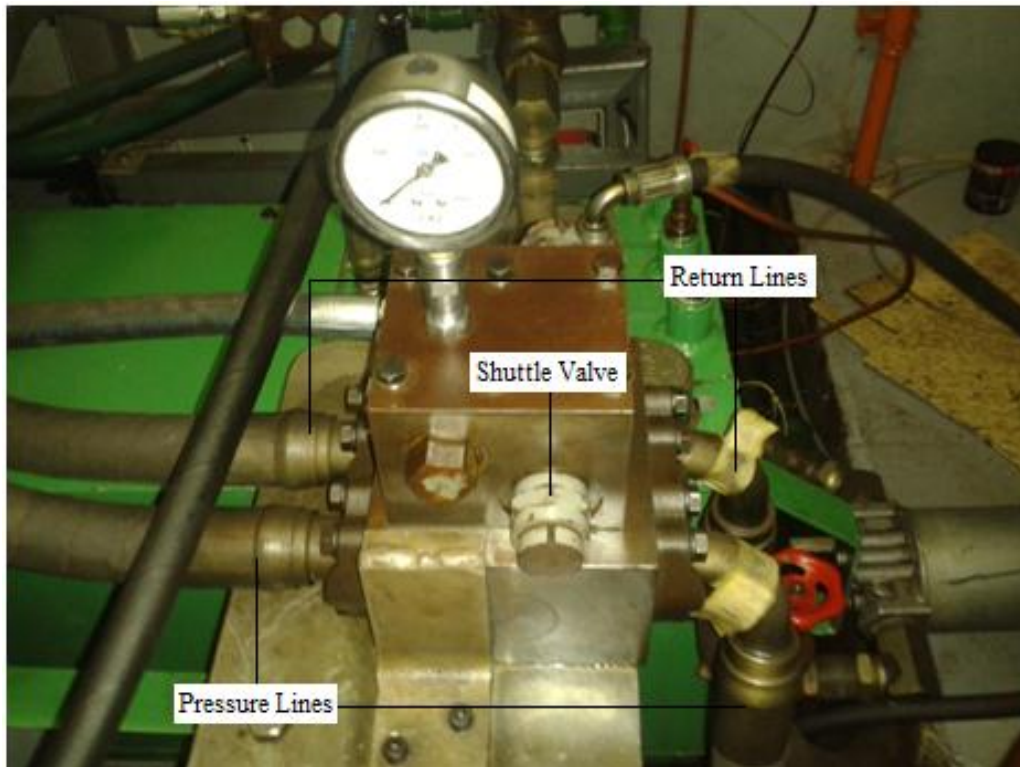


**Figure 4.2: Cross line relief manifold where overheating occurred.**

The Uchida hydraulic pump drove a Sundstrand 65 kW, fixed swashplate, hydraulic motor. The original routing of flow caused the motor shaft to rotate in the wrong direction. The hoses to the motor were switched in order to reverse the motor direction. The motor was coupled to a 1 : 6 speed increasing gearbox. A maximum motor speed of 3000 rpm was achievable, giving a maximum gearbox output speed of 18000 rpm. The motor, gearbox and pump assembly can be seen in Figure 4.4. An oil heater and pneumatic vane pump subsystem was used to provide lubrication to the gearbox.

Control of the motor speed was achieved by varying the swashplate angle of the Uchida hydraulic pump. Control of the swashplate angle was done using a lever on the side of the Uchida. A lead screw mechanism, using a DC motor and threaded bar, was implemented to allow accurate control of the swashplate angle, as seen in Figure 4.5. A hinged joint attached



Figure 4.3: Electrical control circuitry with replacement off breaker.



Figure 4.4: Hydraulic motor, gearbox and motor assembly.

the DC motor to the Uchida frame to allow for the change in angle created by the moving lever. Control of the DC motor was done through an existing panel, shown in Figure 4.6. The panel allows for coarse and fine adjustment of the swashplate angle as well as displays the motor shaft speed.

Although the hydraulic drive system had sufficient power to drive the test impeller, torque requirements had to be determined in order to ensure that the test conditions could be met. For a hydraulic motor, the torque is proportional to delivery pressure. Therefore the limiting factor, with regards to torque, is the maximum allowable pressure. As no specifications, with regards to torque, for the motor were available, the expected delivery pressure, for test conditions, had to be calculated based on the previous operation of the rig. The previous turbine blade test rig ran an impeller at 18000 rpm, consuming approximately 50 kW, based on the sizing of the motor. The pressure maximum pressure that the system ran at was 220 bar. This was the pressure at which the over-pressure relief valves had opened previously. Based on the proportional relationship between torque and delivery pressure, the motor power can be defined as:

$$\text{Power} = knp_1 \quad [4.1]$$

where  $n$  is the shaft speed,  $p_1$  the inlet pressure to the motor and  $k$  is a constant of proportionality which accounts for the specific motors relationship between inlet pressure and torque. Based on the parameters determined above, a value of 0.0126 for  $k$ , having the units of W.min/bar, was calculated. Making  $p_1$  the subject of the formula, and using values of 5000 rpm and 15 kW, the expected delivery pressure under test conditions was determined. A delivery pressure of 240 bar was calculated for the test conditions. The maximum pressure rating on the Uchida name plate was 340 bar, therefore the drive system was sufficient to provide the required torque.

A KSB ETA 125-200 pump was used in the validation of the test rig. Once validation is complete, the pump will be modified to house the test impeller. A Burgmann mechanical shaft seal was installed, replacing the original stuffing box, to allow for high speed operation. The dimensions of the pump can be found in Appendix 1. It was required that the pump be raised off its mounting table in order to line up with the gearbox shaft. Two 100 x 200 mm steel box sections, 250 mm long, were welded together to form the pump base. Two C – channel, 100 mm long, sections were welded to the sides of the box section to provide lateral stability. Slots cut into the bottom and top of the box section and C- channels allowed for positioning of the pump while aligning the shafts. The pump and pump base can be seen in Figure 4.4.

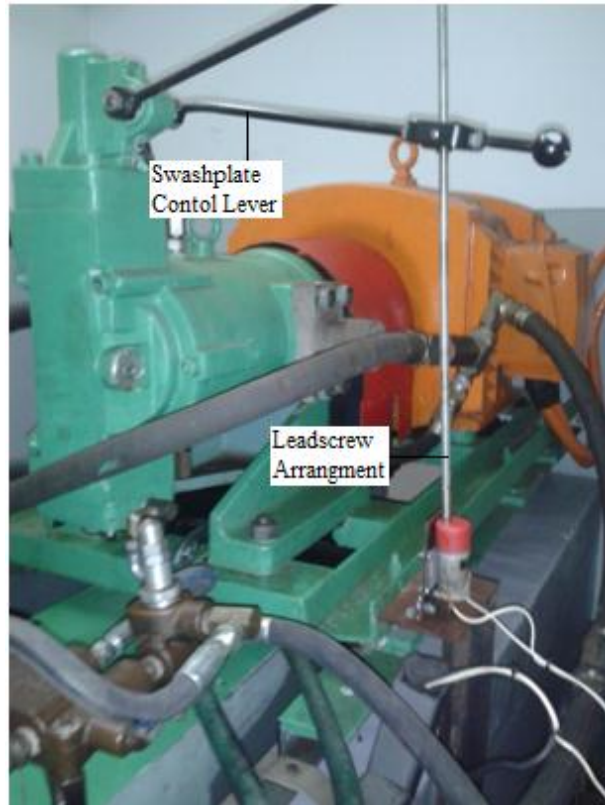


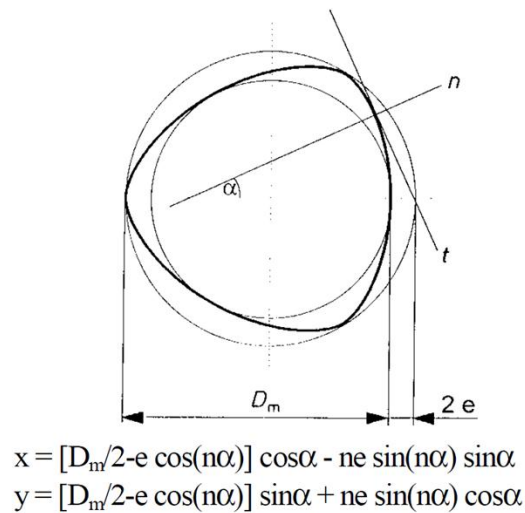
Figure 4.5: DC motor lead screw arrangement for the Uchida swashplate angle control.



Figure 4.6: Panel containing motor speed display and swashplate angle control switches.

Laser shaft alignment was used to position the pump. Shims were used for the fine adjustment of the pump position. Alignment within 0.3 mm was achieved, which was within the tolerances of the gear type coupling used, see Appendix 1 for coupling specifications. The output shaft of

the gearbox had a unique polygon profile, shown in Figure 4.7. Figure 4.7 also shows the formula used to generate the profile, where  $D_m$  is the mean diameter,  $e$  the eccentricity and  $n$  the number of lobes. For the gearbox shaft, values of 36 mm, for  $D_m$ , 1.2 mm for  $e$  and 3 lobes, defined the profile. The gear type coupling used had this polygon profile cut into one side of it and a shaft and keyway profile, for the pump shaft, cut into the other side. MATLAB code was used to generate the polygon profile and the points were transferred into CAD software Inventor, to produce the 3D model that was used to machine the profile. The pump side of the coupling had a 32 mm bore, with a 10 mm wide keyway, cut into it to match the pump shaft. Grub screws were inserted above the keyway to lock the key in place.



**Figure 4.7: Gearbox polygon shaft profile with defining equations.**

#### 4.2.2. Pipe system:

The design of the pipe work was largely defined by the spatial constraints imposed by the location of the drive system and the  $NPSH_r$ . A closed loop design was used for the test rig, utilising a reservoir, where water was drawn from and returned to. Use of a pressure vessel, as the reservoir, was not considered due to the high costs of fabrication. Therefore a reservoir, open to atmosphere, had to be used. From this selection, two requirements of the inlet piping design were established. Firstly, without the ability to control the reservoir pressure, throttling of the suction lines was required to adjust the inlet pressure to the pump. Secondly, as the reservoir could not be pressurised, adequate NPSH had to be achieved by raising the reservoir to a sufficient height above the pump inlet. A  $NPSH_r$  of 3.5 m, required for testing, meant that the water level in the reservoir had to be raised above 3.5 m, to account for losses in the inlet piping. A mezzanine level, adjacent to the test room, was selected as the location for the

reservoir. This provided a maximum elevation of approximately 3.8 m above the pump inlet. A 2500 l water tank was used as the reservoir, as seen in Figure 4.8. Modifications to the tank were made to allow for the inlet piping to enter from below, while the discharge was routed to the top of the tank, through a pre-existing hole. The inlet was extended 400 mm into the tank to ensure no sediment, settled on the bottom of the tank, would be drawn in. The flow was discharged below the water level to reduce the amount of air dissolved in the water. A stand was designed and fabricated to raise the tank to the highest elevation, thus providing the maximum  $NPSH_a$ .



**Figure 4.8: Supply tank with base to raise its level. The inlet pipe enters from the bottom and the discharge pipe enters from the top.**

Stainless steel piping and fittings were used in the design of the test rig to ensure no corrosion occurred. Pipe diameter was selected based on the expected flow rate and the consequent losses in the inlet line. Figure 4.9 shows  $NPSH_a$  based on the test impeller flow rate and the height of the tank. Both inlet pipe length and diameter were varied to determine the range in which each parameter would satisfy the  $NPSH_r$  of the test impeller. It can be seen that, with the available height, the  $NPSH_r$  of 3.5 m cannot be met. While the test impeller was designed for 5000 rpm, performance information was calculated for lower speeds. A reduction of 1000 rpm in shaft speed produces a  $NPSH_r$  of 2.2 m, see Figure 4.19. Therefore the test rig could still meet the

testing objectives, although at a lower speed than originally specified, to allow for adequate  $NPSH_a$ . Taking into account the position of the tank relative to the pump, an estimate inlet pipe length of 15 – 20 m was used for pipe diameter selection. Pipe diameters similar to the inlet diameter of the test impeller were preferential. From Figure 4.9 it can be seen that, for the range of inlet pipe length considered, pipe diameters less than 100 mm result in a significant reduction in  $NPSH_a$  and could therefore not be considered. Diameters above 100 mm did not provide significant enough improvements in  $NPSH_a$  to justify the added cost of the larger pipe. Thus 100 NB piping was used in the design of the test rig. Schedule 10 piping was sufficient for the pressure levels in the system. For rig validation, a 2.5 m length of 150 NB schedule 10 pipe was used directly before the pump inlet, to match the pump inlet flange diameter. Once the test impeller has been fitted, this length of inlet pipe will be replaced with one matching the impeller inlet diameter.

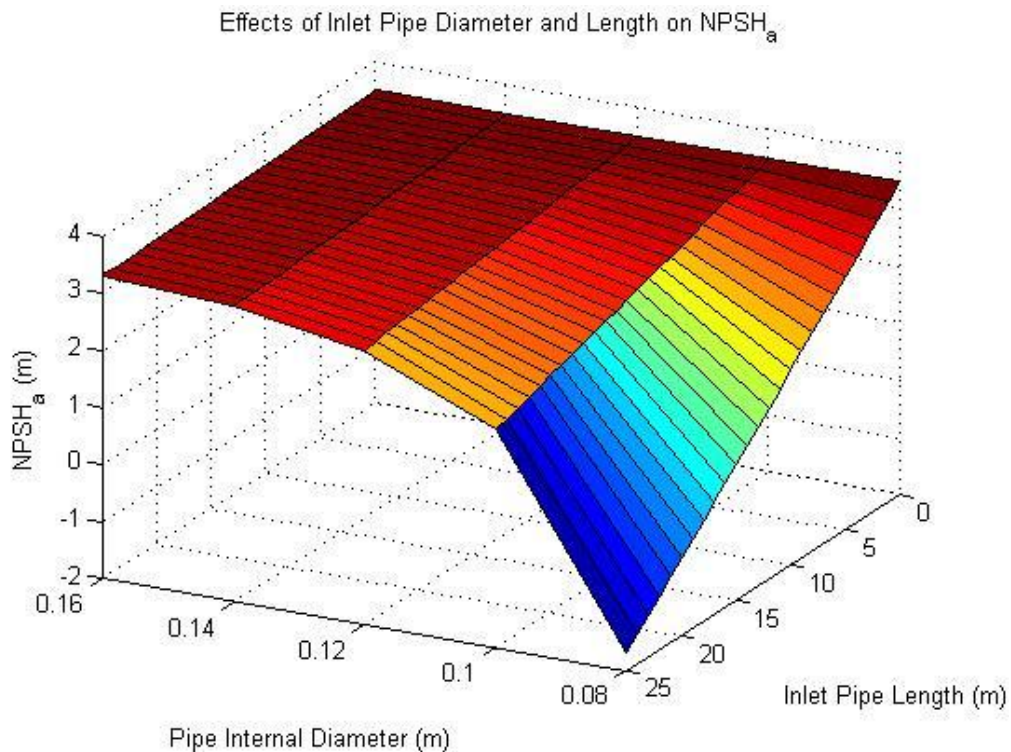


**Figure 4.9: Effect of inlet pipe length and diameter on  $NPSH_a$ , used to select an adequate pipe diameter.**

A 3D model of the test rig layout is shown in Figure 4.10. The final layout has total straight inlet and discharge pipe lengths of 15 m and 10 m, respectively. Four, long radius bends, were used on the inlet line, and five on the discharge line. 100 x 150 NB and 100 x 125 NB reducers were used to connect the piping to the pump inlet and discharge flanges respectively. A 100 NB butterfly valve was installed in the inlet line to provide control of the pump inlet pressure, thus facilitating cavitation testing. Two identical butterfly valves were installed in the discharge line, for control of the system head. Two valves were used to improve the resolution of the

system head control. This is particularly important during cavitation tests as changes in system head, due to inlet throttling, must be accurately negated by the valves in the discharge line to ensure a constant flow rate. The valves in the inlet and discharge lines were placed close to each other, as seen in Figure 4.11. This simplified the operation of the test rig as all the valves could be manipulated from one position.

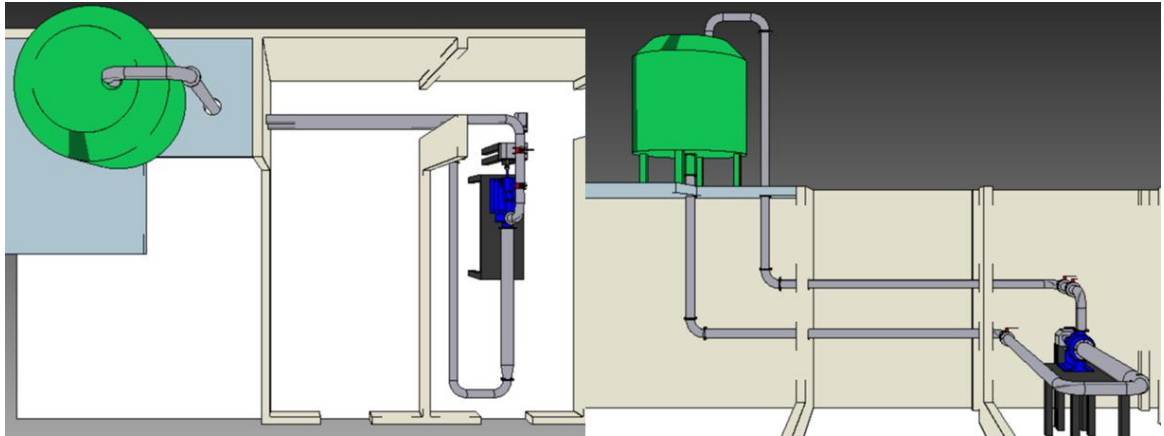


**Figure 4.10: 3D model of the test rig layout.**

Pipe lengths had to be sized to accommodate the spacial constraints. The inlet piping was divided into six individual pieces and the discharge line five. A 2.5 m straight inlet pipe section was used to ensure well developed flow at the inlet to the impeller. These individual pieces had flanges welded to their ends to allow them to be connected once they were in place. The



**Figure 4.11: Position of the valves. The inlet valve is at the bottom and the two discharge valves at the top.**





**Figure 4.12: A section of the inlet and discharge piping. Holes cut through the wall can be seen on the left. Supports for the inlet line (bottom) and discharge line (top) can be seen.**

routing of the pipes required two holes to be cut through a wall, as seen in Figure 4.12. Two stub pipes were made to sit in the holes and flanges were then welded in place. The inlet piping runs below the discharge line, as seen in Figure 4.10. Therefore the inlet line had to be supported from below and the discharge line from above. Floor mounted stands were made, with screw adjusters, to support the inlet line at the height of the pump inlet. On the other hand, the discharge line was suspended from the ceiling by M 12 threaded bar, attached to the ceiling with rawl bolts. A collar with a swivel attachment was used to attached the pipe to the threaded bar. Figure 4.12 shows the two types of supports used. A summary of the pipe lengths and fittings used in the test rig design is given in Table 4.1 below.

**Table 4.1: Summary of pipe lengths and fittings used the test rig design.**

Components		Quantity		
		Inlet Line	Discharge Line	Total
Pipe Length [m]	100 NB	11.79	9.48	21.27
	150 NB	2.5	0	2.5
Reducers	100 x 150 NB	1	0	1
	100 x 125 NB	0	1	1
Long Radius Bends (90°)		4	5	9
Valves		1	2	3

### 4.2.3. Sensors and data acquisition system:

In order to meet the test objectives, knowledge of the following parameters were required:

- Inlet and discharge pressures of the pump. Inlet pressure will be used to determine suction performance and the difference between the outlet and inlet will define the head rise across the pump.
- Temperature of the inlet flow. Temperature determines the vapour pressure of the fluid, used for suction performance analysis.
- Flow rate for varying system heads.
- Rotational speed of the impeller.
- Vibration levels of the pump housing.
- Sound levels.

Motor speed was measure with an existing hall-effect inductive pick-up, as seen on the motor shaft in Figure 4.4. At inlet, two pressure transducers were used to measure the inlet pressure. A WIKA A-10 pressure transducer was used to measure pressures above atmosphere. The transducer has a range of 0-1 bar. This was adequate to measure the maximum possible inlet pressure of approximately 0.38 bar. A WIKA S-10 vacuum transducer was used to measure inlet pressures below atmosphere. The range of the transducer was -1-0 bar. An A-10 transducer, with a range of 0-10 bar was used at the discharge of the pump. All transducers produced a 4-20 mA signal proportional to the applied pressure. RTD temperature sensors were installed in the suction and discharge line. The RTD's had a range of 0-70°C. RTD's are resistance devices and therefore transmitter devices had to be installed to convert the output from the RTD's to a 4-20mA signal. An accelerometer based vibration sensor was installed on the inlet flange of the pump. The sensor integrates the accelerometer signal to provide a 4-20 mA output signal proportional to vibration velocity, measured in mm/s. The maximum vibration velocity capable of been measured with the sensor was 20 mm/s. The vibration sensor produced an output proportional to the RMS level of vibration for a range of 10-1000 Hz. This meant that only the total vibration level could be determined, and no information with regards to the specific vibration frequencies could be obtained. Figure 4.13 shows the instrumentation section around the pump inlet. The two pressure transducers can be seen on either side of the inlet pipe. The discharge pressure transducer was installed on the pump just before the outlet. RTD's in the inlet and discharge line can be seen. The vibration sensor can be seen attached to the inlet flange of the pump. A SAFMAG beta meter electromagnetic flow meter was installed in the discharge line, clamped between flanges, as seen in Figure 4.14. The flow meter could

detect a minimum fluid velocity of 0.1 m/s, however a minimum of 0.5 m/s is recommended for improved accuracy. A control box, provided with the flow meter, allowed for selection of the measurement mode and units, displayed the current flow rate and outputted a 4-20 mA signal to the DAQ system.

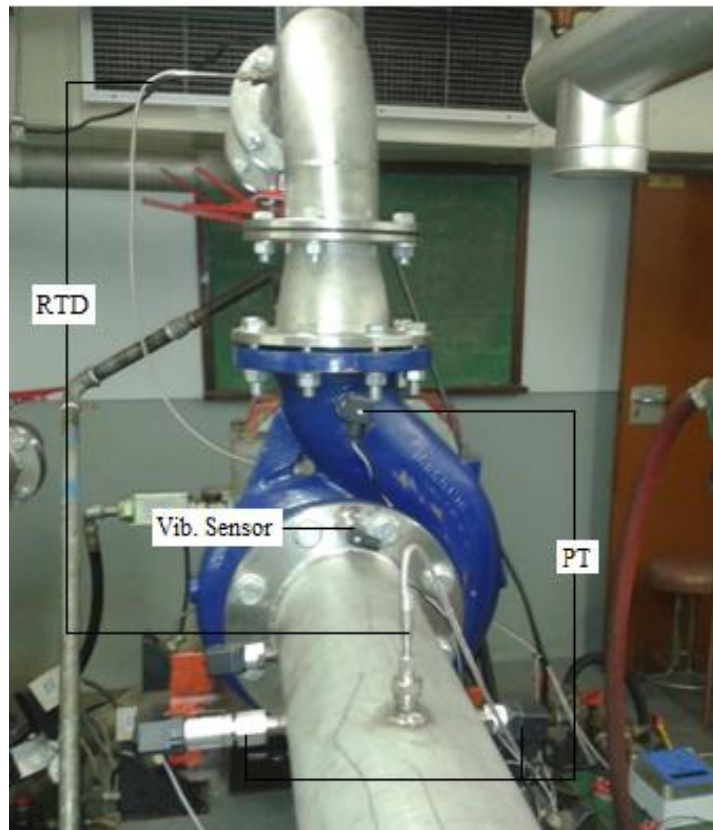


Figure 4.13: Instrumentation section of the test rig.



Figure 4.14: Flow meter clamped between flanges in the discharge line.

Sound levels were recorded with a USB M-Audio studio microphone positioned against the volute of the pump. A 12 VDC power supply was used to power all the sensors other than the flow meter, which ran directly off mains, and the microphone, which was powered through the USB connection. National Instruments (NI) DAQ hardware and software were used to display and log the instrument data. A NI cDAQ-9174 USB chassis, with a NI 9203 4-20 mA input module was used for data acquisition. Figure 4.15 shows the NI chassis and input module along with the power supply, flow meter control box and RTD transmitter. Instrumentation specifications and pump dimensions can be found in Appendix B.

NI LabVIEW software was used to display and log data coming from the sensors. Figure 4.16 shows the front panel of the virtual instrument created in LabVIEW. Inlet gauge and vacuum pressures, as well as total dynamic head are displayed on dials. Outlet pressure is displayed on a dial as well. Temperature thermometer displays are used for inlet and discharge temperatures. Flow rate and rotational speed were also displayed. Waveform graphs were used to display the vibration and sound levels. Control buttons, for selecting when to log data and record sound, were implemented. Operation of the visual instrument was setup in the block diagram shown in Figure 4.17. A DAQ assistant block was used to setup communications between the NI hardware and LabVIEW. With this block specific channels were setup for each sensor and scales were applied to each channel to convert the 4-20 mA signals into the specific units for the particular sensor. The DAQ assistant block outputs signals to each of the display gauges on the front panel. Outputs from the DAQ assistant block were also sent to an EXCEL spreadsheet



**Figure 4.15: NI DAQ hardware, power supply, flow meter control box and RTD transmitter used for data acquisition.**

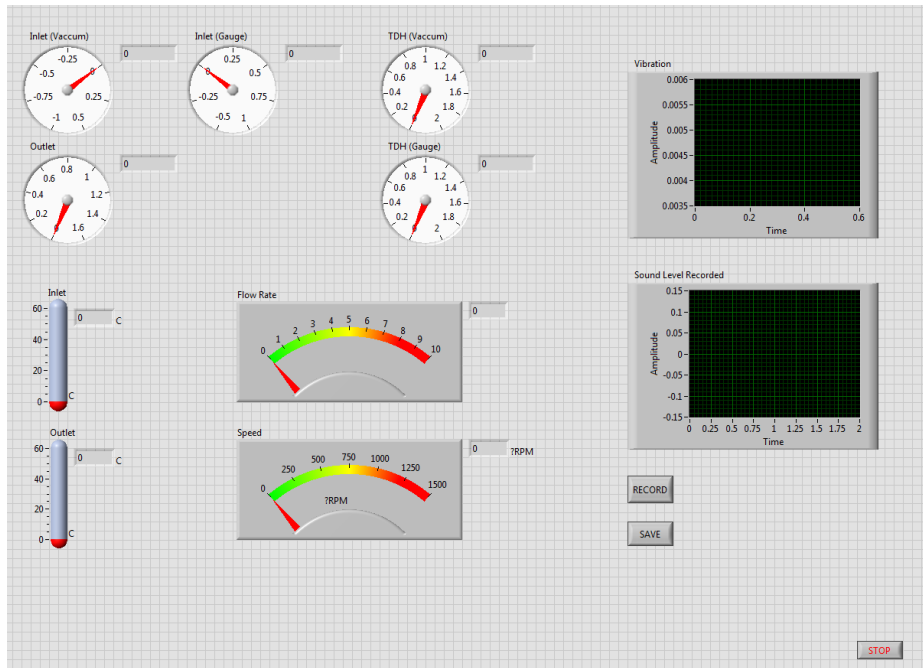


Figure 4.16: Front panel of LabVIEW virtual instrument.

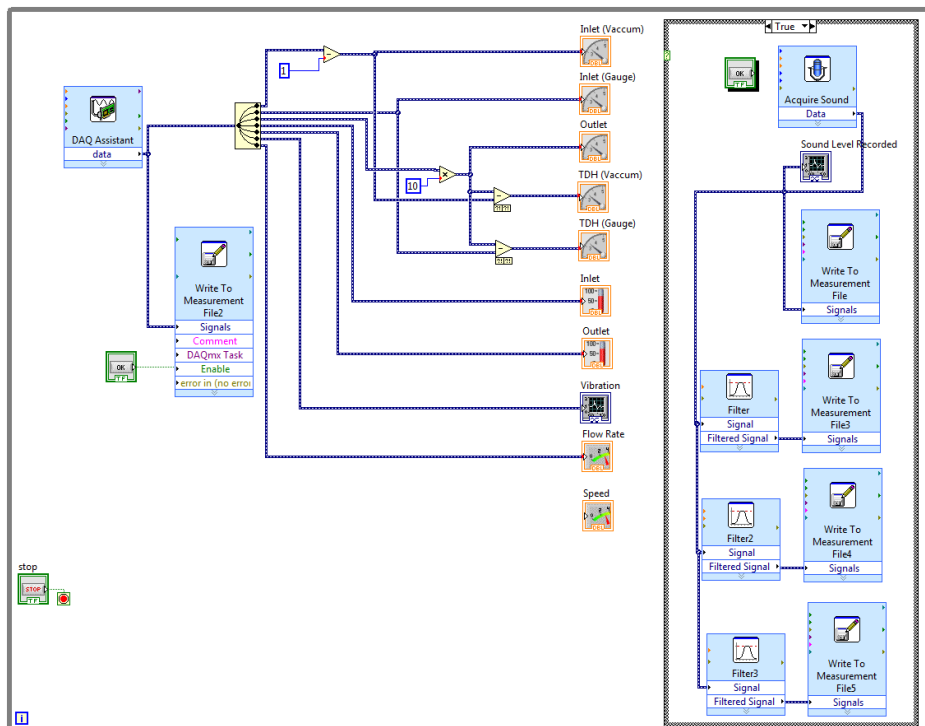


Figure 4.17: Block diagram of LabVIEW virtual instrument.

logging block. This logging action was initiated by clicking the save button on the front panel. A separate loop structure was used to record noise levels. This loop was activated using the record button on the front panel. The recorded noise levels were saved in an EXCEL spread

sheet. Low, band and high pass filters were applied to the sound signal and saved along with the unfiltered signal.

#### 4.4. Test Rig Operational Envelope:

With the final design of the test rig known, a 1D analysis was performed to investigate the test rig limits and define its operational range. Of primary concern was the  $NPSH_a$  that the test rig could produce. Figure 4.18 shows the calculated inlet pressure, in bar, for a flow range of 0 – 0.035  $m^3/s$ . Without throttling of the suction line, which would be done for suction performance tests, the inlet pressure will range between a maximum of 0.38 bar, at zero flow, to a minimum of 0.094 bar, at maximum flow. At the test impeller design flow rate of 0.022  $m^3/s$ , the inlet pressure would be 0.26 bar. The reduction in inlet pressure, as flow rate is increased, is a result of the increasing dynamic head component of the flow as well as the increased frictional losses due to the higher fluid velocity in the pipes.

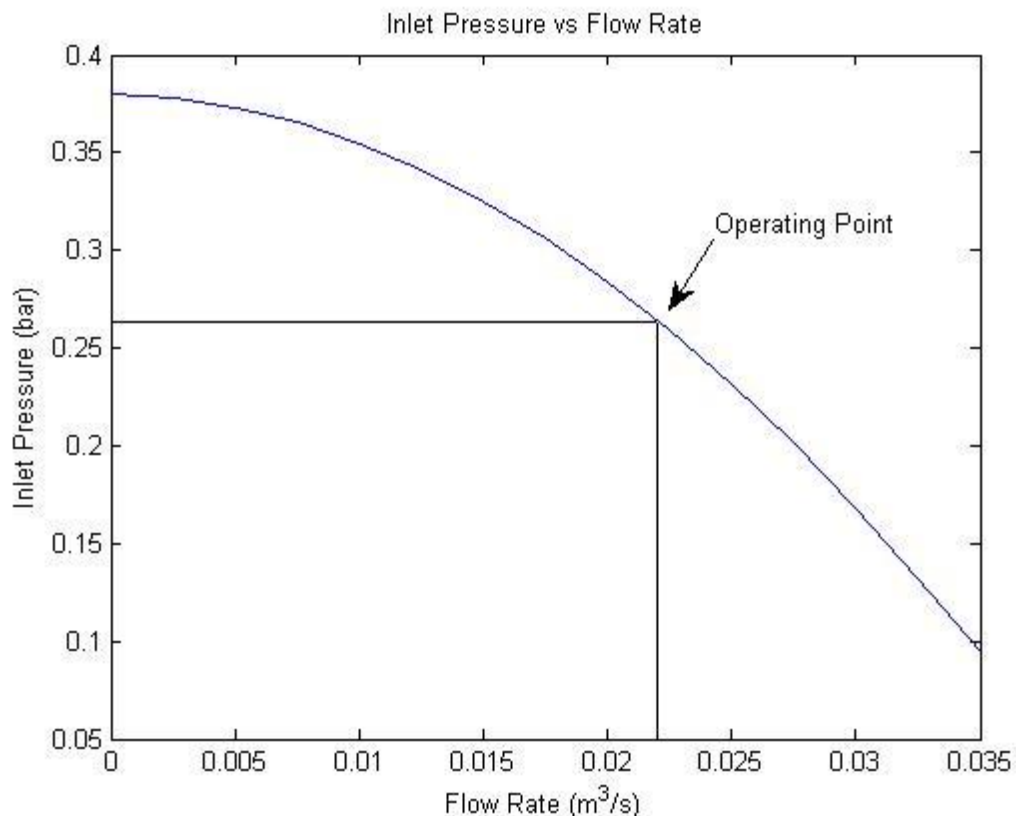
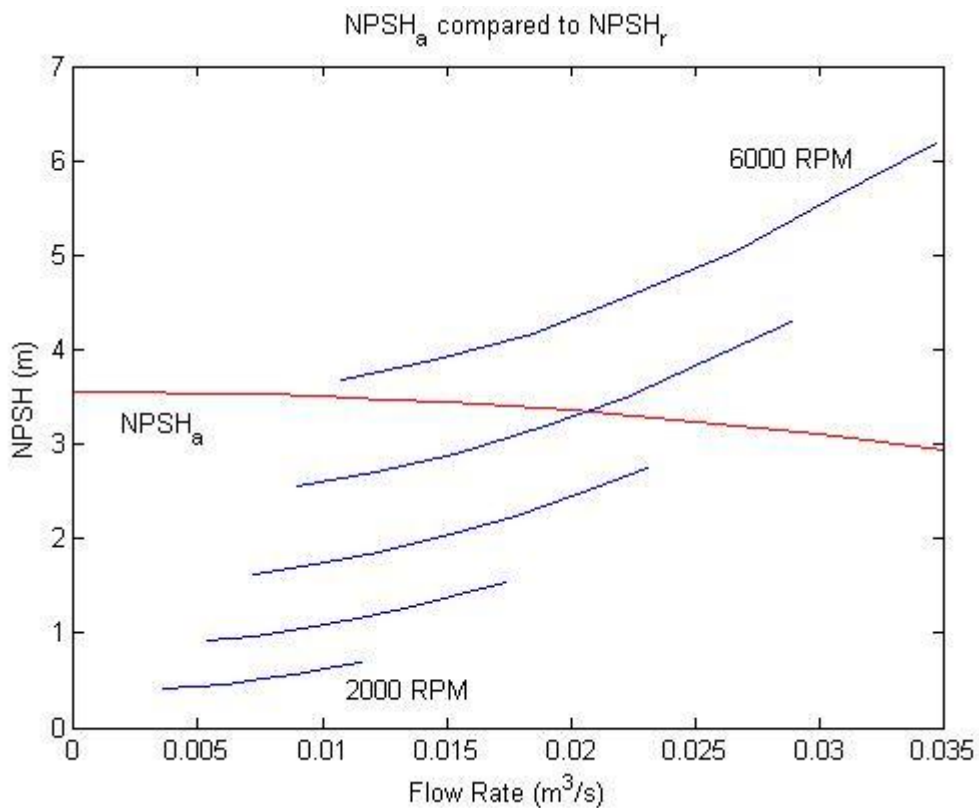


Figure 4.18: Pump inlet pressure as a function of flow rate.

The  $NPSH_a$  of the system is shown in Figure 4.19 as the red line.  $NPSH_a$  for the test rig varies from 3.552 m at zero flow to 2.941 m at maximum flow. Also shown in the figure are the

$NPSH_r$  curves for the test impeller, for speeds of 2000 rpm (bottom curve), increasing in increments of 1000 rpm, to 6000 rpm calculated using PUMPAL. From the figure it can be seen that the  $NPSH_r$  for speeds of 4000 rpm and below are met by the  $NPSH_a$  of the test rig. Speeds of 6000 rpm and above would not have adequate  $NPSH_a$  to be operated without cavitation. The intersection of the  $NPSH_a$  curve with the  $NPSH_r$  curve for 5000 rpm gives a flow rate of  $0.0207 \text{ m}^3/\text{s}$ . This flow rate is below the test impeller design point flow rate of  $0.022 \text{ m}^3/\text{s}$ . Therefore there is inadequate  $NPSH_a$  to test the scaled impeller's design point at 5000 rpm. A quadratic trend line was applied to the  $NPSH_a$  curve in MATLAB. Using the trend line equation and the scaling laws, the maximum speed at which the design point  $NPSH_r$  was met could be calculated. In this case a reduction in the rotational speed, to 4900 rpm, during testing would be required for the  $NPSH_r$  of the test impeller to be met. In the same way, the maximum speed at which the entire performance characteristic curve could be tested, without the development of cavitation, was calculated to be 4363 rpm. Throttling the inlet line would increase the losses and reduce the  $NPSH_a$  so that suction performance could be determined for lower speed operations.



**Figure 4.19:  $NPSH_a$  and  $NPSH_r$  for the test rig and impeller.**

The system head curve for the test rig, with no throttling of the suction or discharge line, is shown in Figure 4.20. As the discharge is returned below the water level of the tank, there is no difference between the inlet and discharge heights. For this reason, the system head has a value

of zero, at zero flow. The rapid increase in system head is due to the increase in losses, proportional to the square of velocity, as flow rate is increased. The maximum system head, for the flow rate range considered, was 3.961 m. The operating envelope of the test rig is shown in Figure 4.21. In the figure, the blue lines are the performance characteristic curves for the test impeller, at rotational speeds of 2000 rpm to 6000 rpm, in increments of 1000 rpm, as calculated by PUMPAL. The green line depicts the design point of the impeller for all flow rates in the range considered. The limiting conditions of the test rig are represented by the red lines in the figure. The horizontal red line, at 100 m or 10 bar, represents the maximum allowable pressure in the piping. Therefore, only pressures below this line can be produced safely in the test rig. This limit is sufficient to allow for the maximum pressure of the test impeller, of 98 m at 5000 rpm, to be measured. The red curve along the bottom of the figure is the system head. This line represents the minimum conditions that can be achieved on the test rig. It can be seen that for all the considered rotational speeds, the performance characteristic curves for the test impeller lie above the system head curve and therefore satisfy the minimum requirements of the test rig. Throttling of the inlet or discharge line will cause the system head curve to rise more sharply, as resistance to flow is increased. With correct control of the throttle valves, the system head curve can be made to intersect the test impeller's performance

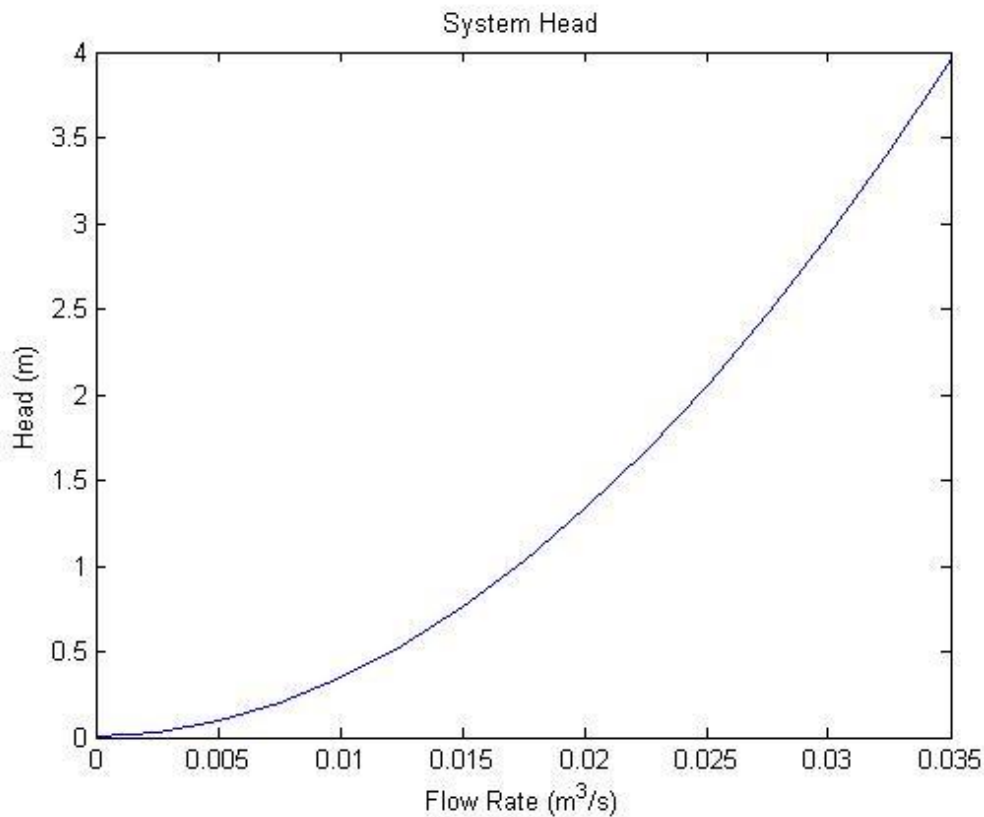
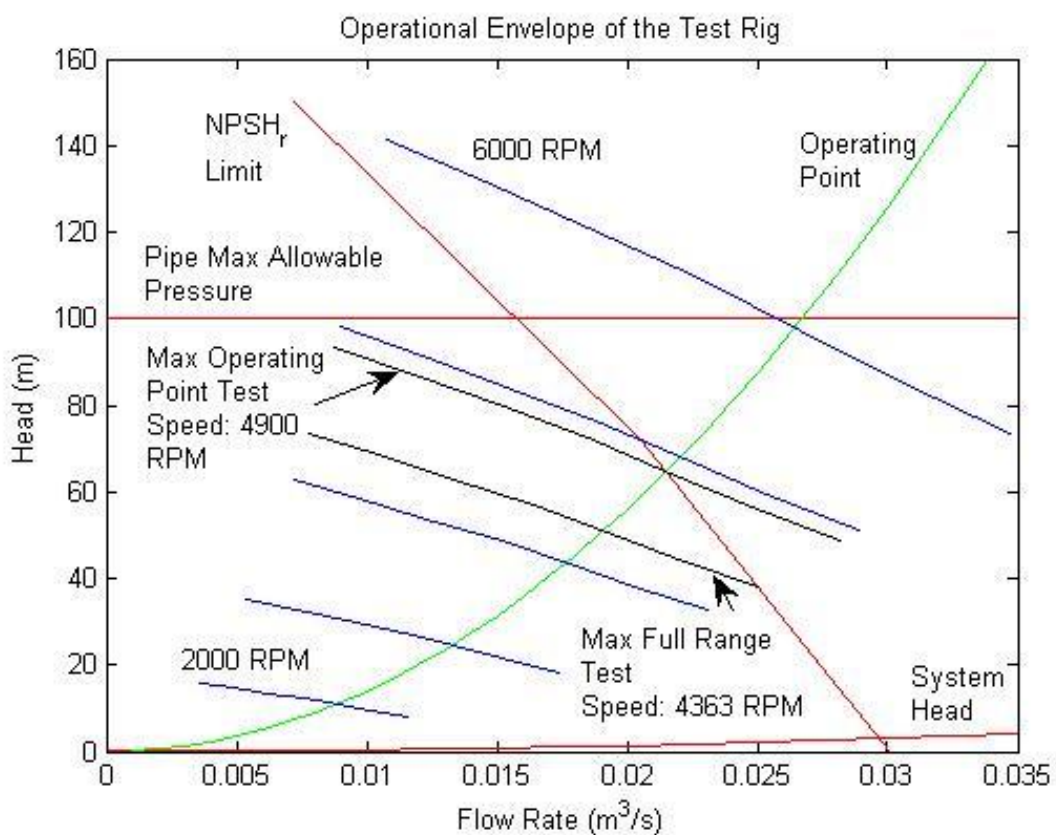


Figure 4.20: System head curve for the test rig, with no throttling of the inlet or discharge line.



characteristic curve anywhere within the operational envelope of the test rig. The final red line, moving from top left to bottom right, represents the  $NPSH_a$  limit for the test rig. This line was determined from Figure 4.19 by applying quadratic trend lines to each  $NPSH_r$  curve and projecting them to intersect the  $NPSH_a$  curve. The point of intersection defined the maximum flow rate, for each rotational speed considered, at which the  $NPSH_r$  was met. These flow rates were then used to locate the point on the performance characteristic curve at which  $NPSH_a$  was sufficient. As only the flow rate determined for 5000 rpm fell on the defined performance characteristic curve, trend lines were used to extend the performance characteristic curves for the other rotational speeds to predict the operating point at which the  $NPSH_r$  were met. All operating points that lie to the left of this line will have adequate  $NPSH_a$  to operate without cavitation. The area enclosed by the three limiting lines defines the operational envelope of the test rig. In Figure 4.21 the black plots represent the performance characteristic curves for two particular rotational speeds. The upper line represents a rotational speed of 4900 rpm, the maximum speed at which the  $NPSH_r$  at the design point could be met. The lower line represents a speed of 4363 rpm, the maximum speed at which the entire defined range of operation, for the test impeller, has sufficient  $NPSH_a$ . These two speeds represent the limits at which testing can be done with regards to the design point and entire defined range.



**Figure 4.21: Operational envelope of the test rig. Test impeller performance characteristic curves shown in blue. Design point is shown in green for all flow rates considered.  $NPSH_a$ , maximum pressure and system head limits are shown in red. Critical test points are shown in black.**

## CHAPTER 5

### Experimental Results

This chapter presents the result of the validation testing of the test rig. Supplier data for the KSB pump used to evaluate the test results is presented. A description of the testing procedures used is given. The performance characteristic curve determined experimentally is presented and compared to the supplier curve to assess the accuracy of the test rig. Suction performance test results, based on head rise, vibration and noise levels are presented. Comparisons between the results from the different methods of cavitation testing are made to better define the suction performance of the impeller and to investigate the benefits of each method. All calculations and experimental data used in this chapter can be found in Appendix E.

#### 5.1. KSB ETA 125 – 200 Data:

Validation of the test rig was done using the standard KSB ETA 125 – 200 centrifugal pump. The results obtained on the test rig were compared to the supplier data to determine the repeatability of the test rig and data acquisition system results, and therefore provide validation. Figure 5.1 shows the supplier performance characteristic curve (top),  $NPSH_r$  curve (middle) and power curve (bottom) for the KSB impeller. The data was obtained at a rotational speed of 1450 rpm, for impeller diameters from 170 mm to 209mm. The specific impeller used for this work had a diameter of 209mm and therefore the upper most curve was used as the reference performance data for the impeller.

The pump head rise varies from 6.2m to 13.8m, giving it a range of 7.6m. The flow rate varies from zero flow to a maximum of 280 m<sup>3</sup>/h or 78l/s. The BEP of the impeller, with an efficiency of 83%, returns a head of 11.8m at a flow rate of 195 m<sup>3</sup>/h or 54l/s. The predicted performance of the scaled test impeller indicates that a greater head rise would be produced but at a significantly lower flow rate compared to the KSB impeller. For this reason certain sensors, the discharge pressure transducer in particular, have ranges significantly greater than required by the KSB impeller test, to account for the scaled test impeller performance.

There is only one  $NPSH_r$  curve for all sized impellers. This is because only inlet conditions affect  $NPSH_r$  and the inlet configurations of each of these impellers are identical. As the flow rate approaches the maximum flow the  $NPSH_r$  reaches a maximum value of 6.4m. The  $NPSH_r$

is 2.2m for the lowest flow rate recorded. The shape of the  $NPSH_r$  curve for the KSB impeller is consistent with the trend shown in Chapter 2, Figure 2.12.

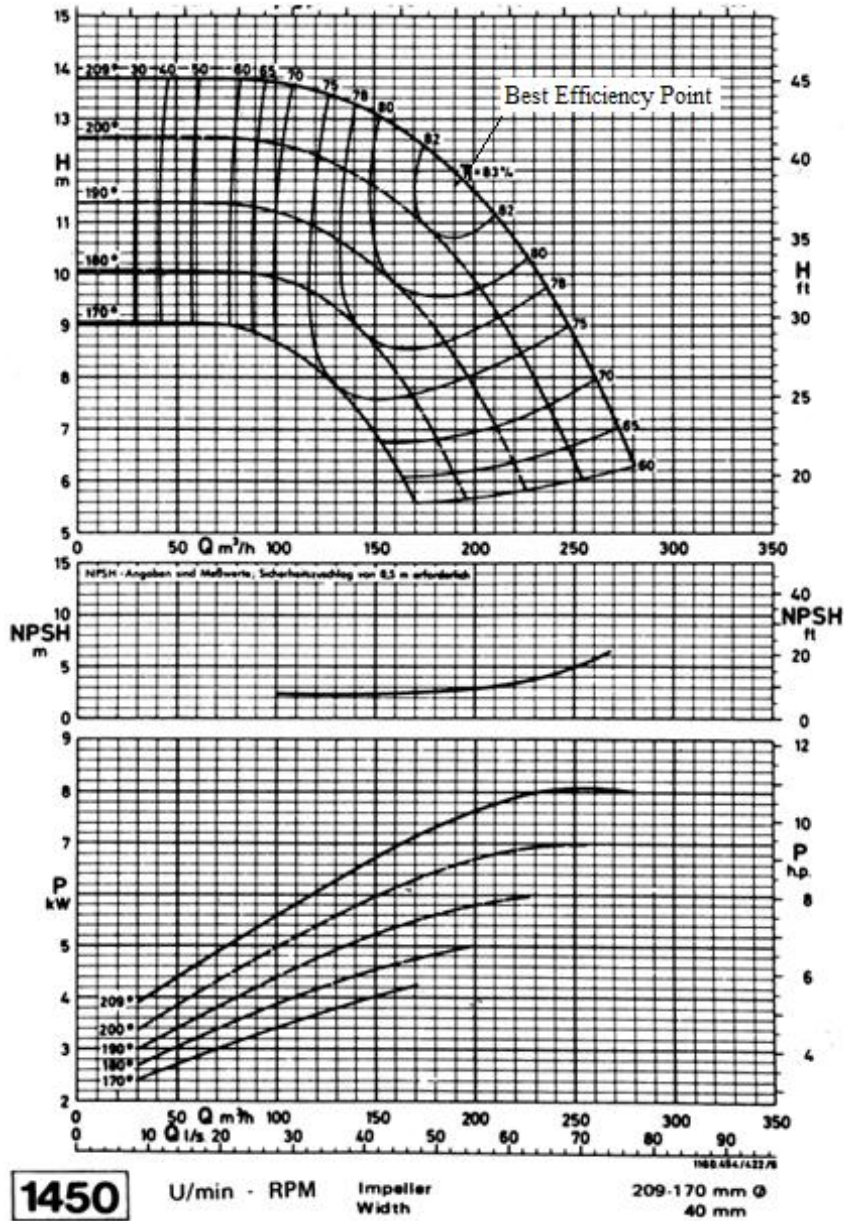


Figure 5.1: KSB ETA 125 - 200 performance data.

The power requirements of the impeller increase with the flow rate to a maximum value, at 128% BEP flow, then begins to reduce as the maximum flow rate is approached. The curve shows a minimum and maximum power requirement of 3.9 kW and 8.1 kW respectively. By projecting the power curve to the shutoff head position the minimum power for the KSB impeller was determined to be approximately 3.2 kW. The power requirements of the KSB pump are relatively low in comparison to the scaled test impeller. However, the rotational speed, 1500 rpm compared to 4000/5000 rpm, is significantly lower, but due to the larger

impeller diameter, higher flow rates are produced. This leads to significantly larger torque requirements that limited the maximum flow at which the KSB pump could be tested.

## **5.2. KSB Pump Test Procedure:**

Testing was divided into two parts; firstly the performance characteristic curve was determined and secondly suction performance was assessed. All tests were conducted at a nominal rotational speed of 1450 rpm to allow for direct comparisons to be made with the supplier data. As torque and power requirements increase with flow rate, any change in the system flow rate would affect the rotational speed of the impeller. It was therefore required that the swashplate angle of the Uchida be adjusted when system flow was varied in order to maintain a constant rotational speed of the impeller. It was found when testing that a maximum flow rate of 10 l/s was achievable without exceeding the torque limit imposed by the maximum allowable Uchida pressure of 340 bar. This relates to a flow rate testing range that extends up to 18.5% of the BEP flow of 54 l/s. Although this represents only a small portion of the entire operational range of the KSB pump, it is adequate to verify the testing techniques proposed and to assess the performance and accuracy of the test rig.

To determine the performance characteristic curve of the impeller, it was required that the head rise across the pump be evaluated for various flow rates. Typically eight to twelve points are required to develop the performance characteristic curve. For this work twelve points were measured in order to confirm the accuracy and repeatability of the results obtained on the test rig. Flow rate was incrementally increased, via the discharge line valves, from zero flow, at shutoff head, to the maximum allowable flow of 10 l/s. Each time, inlet pressure, discharge pressure and flow rate were measured and logged.

Suction performance testing aimed to investigate the effects of cavitation on three pump parameters, namely; the head rise, vibration levels and emitted noise. Tests were conducted at seven different flow rates, from 2 l/s to 8 l/s. At constant flow rate,  $NPSH_a$  was incrementally decreased until a significant reduction in developed head, below 3% of the non-cavitating head, was detected.  $NPSH_a$  was varied using the suction line valve. Throughout each test, mass flow rate was kept constant, despite suction line throttling, by controlling the system head through the discharge line valves. Adjustments were made based on the readings from the flow meter and inlet pressure transducers. For each flow rate tested, twenty data points were measured, for the range of  $NPSH_a$  covered. At each point, inlet pressure and temperature, discharge pressure and vibration levels were measured and logged. Sound levels were then recorded after the other

instrumentation data was logged as this process was controlled by a different loop in the DAQ program.

To maintain accuracy of the results, whenever parameters of the test rig were changed, the system was allowed to settle before measurements were taken. This ensured that any transient effects, created by the change in system conditions, would not influence the test results. The DAQ system sampled all sensors, other than the microphone, at a rate of 100 Hz. At each measurement point data was logged for 10 seconds and then averaged. Audio data was sampled for 2 seconds at a rate of 40 kHz. Sampling theory states that the sampling rate must be at least twice the frequency of the highest frequency signal of interest to avoid aliasing. Therefore a maximum frequency of 20 kHz, the limit of the audible spectrum, could be sampled with the selected sampling rate. The recorded time of 2 s equates to approximately 48 revolutions of the impeller, which is sufficient to allow for a well-developed cavitation noise spectrum to be recorded.

### **5.3. Experimental Results:**

#### **5.3.1: Performance characteristic curve:**

As static pressure was measured across the pump it was necessary to account for differences in dynamic pressure, owing to changes in diameter between the inlet and discharge. Differences in the height of the sensors were taken into account, although the effects were relatively insignificant. Figure 5.2 shows the performance characteristic curve from zero flow, to a maximum of 35m<sup>3</sup>/h. The blue stars in the figure represent the measured curve, while the red line represents the supplier data for the impeller. For the range considered, the supplier data indicates a consistent head of 13.8 m. The measured values for head rise range from 13.8 m to 13.95 m. Therefore all measured data for the KSB impeller performance curve was within 1% of the supplier data. This shows consistency and accuracy of the experimental procedure and test rig.

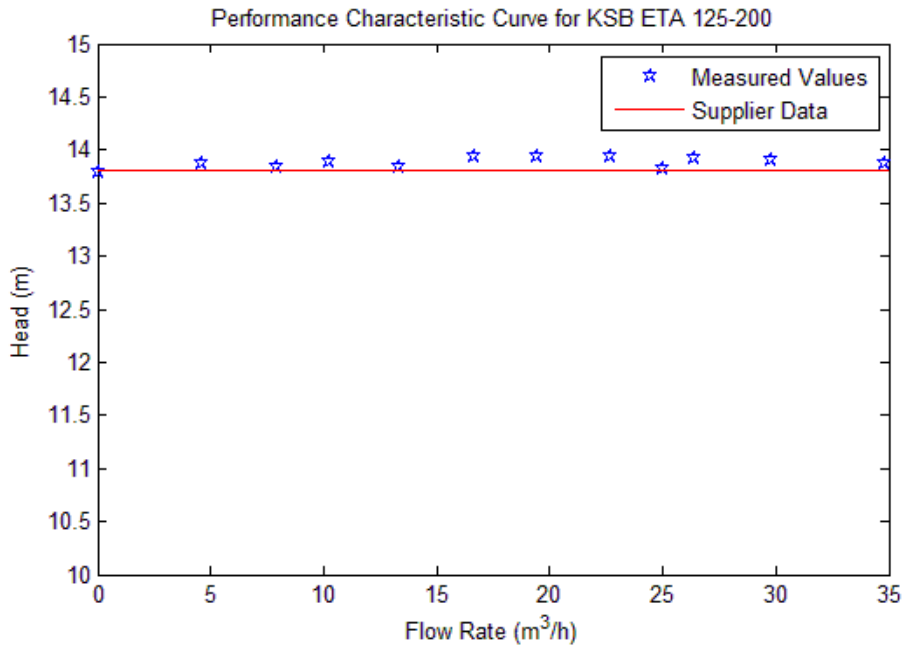


Figure 5.2: Measured pump characteristic curve.

#### 5.4.2. Effect of cavitation on head rise and determining $NPSH_{3\%}$ :

Figure 5.3 shows the measured TDH of the KSB pump, for a range of flow rates, versus the inlet pressure. As mentioned previously, the inlet pressure was reduced by closing down the valve in the suction line. It can be seen that in all cases, at high inlet pressures the head rise corresponds to the measured head rise of 13.8 m, determined for the pump performance characteristic curve above. After significant reduction in inlet pressure, a rapid decline in head rise is noted. This is a result of large cavitation development in the impeller, causing a reduction in the performance of the pump. For flow rates of 6 l/s and below, the head rise appears to gradually reduce, with decreasing inlet pressure, then recovers slightly before finally declining rapidly. This trend is not present for flow rates of 7 l/s and 8 l/s, where the head rise curve remains relatively flat until the final rapid decline. This points to the presence of rotating cavitation, or other flow phenomenon such as auto-oscillation (Brennen, 1994), at lower flow rates causing the gradual decline in head observed, before the effect of large scale cavitation is present.

To determine the  $NPSH_{3\%}$  curve for the KSB impeller, it is required that the value of NPSH at which the developed head is reduced by 3% be found. Figure 5.4 shows the developed head, as a trend line of the data found in Figure 5.3, versus the  $NPSH_a$  at the inlet to the pump. With a non-cavitating head of 13.8 m for all flow rates considered, a value for head rise of 13.386 m

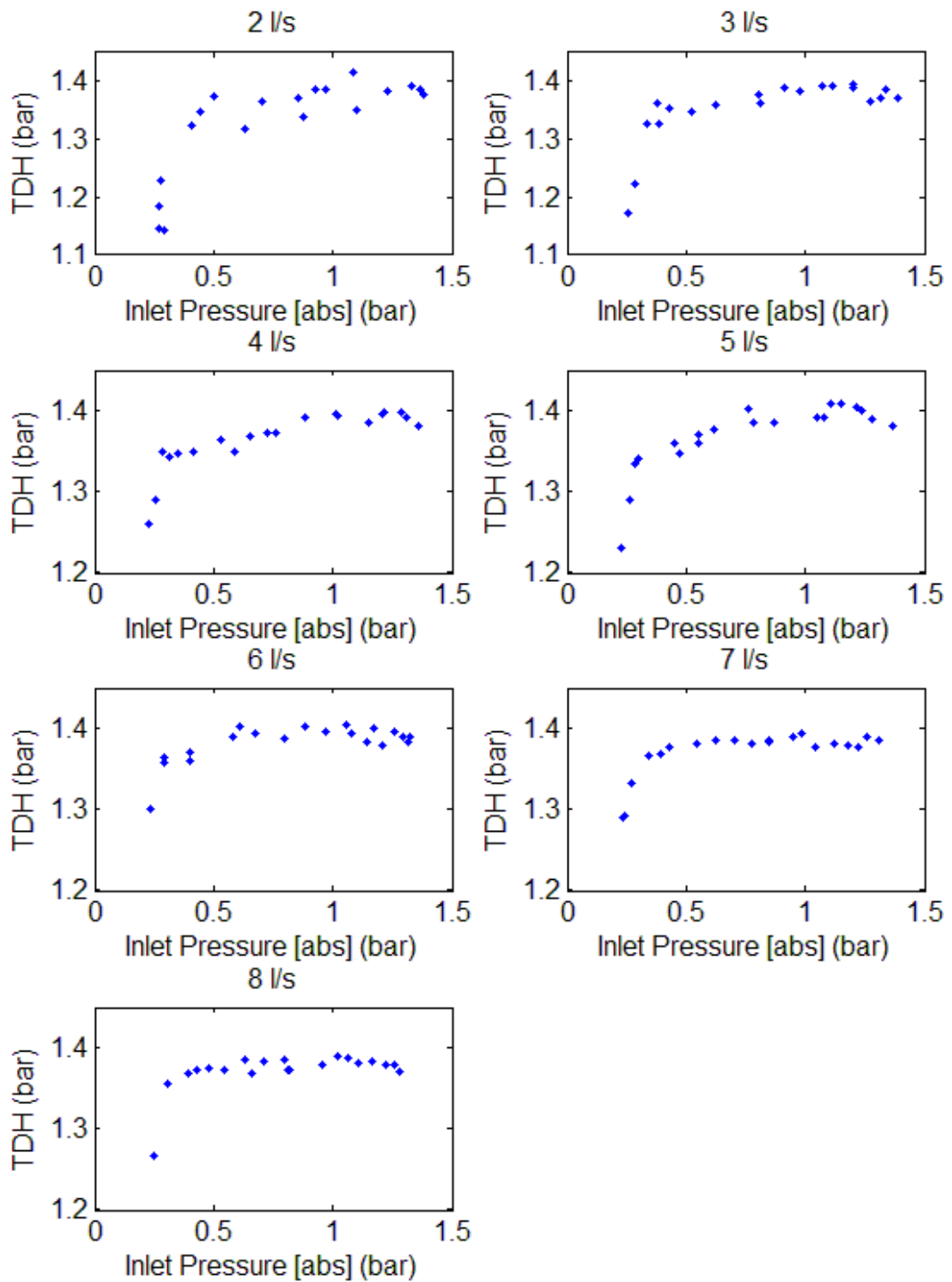


Figure 5.3: Head rise versus inlet pressure for various flow rates.

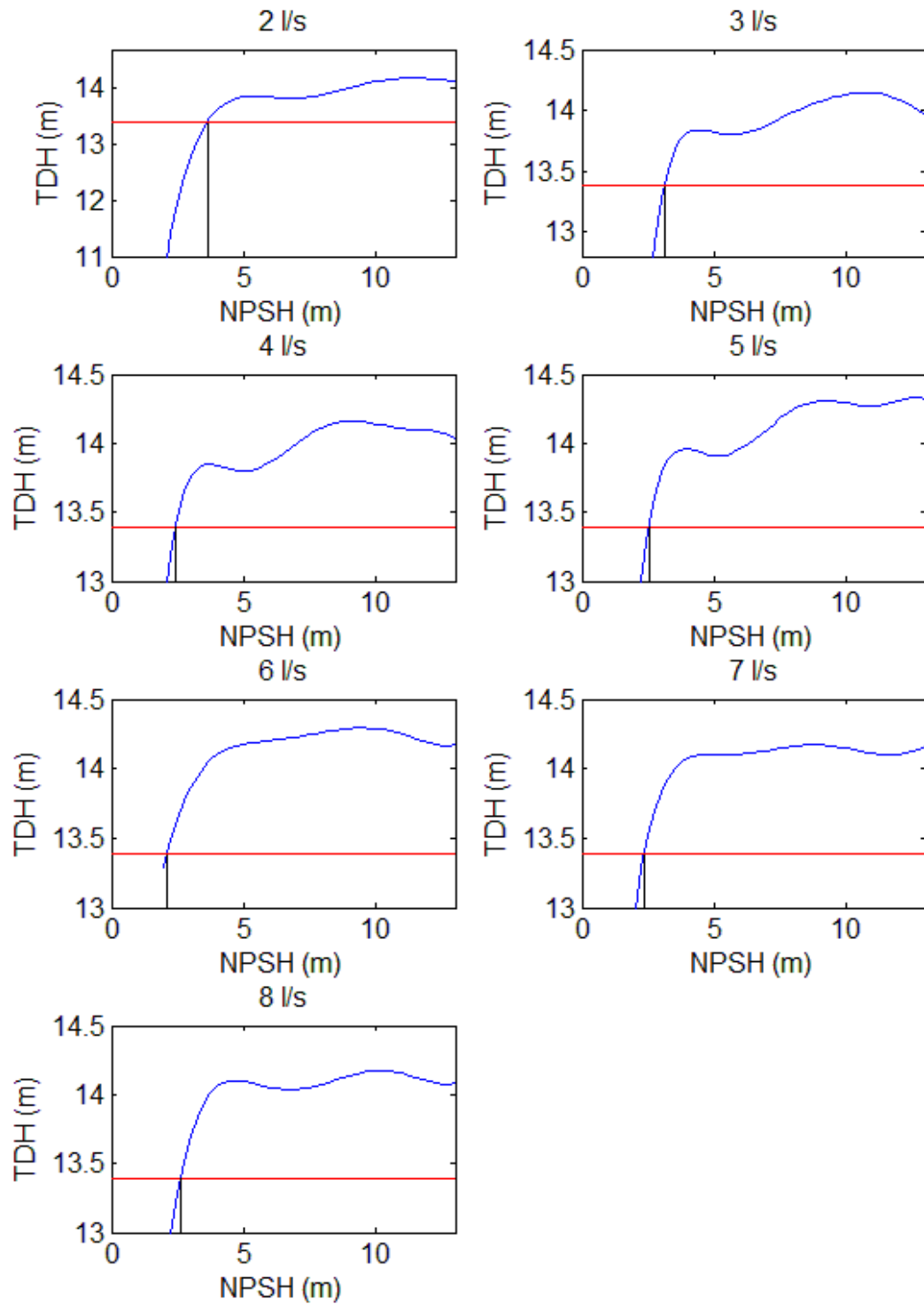


Figure 5.4: Head rise versus NPSH for various flow rates.



represents a 3% reduction. In Figure 5.4, the red horizontal lines represent this value of 3% head drop. The intersection of the head curve and the 3% head drop line then defines the value of  $NPSH_{3\%}$  for the impeller at the particular flow rate. By combining the results for each flow rate, the  $NPSH_{3\%}$  curve can be developed. Figure 5.5 shows the  $NPSH_{3\%}$  curve developed from experimental results, blue stars, and a trend line fitted to the supplier curve data. As no  $NPSH_{3\%}$  supplier data was available for the flow rate range tested, only data for flow rates greater than  $100 \text{ m}^3/\text{h}$  was available, accuracy could not be directly determined. From the supplier data it can be seen that the  $NPSH_{3\%}$  curve rises rapidly as flow rate increases. Below a flow rate of  $150 \text{ m}^3/\text{h}$ , the supplier  $NPSH_{3\%}$  trend line flatten out, giving a value of  $NPSH_{3\%}$  for all lower flow rates, of approximately 2.3 m. The experimental results for the higher flow rates tested, 4 l/s to 8 l/s, the values of  $NPSH_{3\%}$  range between 2.4 and 2.6 m. These values agree somewhat with the supplier data trend line, however they are slightly higher, 13%, then estimated. At the lowest flow rate considered, it can be seen that the  $NPSH_{3\%}$  rises to a maximum of 3.8 m. The trend of the measured data shows that as shutoff head is approached, the  $NPSH_{3\%}$  begins to increases. When the experimental data is compared to the typical  $NPSH_{3\%}$  shown in Chapter 2, Figure 12, it shows the same trend near shutoff head. This rise in  $NPSH_{3\%}$  as shutoff head is approached is a result of the large secondary flows and increased

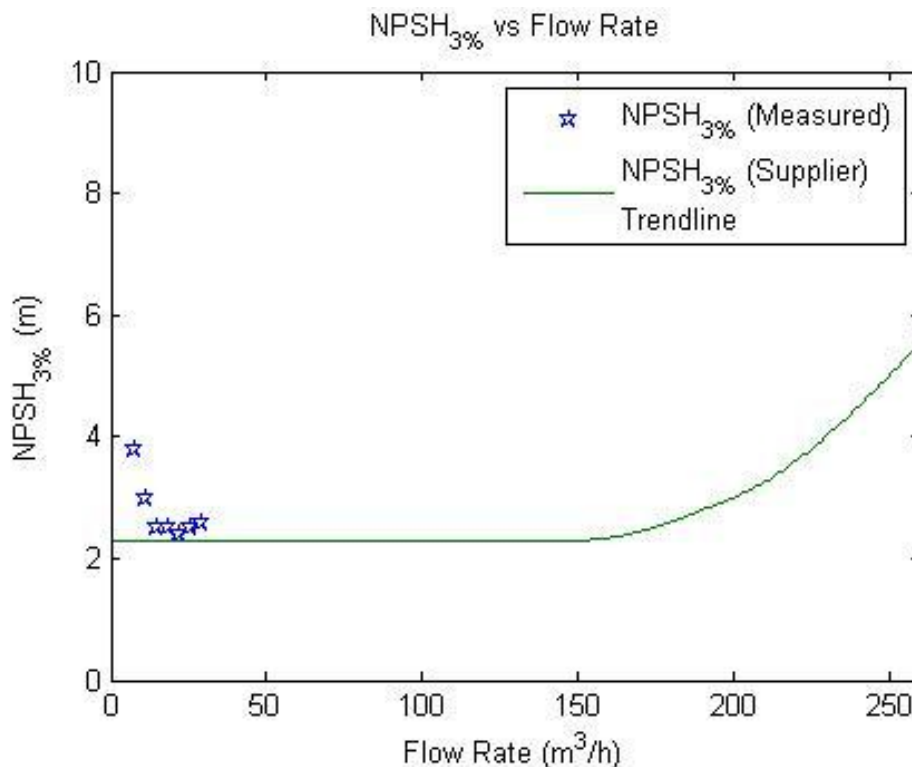


Figure 5.5: Experimental and supplier  $NPSH_{3\%}$  curves.

thermal energy absorbed by the flow at these conditions (Shiels, 1998). This trend for  $NPSH_{3\%}$  to increase as shutoff head is approached may account for higher values of  $NPSH_{3\%}$  measured

in this range. The trend line of supplier data did not consider these low flow effects and would therefore predict a lower value for  $NPSH_{3\%}$  at these flow rates.

#### 5.4.3: Cavitation detection using vibration:

Figure 5.6 presents the RMS vibration velocity of the pump as a function of  $NPSH_a$ , for all flow rates considered. In the figure the red lines represent the non-cavitating vibration levels for the particular flow rates considered. The non-cavitating vibration levels can be seen to rise from 0.8 mm/s to 1.2 mm/s, as flow rate is increased. This is owing to the fact that higher velocity fluid produces greater dynamic forces on the pump structure, leading to higher levels of vibration. From the figure it can be seen that as inlet pressure, hence  $NPSH_a$ , decreases, there comes a point at which the vibration levels begin to rise. This rise in vibration is a result of cavitation development in the pump. The corresponding value for  $NPSH_a$  at which vibration levels begin to rise, can be used as a metric in defining the suction performance of the impeller in a similar way as the previous head drop method. It is important to note that vibration was only assessed at frequencies up to 10 kHz. As a result, only once cavitation had developed significantly enough to produce vibrations in this range, could it be detected. At inception and during early development, cavitating flows produce vibrations at significantly higher frequencies (Koivula et al, 2000), than were able to be measured with the test rig. Therefore the point defined by a rise in vibration level on the test rig does not correspond to the point of cavitation inception, which would occur at a higher value of  $NPSH_a$ . In addition to the insight vibration levels provide with regards to cavitation, they can also be usefully in assessing the potential for vibration induced damage and instability of the physical components, i.e. the pump and the system it serves.

Figure 5.7 shows the  $NPSH_r$  curve based on vibration levels, as well as the  $NPSH_{3\%}$  curve developed previously, based on head reduction (Figure 5.5). Both curves display a similar trend, with higher  $NPSH_r$  near shutoff head, flattening out as the flow rate is increased.  $NPSH_r$  determined through vibration, ranges from a maximum of 8.4 m near shutoff head, to a minimum of 5.3 m. These values are significantly higher than the  $NPSH_{3\%}$  values determined by the head loss method. The reason for the improved detection of cavitation using vibration is a result of the parameters measured in each case. Vibration is a direct result of cavitation and is therefore present as soon as cavitation commences. Head loss is a secondary effect of cavitation, dependent on the specific design of an impeller. For this reason each test can reveal a different aspect of an impeller's suction performance. Vibration test can help to identify the point of cavitation inception and thus how well an impeller design makes use of the  $NPSH_a$ .

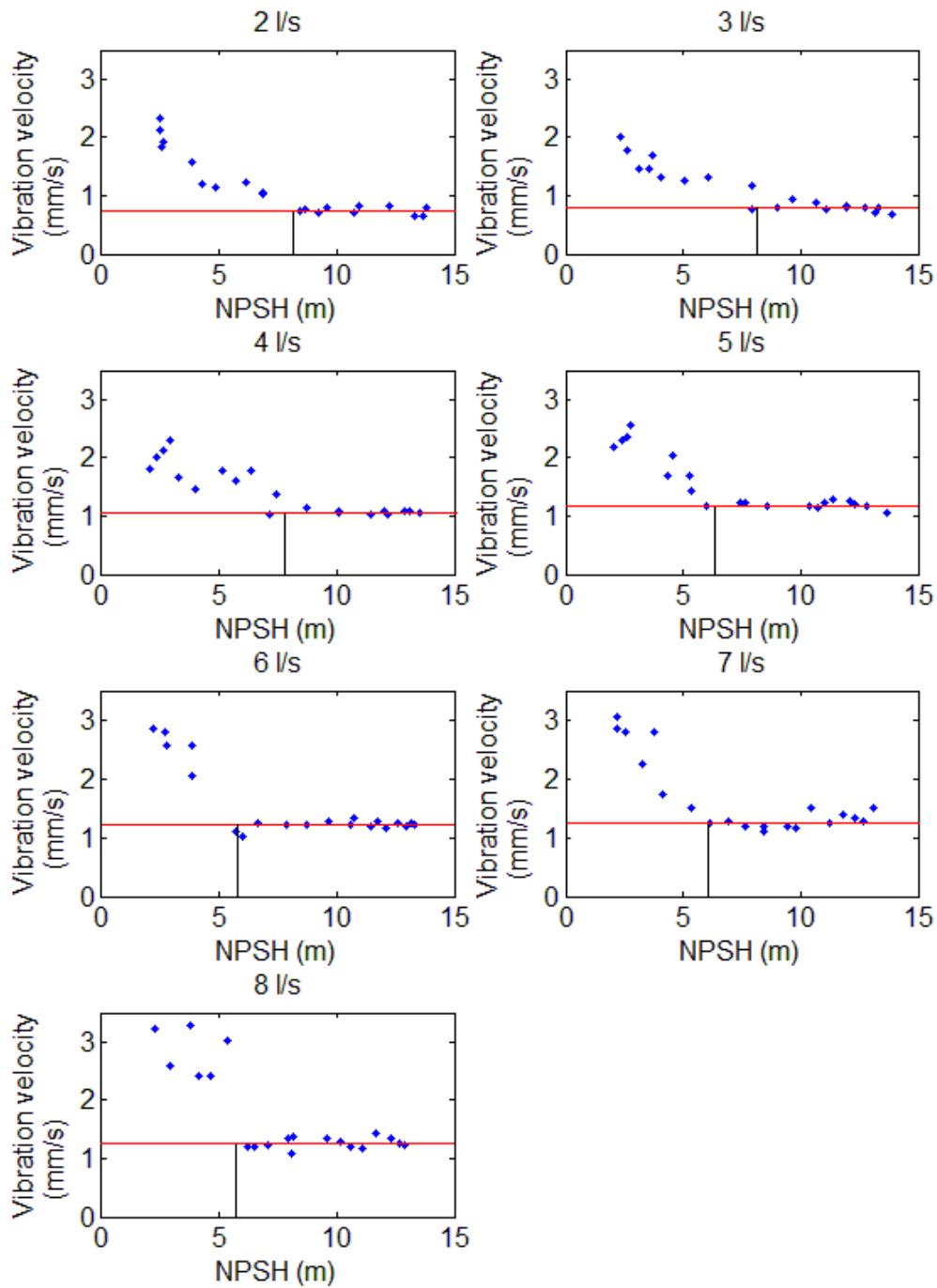


**Figure 5.6: RMS vibration velocity versus NPSH for the seven flow rates tested. Red lines represent the non-cavitating vibration levels. Black lines represent the value of NPSH at which vibration increases due to cavitation.**

The difference between the  $NPSH_a$  for cavitation inception, determined through vibration, and the  $NPSH_{3\%}$  defines a range in which the impeller is known to operate with some cavitation present, but without significant performance loss. A small difference means that an impeller

cannot tolerate any significant amount of cavitation before its performance begins to suffer, while the opposite is true for a large difference. In Figure 5.7 it can be seen that the difference varies with flow rate. Near shutoff head, the difference is 4.6 m, while at the highest flow rate tested it is 2.9 m. This implies that cavitation is present for a greater range of  $NPSH_a$  near shutoff head than at higher flow rates, in the range tested. A large difference may seem advantageous, however it must be noted that cavitation damage and flow instability may occur in this range of operation. In some cases, where these other effects of cavitation are of importance, a small difference, for the same value of  $NPSH_{3\%}$ , would be advantageous, as this would permit operation with lower  $NPSH_a$  before inception.

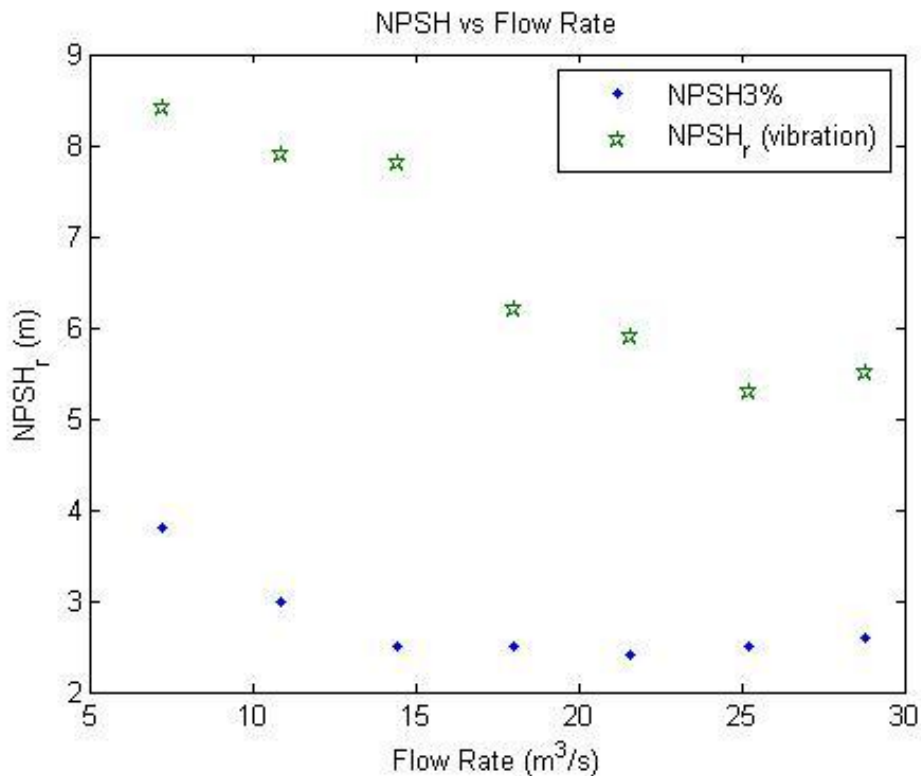


Figure 5.7:  $NPSH_r$  based on vibration and head rise versus flow rate.

#### 5.4.4: Cavitation noise analysis:

The cavitation noise levels were assessed at a single flow rate of 5 l/s. Figure 5.8 shows four time domain noise signal plots. The unfiltered signal as well as low, band and high pass filtered signals are presented. Each graph is an overlay of two signals, recorded at different levels of  $NPSH_a$ . The blue signal was recorded at reduced inlet pressure, with some cavitation present, while the green signal was recorded with no cavitation present. Note that the unfiltered and low pass signals are significantly louder, an order of magnitude, than the band and high pass signals.

This is a result of environmental noise, which is significantly louder than cavitation noise, being present in the first two signals, while the band and high pass signals have filtered it out. The environmental noise is contributed to primarily from the noise emitted from the pump, gearbox and hydraulic motor. When comparing the two unfiltered noise signals at different levels of  $NPSH_a$ , it can be seen that there is little difference between their magnitudes. The same is true for the low pass signal. Due to the dominance of environmental noise in these signals, cavitation noise does not have any significant impact on the signal strength. Therefore the low pass and unfiltered signals can reveal fairly little about the onset and development of cavitation. The band and high pass signals, with environmental noise eliminated, can detect cavitation noise more effectively. In Figure 5.8 the band and high pass signals show a significant increase in noise level, by an order of magnitude, in the presence of cavitation.

In order to investigate the frequency distribution of the noise signals, Fast Fourier Transforms (FFT's) were applied to the time domain signals. Figure 5.9 shows frequency plots for each signal. Each plot shows the difference in the frequency power spectrum between the two cavitation conditions considered in Figure 5.8. By assessing the difference between signals, a large portion of the background noise can be eliminated, allowing for the cavitation noise contribution to be readily identified. The dominance of the environmental noise can once again be seen in the plots of the unfiltered and low pass signals. The only significant frequencies in these plots fall below 1 kHz, in the range of the environmental noise. The plots do not show any bias either, with an almost equal distribution above and below the zero line. This implies no significant difference in the frequency distributions or signal strengths between the two cavitation conditions at low frequencies, where environmental noise is dominant. The band and high pass signal comparisons show significant bias towards the cavitating conditions. In both plots it can be seen that with the introduction of cavitation, there is a broadband increase in noise levels, affecting all frequencies in the band considered. The band and high pass plots show peaks at approximately 3.2 kHz and 13.7 kHz respectively. The band pass peak is larger in relation to the other frequencies in its band, when compared to the high pass peak. This shows a more even distribution of cavitation noise at higher frequencies, while at lower frequencies the cavitation noise appears more strongly at discrete frequencies. Note also the difference in power spectrum strengths between the band and high pass signals. The band pass signal is an order of magnitude larger than the high pass signal. This implies that even though cavitation noise is present over a large range of frequencies, the strength of the signal increase at lower frequencies. The increase in power of the signal at lower frequencies is a result of the greater energy involved with the collapse of a larger cavity.

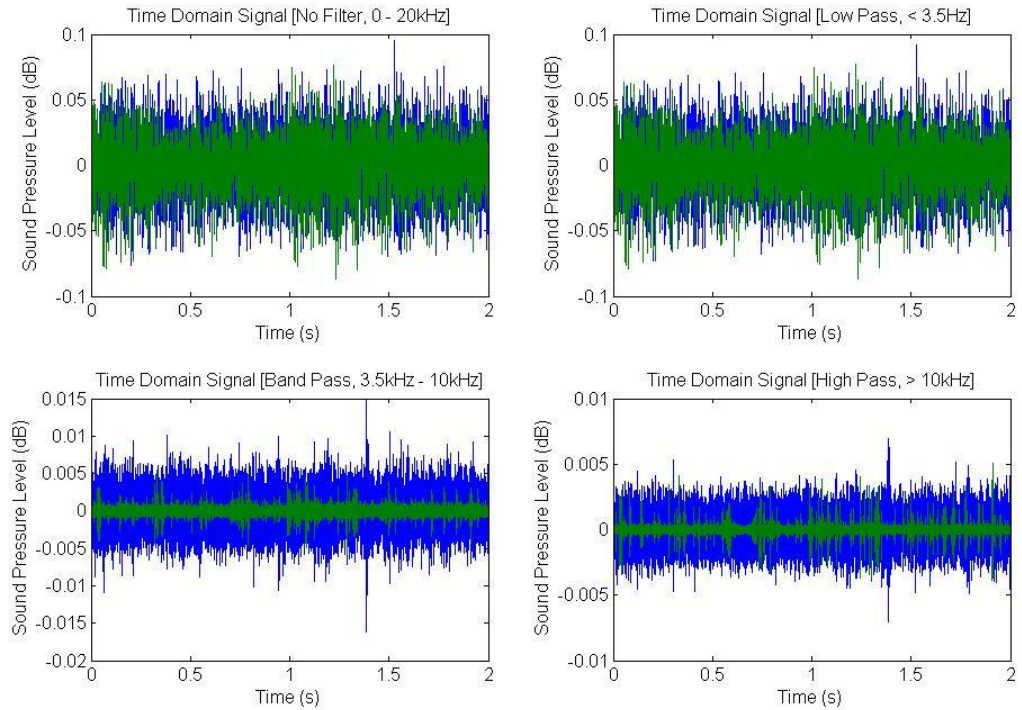


**Figure 5.8: Time domain signal comparisons at non-cavitating and cavitating conditions. The unfiltered signal is shown first followed by low, band and high pass filtered signals.**

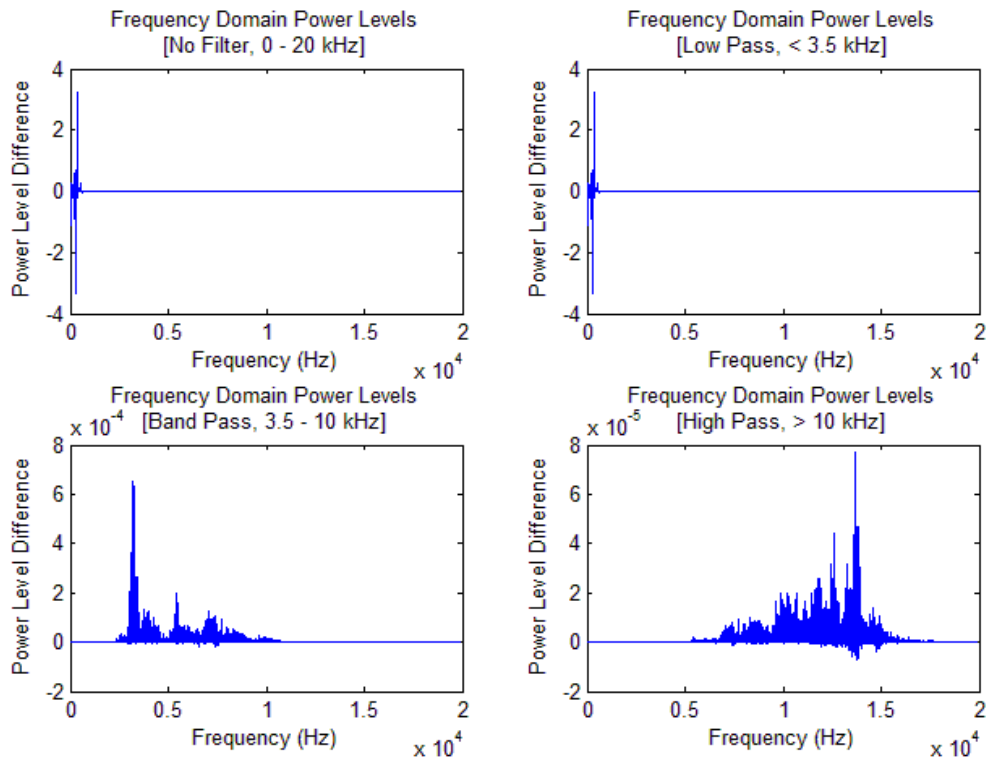


**Figure 5.9: Difference in the frequency power spectrum at two different cavitation conditions. The unfiltered signal is shown first followed by low, band and high pass filtered signals.**

The RMS value of each signal was calculated at varying levels of  $NPSH_a$ . Figure 5.9 shows the RMS signals, in blue, as a function of  $NPSH_a$ , along with the head rise curve, in green. The unfiltered and low pass signals show a similar trend, as to be expected due to the dominance of environmental noise in both signals. Both signals remain relatively flat above a  $NPSH_a$  of approximately 6.5 m, where after they begin to rise rapidly, similar to the vibration levels at 5 l/s (Figure 5.6). This implies that the dominant low frequency noise does increase with a sufficient amount of cavitation, but is likely a result of vibration induced noise and not a direct measure of cavitation noise. The band and high pass signals, where cavitation noise is dominant, show typical cavitation noise trends. As  $NPSH_a$  is reduced, the size and number of cavitation bubbles, or cavities, in the flow increase and therefore the emitted noise increases. The noise levels peak at an intermediate point in the cavitation development process (point A in Figure 5.9). At this point there is still no significant effect of cavitation on the head of the pump. The noise levels then rapidly decline as a result of the damping effects cause by the increasing volume of vapour in the flow (Schiavello and Visser, 2009). Note that the head curve begins to gradually decline as the noise levels do. This head decline is a possible result of rotating cavitation, where a cell of cavitation rotates at 1.1 - 1.2 times the shaft speed (Brennen 1994) in the impeller, which may contribute to the damping of the cavitation noise as well. A further decrease in  $NPSH_a$  brings no change in the RMS noise levels and eventually, at a  $NPSH_a$  of 2.5 m, head breakdown occurs. The rising slope of the high pass signal, at the maximum  $NPSH_a$  tested (point B in Figure 5.9), indicates that cavitation inception occurred at a  $NPSH_a$  above 13.5 m. The high pass signal can be seen to increase more rapidly than the band pass

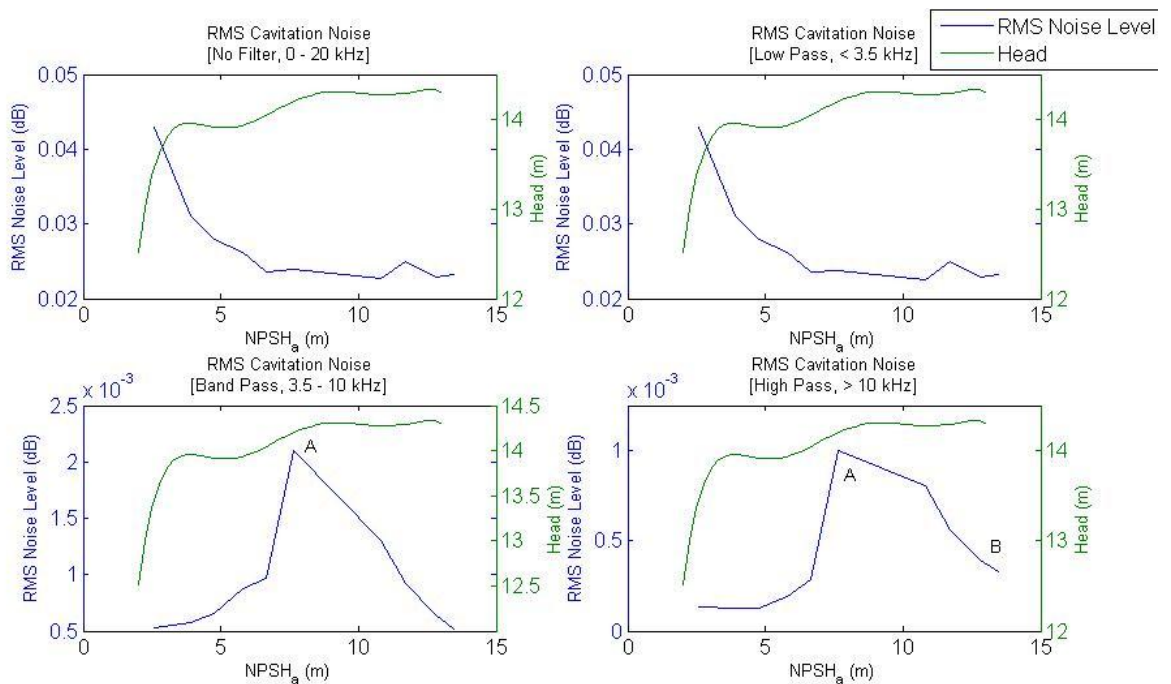


**Figure 5.10: RMS noise levels and head as functions of  $NPSH$ , for a flow rate of 5 l/s.**

signal, with decreasing  $NPSH_a$ . This illustrates the progression of cavitation noise, from high to low frequencies, as it develops. Note that the high pass signal level does not decrease, but continues to increase, as the band pass signal level rises. This indicates that many different sized cavities can coexist in a flow, all contributing different frequencies to the emitted noise spectrum, highlighting the chaotic and broadband nature of cavitation.



## CHAPTER 6

### Conclusion and Future Work

This chapter provides concluding remarks with regards to the work done. Outcomes of the selection and design process of the test impeller are discussed. Outlines of the test rig design process are presented along with identification of the limiting factors and operational envelope. The results and success of the performance validation testing is then evaluated. Finally, the future work required to allow for testing of the scaled impeller is presented.

#### 6.1. Conclusion:

Research began at UKZN into the development of a liquid rocket engine in response to a growing need, locally, for the development of a commercial launch vehicle. The research focused initially on the design of a fuel turbopump impeller to function in a liquid rocket engine. Hypothetical mission parameters were selected based on the perceived requirements of the local satellite industry. From these parameters and comparisons with existing launch vehicles, the parameters of the hypothetical launch vehicle, in which the fuel impeller would operate, could be defined. Moreover from the launch vehicle specifications it was also possible to extract the performance requirements of the fuel turbopump impeller.

Design of the impeller was done using 1D mean-line and quasi 3D multi stream tube analyses, implemented in software packages PUMPAL and AxCent. Initially, inlet and discharge arrangements were assessed using PUMPAL. Once a satisfactory solution was obtained at the inlet and discharge, the through-blade characteristics were assessed in AxCent. The final design had inlet and discharge diameters of 108.6 mm and 186.7 mm respectively, running at 14500 rpm. PUMPAL calculated the design point of the impeller to have a head rise of 889 m at a flow rate of  $0.126 \text{ m}^3/\text{s}$ , requiring 1127.8 kW of power. At this point a  $\text{NPSH}_r$  of 43.51 m was calculated.

To facilitate laboratory testing, a scaled test impeller was used. The primary motivation for this was to reduce the power requirements and  $\text{NPSH}_r$  of the impeller in order to create more realistic requirements for the test rig design. The effects of rotational speed and diameter, on all aspects of the impeller performance, were investigated using the scaling laws. Based on this scaling investigation and the initial limitations on the test rig design, particularly with regards to

power and  $NPSH_a$ , the final design of the scaled test impeller was selected. The scaled test impeller was designed to operate at 5000 rpm, with a reduction of 20% in geometric size. This reduced the power required to 15 kW and the  $NPSH_r$  to 3.5 m. The design point of the scaled test impeller would then have a head rise of 67.7 m, at a flow rate of 0.022 m<sup>3</sup>/s, calculated using PUMPAL.

The requirements established for the test impeller were used as objectives for the design of the test rig. The test rig was a closed loop, system using water as a test fluid. A 65 kW hydraulic pump, motor and gearbox assembly, from an existing turbine blade test rig, was used for the impeller test rig. As this assembly could not be relocated, the design of the test rig had to account for the existing setup and the spacial limitations imposed by its location. A KSB ETA 125 – 200 centrifugal pump was used for its volute, shaft and bearing arrangements. This pump was used for validation testing of the rig and testing procedures and will in the future be modified to house the scaled test impeller. A 2500 l storage tank was used as a reservoir from which water was drawn and returned.  $NPSH_a$  was maximized by placing the storage tank as high above the pump inlet as possible. The effects of suction line length and diameter on  $NPSH_a$  were investigated to determine the most cost effective solution that would still provide adequate  $NPSH_a$ . A throttle valve in the suction line controlled inlet pressure, while two discharge line throttle valves were used for system head control. Instrumentation for measurement of inlet and discharge pressure and temperature, flow rate, rotational speed, vibration and noise levels were installed. With the final design known, a 1D analysis was carried out to determine the operational range of the test rig. Due to the restrictions on available tank height, it was found that there was inadequate  $NPSH_a$  to test the design point of the scaled test impeller at 5000 rpm. The maximum speed, at which the scaled test impeller design point could be tested with adequate  $NPSH_a$ , was calculated to be 4900 rpm. Whilst a maximum speed of 4363 rpm allowed for testing of the entire range of calculated performance with adequate  $NPSH_a$ .

Validation testing was conducted using the KSB pump. Results obtained on the test rig were compared to supplier data to determine accuracy. Validation testing involved determining the performance characteristic curve of the KSB impeller as well as its suction performance. Due to the torque requirements of the KSB impeller, a maximum flow of 18.5% BEP flow was achievable without exceeding the maximum outlet pressure of the Uchida hydraulic supply pump. The performance curve was determined by measuring head rise across the pump for various flow rates. The measured performance characteristic curve was within 1% of the supplier data for the range tested. Suction performance testing investigated three parameters, namely the head rise, vibration and noise levels, to determine the presence and effects of cavitation on the pump. Each suction performance test was conducted at a constant flow rate

which was varied after each test. Data, with regards to the parameters of interest, were measured for decreasing values of  $NPSH_a$ . Head rise data was used to develop the  $NPSH_{3\%}$  curve for the impeller. No supplier data was available for  $NPSH_{3\%}$  in the range tested therefore the trend of the supplier data was used to assess the accuracy of the test results. For the higher flow rates tested, the results obtained on the test rig showed good agreement with the trend of the supplier data, albeit slightly higher than would be expected. Near shutoff head the measured  $NPSH_{3\%}$  curve showed an increasing trend, deviating from the assumed trend of the supplier data. This was owing to the large incidence angles and secondary flows that exist near shutoff head, resulting in increased heat production and thus promoting the development of cavitation. A  $NPSH_r$  curve was established for the KSB impeller, based on the vibration levels of the pump. The values of  $NPSH_a$  at which vibration levels began to increase, due to cavitation, were used to develop the curve. When comparing the vibration curve to the  $NPSH_{3\%}$  curve similar trends were observed, showing consistency between the methods used. The  $NPSH_r$  predicted through vibration was however significantly higher than the  $NPSH_{3\%}$ , revealing the presence of cavitation within the impeller even when no significant performance degradation was detected. The unfiltered noise signal, as well as low, band and high pass filtered noise signals were recorded. Frequency power spectrum plots showed dominant environmental noise in the unfiltered and low pass filtered signals. Frequency power spectrum plots of the band and high pass filtered signals showed a broadband increase in noise levels with the presence of cavitation. RMS noise levels were plotted against  $NPSH_a$  to determine the effect of developing cavitation on the emitted noise. The unfiltered and low pass filtered signals were found to increase at a  $NPSH_a$  similar to that measured by the vibration approach. It was therefore concluded that this rise in noise level was as a result of increased vibration, generating environmental noise, and not cavitation noise directly. The band and high pass filtered signals showed typical cavitation noise trends. Both noise signals initially increased as  $NPSH_a$  was decreased, until a peak was reached, after which a rapid decline was recorded. The rapid decline was a result of vast cavitation in the impeller, creating a damping effect on the cavitation noise. As cavitation first emits high frequency noise, the first indication of its presence was seen in the high pass filtered signal. This signal suggested that cavitation was present in the impeller at a  $NPSH_a$  above 13.5 m for a flow rate of 5 l/s. This value was significantly higher than the values determined through head drop and vibration. For this reason, noise levels provided the best method for the detection of the onset of cavitation, although at this early stage performance of the pump is not compromised.

## 6.2: Future Work:

With the scaled test impeller design, test rig construction and validation testing complete, the next step for this work is to integrate the test impeller into the KSB housing. Figure 6.1 shows a 3D model of the proposed modification to the existing housing. In the figure, the yellow structure is the existing volute of the KSB pump and the black component is the back plate. For the proposed modifications, the inlet section and flange of the housing will be removed to allow for an inlet and shroud, matched to the test impeller geometry, to be installed. The modified shroud is shown in red. The shroud insert could not extend any further radially into the volute as it would have to be installed through the hole in the rear of the casing. The shroud was designed to create a clearance gap of 0.75 mm between itself and the impeller, as specified by the design of the impeller. The shroud was designed with a degree of pinch in the discharge flow passage. This was done to ensure zero diffusion in the flow passage so that pressure and velocity in this section remain constant. This will aid the measurement of exit pressure and velocities of the scaled test impeller. A guiding ring will also be installed, shown in blue, to direct the flow from impeller discharge, to the volute with minimal disruptions. This will help

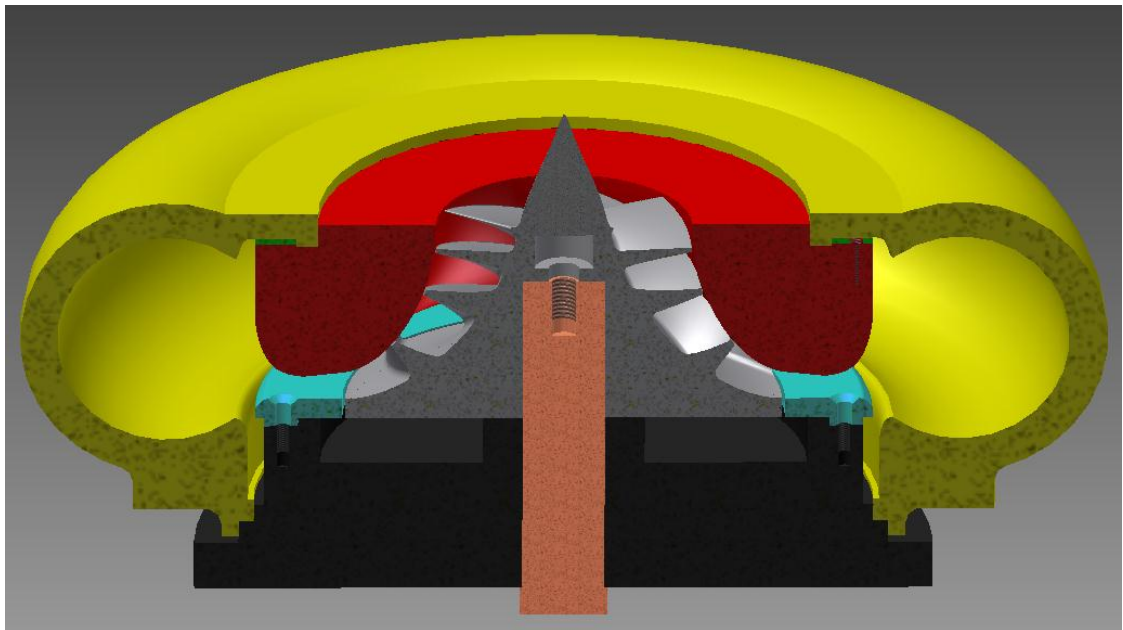


**Figure 6.1: 3D model of proposed modification to the exiting pump housing to accept the scaled test impeller.**

to maintain consistent flow in the discharge flow passage. A gasket, shown in green, will be used to seal the assembly between the original KSB housing and the shroud insert. The impeller will be keyed to the drive shaft and secured at the end with a bolt. The existing shaft will be reduced in length to account for the new impeller. Exact clearances between the impeller and shroud will be achieved using spacers on the pump shaft to varying the axial

position of the impeller. Once such modifications are complete, testing of the impeller will be possible. All tests carried out on the KSB impeller can also be done for the scaled test impeller. As the volute was not designed for the particular test impeller; it will not perform as efficiently as with the KSB impeller. For this reason would be advantageous to measure impeller data before the volute. The inclusion of pitot tubes in the discharge flow passages, between the impeller exit and volute entrance, maybe considered in this regard. This will help to identify exit velocity angles and magnitudes before the volute. Experimental results will then be used to verify the scaled test impeller design and CFD analysis.

## REFERENCES:

- Arndt, R.E.A. (1981). *Cavitation in Fluid Machinery and Hydraulic Structures*. Ann. Rev. Fluid Mech. 13:271-328. St. Anthony Falls Hydraulic Laboratory. University of Minnesota, Minneapolis.
- Baldassarre, A., De Lucia, M., and Nesi, P. (1998). *Real-Time Detection of Cavitation for Hydraulic Turbomachines*. *Real-Time Imaging* 4, 1998, 403-416.
- Boysan, M.E. (2008). *Analysis of Regenerative Cooling in Liquid Propellant Rocket Engine*. Middle East Technical University.
- Braisted, D.M. (1979). *Cavitation induced instabilities associated with turbomachines*. Ph.D. Thesis, California Institute of Technology, Pasadena, Ca.
- Brennen, C.E. (1994). *Hydrodynamics of Pumps*. Concepts ETI Inc. and Oxford University Press.
- Brennen, C.E. (1995). *Cavitation and Bubble Dynamics*. Oxford University Press.
- Campbell, K. (2008). *South African Space Firm Positions Itself as Low-Cost, Small Satellite Hub*. [Homepage of Creamer Media], [Online]. Available: <http://www.engineeringnews.co.za/print-version/sa-space-firm-positions-itself-as-lowcost-small-satellite-hub-2008-09-05> [2011, 15/03].
- Černetič, J., Prezelj, J., and Čudina, M. (2008). *Use of Noise and Vibration Signal for Detection and Monitoring of Cavitation in Kinetic Pumps*. *Acoustics* 08 Paris, 2199-2204.
- Chivers, T.C. (1969). *Cavitation in Centrifugal Pumps*, Proc. Inst. Mech. Eng. 184, Pt. 1, No. 2.
- Colebrook, C. *Turbulent Flow in Pipes, with Particular Reference to the Transition Region between the Smooth and Rough Pipe Laws*. Journal of the Institute of Civil Engineers, London, 11, 1938-39, 133-156.
- Čudina, M. (2002). *Detection of Cavitation Phenomenon in a Centrifugal Pump Using Audible Sound*. *Mechanical Systems and Signal Processing*, 2003, 17(6), 1335-1347.
- Čudina, M., and Prezelj, J. (2008). *Detection of Cavitation in Operation of Kinetic Pumps. Use of Discrete Frequency Tone in Audible Spectra*. *Applied Acoustics* 70, 2009, 540-546.

Ehrlich, D.A., Schwille, J.A., Welle, R.P., Murdock, J.W., and Hardy, B.S. *A Water Test Facility for Liquid Rocket Engine Turbopump Cavitation Testing*. Proceedings of the 7th International Symposium on Cavitation, CAV2009 - Paper No. 11, August 17 - 22, 2009, Ann Arbor, Michigan, USA.

Fraser, W.H. *Flow Recirculation in Centrifugal Pumps*. Texas A. and M. Turbomachinery Symposium, Houston, Texas, December, 1981.

Furst, R.B. (1973). *Liquid Rocket Engine Centrifugal Flow Turbopumps*. SP-8109 NASA.

Gülich, J.F., and Rösch, A., (1988). *Cavitation Erosion in Centrifugal Pumps*. World Pumps, Jult, 164-168.

Haaland, S. *Simple and Explicit Formulas for the Friction Factor in Turbulent Flow*. Transactions of ASME, Journal of Fluids Engineering, 103, 1983, 89-90.

Haidn, O.J. (2008). *Advanced Rocket Engines*. NATO, Neuilly-sur-Seine.

Hofmann, M., Stoffel, B., Friedrichs, J., and Kosyna, G. *Similarities and Geometrical Effects on Rotating Cavitation in Two Scaled Centrifugal Pumps*. Fourth International Symposium on Cavitation, June 20-23-4, Pasadena, California, USA, 2001.

Huzel, D.K., and Huang, D.H. (1992). *Modern Engineering for Design of Liquid-Propellant Rocket Engines*. AIAA, Washington DC, USA.

Isakowitz, S., Hopkins, J., and Hopkins, J. (2004). *International Reference Guide to Space Launch Systems*. AIAA, Fourth Edition, Reston, Virginia.

Japikse, D. (2001). *Overview of Industrial and Rocket Turbopump Inducer Design*. CAV 2001: Fourth International Symposium on Cavitation.

Japikse, D., Marscher, D., and Furst, R. (1997). *Centrifugal Pump Design and Performance*. White River Junction, VT: Concepts NREC.

Johnsson, C.A. (1969). *Cavitation Inception on Headforms, Further Tests*. Proc. 12<sup>th</sup> Int. Towing Tank Conf., Rome, 381-392.

Kamijo, K., Shimura, T., and Watanabe, M. (1977). *An Experimental Investigation of Cavitation Inducer Instability*. ASME Paper 77-WA/FW-14.

Kermeen, R.W. (1956). *Water Tunnel Tests of NACA 4412 and Walchner Profile 7 Hydrofoils in Noncavitating and Cavitating Flows*. Calif. Inst. of Tech. Hydrodynamics Laboratory. Rep 47-5.

- Koivula, T., Ellman, A., and Vilenius, M. (2000). *Experiences on Cavitation Detection Methods*. Institute of Hydraulics and Automation, Tampere University of Technology.
- Kudela, H. *Hydraulic Losses in Pipes*. Published by Khandagale. V., 18 July, 2012.
- Lindgren, H., and Johnsson, C.A. (1966). *Cavitation Inception on Headforms, ITTC Comparative Experiments*. Proc. 11<sup>th</sup> Int. Towing Tank Conf., Tokyo, 219-232.
- Makay, E. (1980). *Centrifugal Pump Hydraulic Instabilities*. Electric Power Res. Inst. Rep. EPRI CS-1445.
- Mårtensson, H., Andersson, S., Trollheden, S., and Brodin, S. (2008). *Rocket Engines: Turbomachinery*. NATO, Neuilly-sur-Seine, France.
- McNulty, P.J., and Pearsall, I.S. (1979). *Cavitation Inception in Pumps*. ASME Int. Symp. On Cavitation Inception, 163-170.
- Moody, L. *Friction Factors for Pipe Flow*. Transactions of the ASME, 66, 8, November 1944, 671-684.
- Parsely, R. and Zhang, B. (2004). *Thermodynamic Power Cycles for Pump-Fed Liquid Propellant Rocket Engines*. Progress in Astronautics and Aeronautics, Volume 200.
- Patel, V.P., and Bro, J.R. *Centrifugal Pumps Inspection and Testing*. Proceedings of the Twelfth International Pump Users Symposium. 143-150.
- Rapposelli, E., Cervone, A., and d'Agostino, L. *A New Cavitating Pump Rotordynamic Test Facility*. 38th AIAA/ASME/SAE/ASEE Joint Propulsion Conference and Exhibit, 7-10 July, 2002, Indianapolis, Indiana.
- Sabersky, R.H., Acosta, A.J., and Hauptmann, E.G. (1989). *Fluid Flow (3<sup>rd</sup> Edition)*, Chapters 12 and 13. MacMillan Publ. Co.
- Schiavello, B., and Visser, F.C. *Pump Cavitation - Various NPSH<sub>r</sub> Criteria, NPSH<sub>a</sub> Margins, and Impeller Life Expectancy*. Proceedings of the Twenty-Fifth International Pump Users Symposium, 2009, 113-144.
- Schilling, J. (2009). *Launch Vehicle Performance Estimation*. Available: <http://silverbirdastronautics.com/LaunchMethodology.pdf> [2011, 03/02].
- Shiels, S. (1998). *Causes of Intermittent and Chronic Cavitation*. World Pumps, May 1998, 57-60.



Sloteman, D.P., Cooper, P., and Graf, E. (1991). *Design of High Energy Pump Impellers to Avoid Cavitation Instabilities and Damage*. Proc.EPRI Power Plant Symp. Tampa, FL, June 1991.

Smyth, J.M. (2014). *The Design and Analysis of a Kerosene Turbopump for a South African Commercial Launch Vehicle*. MSc.Dissertation, University of KwaZulu-Natal, Durban, South Africa.

Sobin, A.J., and Bissel, W.R., (1974). *Turbopump Systems for Liquid Rocket Engines*. SP-8107 NASA.

Sutton, G. (2005). *History of Liquid Propellant Rocket Engines*. AIAA, Reston, Virginia.

Timár, P. (2005). *Dimensionless Characteristics of Centrifugal Pump*. Chem. Pap. 59(6b), 2005, 500-503.

Townsend, G.E. (1962). *Design Guide to Orbital Flight*. Martin-Marietta.

Wood, D., and Weigel, A. (2011). *Charting the Evolution of Satellite Programs in Developing Countries - The Space Technology Ladder*. Space Policy 28, 2012, 15-24.

**APPENDIX A**

**Comparative Data for Hypothetical Launch Vehicle Sizing and Fuel  
Turbopump Requirements**

Table A.1: Comparative Data for 2-Stage Lift Vehicles.

Vehicle	Falcon 1e	Angara 1.1	Kosmos 3M	Delta II (mod)*	Strela
Propellant Combination	LOX/RP-1	LOX/RP-1	UMDH/IRFNA	LOX/RP-1	UMDH/N2O4
Engine Cycle	Gas Generator	Staged	Gas Generator	Gas Generator	Staged
Dry Mass (kg)	2576.4	10000	5310	5680	5700
Propellant Mass (kg)	39462.5	132600	81900	95808	89500
Vac. Thrust (kN)	615.6	2084	1728	1085.8	2070
Vac. Isp (s)	304	337.5	291.3	301.7	310
Chamber Pressure (b)	66.12	257	75	48.4	205
Delta V (m/s)	5372.998	7111.340	4041.1159	6098.54	4810.286
Propellant Combination	LOX/RP-1	LOX/RP-1	UMDH/IRFNA	Aerozine/N2O4	UMDH/N2O4
Engine Cycle	Pressure Fed	Staged		Pressure Fed	Staged
Dry Mass (kg)	544.3	1100	1435	950	2250
Propellant Mass (kg)	4036.97	5200	18700	6004	14000
Vac. Thrust (kN)	30.69	20	163.9	43.7	240
Vac. Isp (s)	317	325.5	303	319.2	320
Chamber Pressure (b)			98.1	57	75
Delta V (m/s)	4918.668	4618.682	7033.022	5124.885	5669.990
Fairing Mass (kg)	136	710	348	841	700
Fairing Jettison Time (s)	185	250	146.5	300	150
Liftoff Mass (kg)**	47256.17	150110	108193	109783	112650
R1	6.063	8.573	4.115	7.856	4.866
R2	4.866	4.250	10.664	5.141	6.091
Total Delta V (m/s)	10291.666	11730.023	11074.138	11223.425	10480.276
Payload - Schilling(kg)***	412	1127	993	773	817
Payload - User Guide (kg)	625		900		900

\* The Delta II vehicle considered does not use strap on boosters.

\*\*The lift-off mass includes a 500 kg payload.

\*\*\*All calculations are made from a local launch site.

Data sourced from Isakowitz et al, 2004.

Table A.2: Comparative Data for Kerosene Engines (Smyth, 2014).

Vehicle	Engine	Cycle	Pc [b]	Tb [s]	Thrust (vac) [kN]	Isp (vac) [s]	Mass Flow Rate [kg/s]	Stage Mass Fraction, $M_f$
Delta II	RS-27A	GG	48.4	261	1085.8	301.7	366.99	0.94
Soyuz	RD-108A	GG	51	290	997.2	319	318.76	0.93
Soyuz	RD-107A	GG	58.5	118	1021.3	319	326.46	0.91
Soyuz	RD-0110	GG	68.2	240	297.9	325	93.47	0.91
Molniya	Block L*	GG	54.5	250	66.7	340	20.00	0.83
Falcon	Merlin 1c	GG	66.12	196	615.6	304	206.49	0.94
Falcon	Merlin Vac*	GG		354	445	310	146.38	
Saturn V	F-1	GG	70	161	7740.5	304	2596.41	
Atlas II	MA-5A booster	GG	44.1	163	2065	293.4	717.69	0.93
Atlas II	MA-5A sustainer	GG	50.7	289	380.6	311	124.79	0.93
Atlas V	RD-180	Staged	257	235	4152	338	1252.62	0.93
Zenit	RD-171	Staged	245	134.1	7911.5	337.22	2392.34	0.91
Zenit	RD-120*	Staged	162.8	297.1	992	350	289.02	0.9
Zenit	RD-58Z*	Staged	78	700	84	356.9	23.99	0.86
Proton	BlockDM*	Staged	97	3000	19.62	325.5	6.15	0.86
Angara	RD-191	Staged	257	300	2084	337.5	629.65	0.93
Angara	RD-0124A*	Staged	162	300	294.3	359	83.59	

\*Second or upper stage engines.

**APPENDIX B**

**Specifications of Instrumentation and KSB Pump**

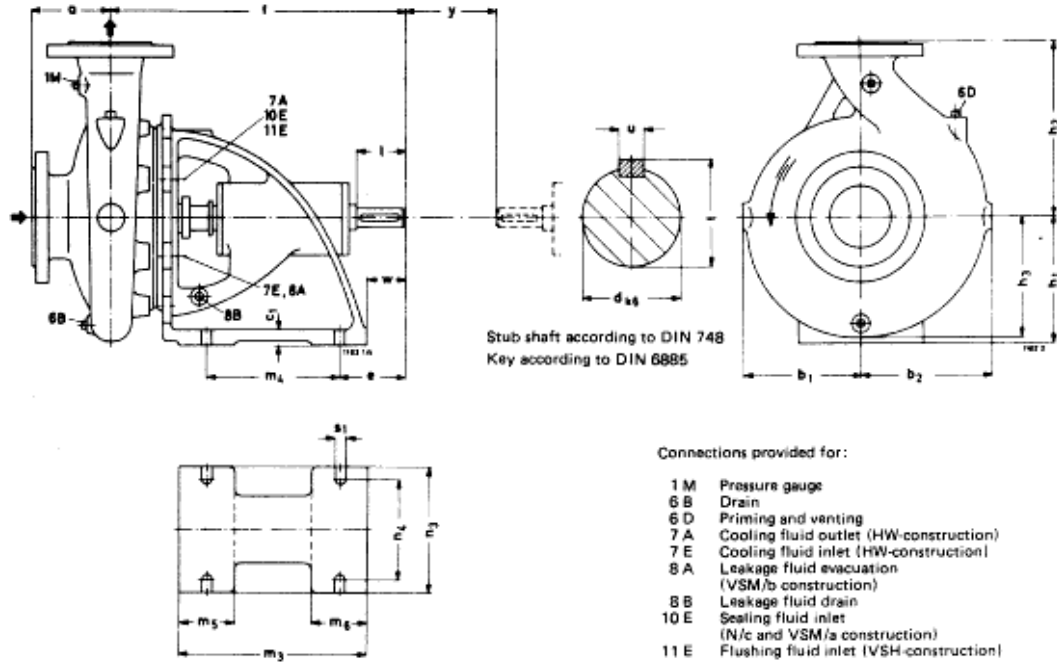
Appendix B-1: KSB pump dimensions.



ETA

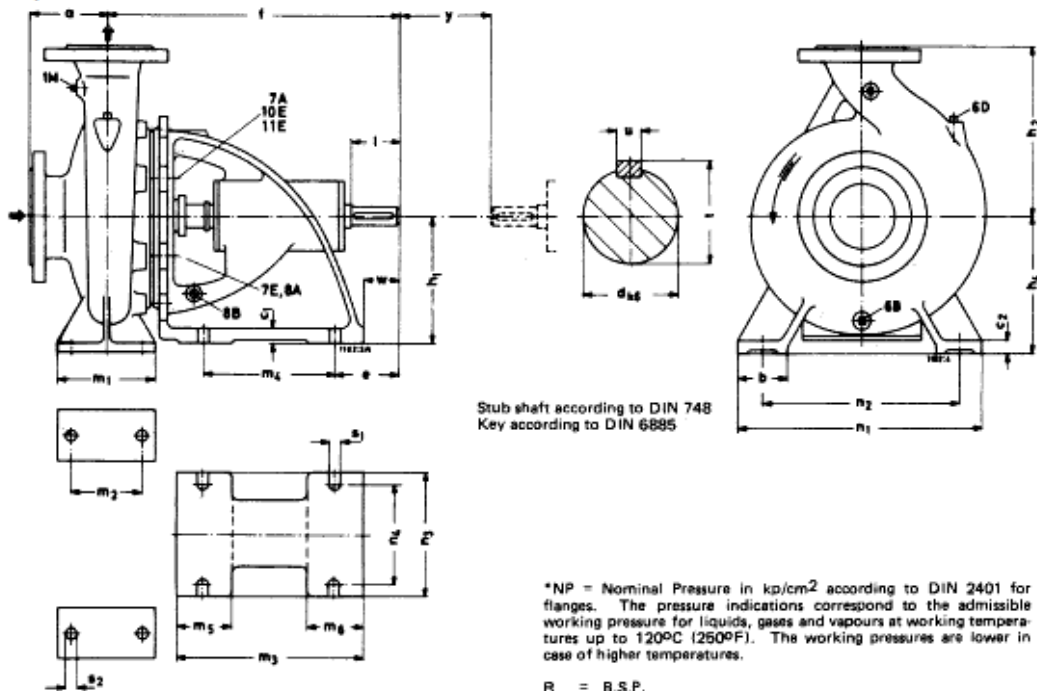
Dimensions

Pumps with bearing pedestal



Dimensions

Pumps with volute feet





Pump Size	Pump dimensions										Foot dimensions														Stub Shaft					
	a	f	b <sub>1</sub>	b <sub>2</sub>	h <sub>1</sub>	h <sub>2</sub>	h <sub>3</sub>	h <sub>4</sub>	y <sup>1)</sup>	b	m <sub>1</sub>	m <sub>2</sub>	m <sub>3</sub>	m <sub>4</sub>	m <sub>5</sub>	m <sub>6</sub>	n <sub>1</sub>	n <sub>2</sub>	n <sub>3</sub>	n <sub>4</sub>	e	w	s <sub>1</sub> for bolts	s <sub>2</sub> for bolts	c <sub>1</sub>	c <sub>2</sub>	Ø d	l	u	t
40-200	100	360	131	145	160	180	134	100				230	160	70	70			160	125	80	45	M 12	16	16	24	50	8	26,9		
40-250	100	360	157	165	160	225	157	100				215	160	55	70			160	125	80	45	M 12	16	16	24	50	8	26,9		
40-315	125	470	182	189	200	250	181	100				275	210	65	90			200	160	110	65	M 16	20	20	32	80	10	35,3		
50-200	100	360	140	162	160	200	148	100				230	160	70	70			160	125	80	45	M 12	16	16	24	50	8	26,9		
50-250	100	360	163	176	160	225	166	100				215	160	55	70			160	125	80	45	M 12	16	16	24	50	8	26,9		
50-315	125	470	191	207	200	280	195	100				275	210	65	90			200	160	110	65	M 16	20	20	32	80	10	35,3		
65-200	100	360	149	172	160	225	158	100				230	160	70	70			160	125	80	45	M 12	16	16	24	50	8	26,9		
65-250	100	470	173	193	200	250	180	100				300	210	90	90			200	160	110	65	M 16	20	20	32	80	10	35,3		
65-315	125	470	198	215	200	280	204	140				275	210	65	90			200	160	110	65	M 16	20	20	32	80	10	35,3		
80-200	125	470	155	188	200	250	168	100				300	210	90	90			200	160	110	65	M 16	20	20	32	80	10	35,3		
80-250	125	470	185	215	200	280	195	100				300	210	90	90			200	160	110	65	M 16	20	20	32	80	10	35,3		
80-315	125	470	204	225	200	315	211	140				275	210	65	90			200	160	110	65	M 16	20	20	32	80	10	35,3		
80-400 <sup>2)</sup>	125	530			250	355		280	140	80	160	120	330	250	80	100	435	355	250	200	110	60	M 16	M 16	22	18	42	110	12	45,1
100-200	125	470	166	207	200	280	185	140				300	210	90	90			200	160	110	65	M 16	20	20	32	80	10	35,3		
100-250	140	470	190	221	200	280	202	140				300	210	90	90			200	160	110	65	M 16	20	20	32	80	10	35,3		
100-315	140	470	212	238	200	315	222	140				275	210	65	90			200	160	110	65	M 16	20	20	32	80	10	35,3		
100-400 <sup>2)</sup>	140	530			250	355		280	140	100	200	150	330	250	80	100	500	400	250	200	110	60	M 16	M 20	22	20	42	110	12	45,1
125-200	140	470	184	229	200	315	203	140				300	210	90	90			200	160	110	65	M 16	20	20	32	80	10	35,3		
125-250	140	470	198	241	200	355	217	140				300	210	90	90			200	160	110	65	M 16	20	20	32	80	10	35,3		
125-315 <sup>2)</sup>	140	530			250	355		280	140	100	200	150	350	250	100	100	500	400	250	200	110	60	M 16	M 20	22	20	42	110	12	45,1
125-400 <sup>2)</sup>	140	530			250	400		315	140	100	200	150	330	250	80	100	500	400	250	200	110	60	M 16	M 20	22	20	42	110	12	45,1
150-200 <sup>2)</sup>	160	470			200	400		280	180	100	200	150	300	210	90	90	550	450	200	160	110	65	M 16	M 20	20	20	32	80	10	35,3
150-250 <sup>2)</sup>	160	470			200	400		280	140	100	200	150	300	210	90	90	500	400	200	160	110	65	M 16	M 20	20	20	32	80	10	35,3
150-315 <sup>2)</sup>	160	530			250	400		280	140	100	200	150	350	250	100	100	550	450	250	200	110	60	M 16	M 20	22	20	42	110	12	45,1
150-400 <sup>2)</sup>	160	530			250	450		315	140	100	200	150	330	250	80	100	550	450	250	200	110	60	M 16	M 20	22	20	42	110	12	45,1

1) Dismantling dimension when using an intermediate sleeve coupling (for dismantling without having to remove the motor)      2) These sizes are designed with pump feet

Dimensions in mm, certified

Pump sizes	Connections							Suction flange (machined acc. to DIN 2533, NP* 16)					Discharge flange (machine acc. to DIN 2533, NP* 16)						
	1M	6B	6D	7A/7E	8B	8A/10E <sup>3)</sup>	10E <sup>4)</sup> 11E	N.B.	Flange Ø	Bolt Circle Ø	Raised face Ø	Bolt No.	Bolt hole Ø	N.B.	Flange Ø	Bolt Circle Ø	Raised face Ø	Bolt No.	Bolt hole Ø
40-200	R3/8"	R1/4"	R3/8"	R1/4"	R1/2"	R1/4"	R3/8"												
40-250	R3/8"	R1/4"	R3/8"	R3/8"	R1/2"	R3/8"	R3/8"	65	185	145	122	4	18	40	150	110	88	4	18
40-315	R3/8"	R1/4"	R3/8"	R3/8"	R3/4"	R3/8"	R3/8"												
50-200	R3/8"	R1/4"	R3/8"	R1/4"	R1/2"	R1/4"	R3/8"												
50-250	R3/8"	R1/4"	R3/8"	R3/8"	R1/2"	R3/8"	R3/8"	65	185	145	122	4	18	50	165	125	102	4	18
50-315	R3/8"	R1/4"	R3/8"	R3/8"	R3/4"	R3/8"	R3/8"												
65-200	R3/8"	R3/8"	R3/8"	R1/4"	R1/2"	R1/4"	R3/8"												
65-250	R3/8"	R3/8"	R3/8"	R3/8"	R3/4"	R3/8"	R3/8"	80	200	160	138	8	18	65	185	145	122	4	18
65-315	R3/8"	R3/8"	R3/8"	R3/8"	R3/4"	R3/8"	R3/8"												
80-200	R3/8"	R3/8"	R3/8"	R1/4"	R3/4"	R1/4"	R3/8"												
80-250	R3/8"	R3/8"	R3/8"	R3/8"	R3/4"	R3/8"	R3/8"	100	220	180	158	8	18	80	200	160	138	8	18
80-315	R3/8"	R3/8"	R3/8"	R3/8"	R3/4"	R3/8"	R3/8"												
80-400 <sup>2)</sup>	R3/8"	R3/8"	R3/8"	R3/8"	R3/4"	R3/8"	R3/8"												
100-200	R1/2"	R1/2"	R1/2"	R1/4"	R3/4"	R1/4"	R3/8"												
100-250	R1/2"	R1/2"	R1/2"	R3/8"	R3/4"	R3/8"	R3/8"	125	250	210	188	8	18	100	220	180	158	8	18
100-315	R1/2"	R1/2"	R1/2"	R3/8"	R3/4"	R3/8"	R3/8"												
100-400 <sup>2)</sup>	R1/2"	R1/2"	R1/2"	R3/8"	R3/4"	R3/8"	R3/8"												
125-200	R1/2"	R1/2"	R1/2"	R1/4"	R3/4"	R1/4"	R3/8"												
125-250	R1/2"	R1/2"	R1/2"	R3/8"	R3/4"	R3/8"	R3/8"	150	285	240	212	8	23	125	250	210	188	8	18
125-315 <sup>2)</sup>	R1/2"	R1/2"	R1/2"	R3/8"	R3/4"	R3/8"	R3/8"												
125-400 <sup>2)</sup>	R1/2"	R1/2"	R1/2"	R3/8"	R3/4"	R3/8"	R3/8"												
150-200 <sup>2)</sup>	R1/2"	R1/2"	R1/2"	R1/4"	R3/4"	R1/4"	R3/8"												
150-250 <sup>2)</sup>	R1/2"	R1/2"	R1/2"	R3/8"	R3/4"	R3/8"	R3/8"	200	340	295	268	12	22	150	285	240	212	8	22
150-315 <sup>2)</sup>	R1/2"	R1/2"	R1/2"	R3/8"	R3/4"	R3/8"	R3/8"												
150-400 <sup>2)</sup>	R1/2"	R1/2"	R1/2"	R3/8"	R3/4"	R3/8"	R3/8"												

3) Stuffing box construction VSM/s      4) Stuffing box construction N/c

**Table B.1: Type 42 flexible gear coupling specifications.**

<b>Type 42 Flexible Gear Coupling</b>		
Max. Bore		42 mm
Min. Bore		11 mm
Max. Torque		80 Nm
Max. Speed		5000 rpm
Max. Misalignment	Angular	3°
	Radial	0.6 mm
	Axial	8 mm

**Table B.2: A-10 pressure transducer specifications**

<b>A-10 Pressure Transducer</b>	
Operating Voltage	8 - 30 VDC
Output Signal	4 - 20 mA
Range	0 - 1/10 bar
Accuracy	± 1 % of span
Non-Repeatability	≤ 0.1 % of span
Non-Linearity	≤ ± 0.5 % of span
Temp Range	0 - 80°C
Temp Error	1 % of span
Signal Noise	≤ ± 0.3 % of span

**Table B.3: S-10 pressure transducer specifications.**

<b>S-10 Pressure Transducer</b>	
Operating Voltage	10 - 30 VDC
Output Signal	4 - 20 mA



Range	-1 - 0 bar
Accuracy	$\pm 0.5$ % of span
Non-Repeatability	$\leq \pm 0.1$ % of span
Non-Linearity	$\leq \pm 0.2$ % of span
Temp Range	0 - 80°C
Temp Error	$\leq 0.2$ % of span

**Table B.4: SAFMAG beta meter electromagnetic flowmeter specifications.**

<b>SAFMAG Beta Meter Electromagnetic Flow Meter</b>	
Operating Voltage	80 - 240 VAC 50/60 Hz
Output Signal	4 - 20 mA
Range	0.1 - 10 m/s
Accuracy	$\pm 0.5$ % of flow rate > 0.5 m/s
Repeatability	$\pm 0.1$ % of flow rate > 0.5 m/s

**Table B.5: PT 100 RTD and transmitter specifications.**

<b>PT 100 RTD and Transmitter</b>	
Operating Voltage	10 - 36 VDC
Output Signal	4 - 20 mA
Range	-50 - 200°C

**Table B.6: Model 2400 vibration sensor specifications.**

<b>Model 2400 Vibration Sensor</b>	
Operating Voltage	10 - 36 VDC
Output Signal	4 - 20 mA

Range (RMS)	0 - 20 mm/s
Frequency Range	10 - 1000 Hz
Accuracy	$\pm 5\%$
Plane of Measurement	90 <sup>0</sup> to surface

**APPENDIX C**

**Preliminary Scaling Calculations**

**Appendix C-1: MATLAB code used to plot the effects of impeller rotational speed and scaling factor on head, flow rate, power and NPSH<sub>r</sub>.**

```

% Plots the relationship between performance parameters, scaling
factor

% and rotational speed.

% Imports scaled test impeller data

[ScaledData] = xlsread...

('C:\Users\208504902\Desktop\Dissertation\Chapter
3\Calculations\MatlabScaling.xlsx');

% Setting up result arrays

Q = zeros(6,10);

H = Q;

P = Q;

NPSH = Q;

N = Q;

SF = Q;

% Entering scaling factor and rotational speeds

sf = 1;

for i = 1 : 6
    n = 11000;
    for j = 1 : 10
        N(i,j) = n;
        SF(i,j) = sf;
        n = n - 1000;
    end
    sf = sf - 0.1;
end

N(1:6,1) = 14500;

% Entering flow rate, head rise and power

for i = 1 : 6
    k = 1;
    for j = 1 : 4 : 37
        Q(i,k) = ScaledData(i,j);
    end
end

```

```

H(i,k) = ScaledData(i,j+1);
P(i,k) = ScaledData(i,j+2);
NPSH(i,k) = ScaledData(i,j+3);
    k = k + 1;

end

end

% 3D plot of flow rate, scaling factor and rotational speed
figure(1)
clf
surf(SF,N,Q)

% 3D plot of head rise, scaling factor and rotational speed
figure(2)
clf
surf(SF,N,H)

% 3D plot of power, scaling factor and rotational speed
figure(3)
clf
surf(SF,N,P)

% 3D plot of NPSH, scaling factor and rotational speed
figure(4)
clf
surf(SF,N,NPSH)

```

**Table C.1: Scaled impeller performance data used to compare the effects of rotational speed and geometric scaling factor.**

	Flow Rate [m <sup>3</sup> /s]	Head [m]	Power [kW]	NPSHr [m]	Flow Rate [m <sup>3</sup> /s]	Head [m]	Power [kW]	NPSHr [m]	Flow Rate [m <sup>3</sup> /s]	Head [m]	Power [kW]	NPSHr [m]
SF	14500 [rpm]				10000 [rpm]				9000 [rpm]			
1.0	0.126	889.000	1130.000	43.500	0.087	422.830	370.659	20.690	0.078	342.492	270.210	16.759
0.9	0.092	648.081	667.254	31.712	0.063	308.243	218.870	15.083	0.057	249.677	159.557	12.217
0.8	0.065	455.168	370.278	22.272	0.044	216.489	121.458	10.593	0.040	175.356	88.543	8.580
0.7	0.043	304.927	189.919	14.921	0.030	145.031	62.297	7.097	0.027	117.475	45.414	5.748
0.6	0.027	192.024	87.869	9.396	0.019	91.331	28.822	4.469	0.017	73.978	21.012	3.620
0.5	0.016	111.125	35.313	5.438	0.011	52.854	11.583	2.586	0.010	42.812	8.444	2.095

<b>SF</b>	<b>8000 [rpm]</b>				<b>7000 [rpm]</b>				<b>6000 [rpm]</b>				
1.0	0.070	270.611	189.777	13.241	0.061	207.187	127.136	10.138	0.052	152.219	80.062	7.448	
0.9	0.051	197.276	112.062	9.653	0.044	151.039	75.073	7.391	0.038	110.967	47.276	5.430	
0.8	0.036	138.553	62.186	6.780	0.031	106.080	41.660	5.191	0.027	77.936	26.235	3.814	
0.7	0.024	92.820	31.896	4.542	0.021	71.065	21.368	3.477	0.018	52.211	13.456	2.555	
0.6	0.015	58.452	14.757	2.860	0.013	44.752	9.886	2.190	0.011	32.879	6.226	1.609	
0.5	0.009	33.826	5.931	1.655	0.008	25.898	3.973	1.267	0.007	19.027	2.502	0.931	
<b>SF</b>	<b>5000 [rpm]</b>				<b>4000 [rpm]</b>				<b>3000 [rpm]</b>				
1.0	0.043	105.707	46.332	5.172	0.035	67.653	23.722	3.310	0.026	38.055	10.008	1.862	
0.9	0.032	77.061	27.359	3.771	0.025	49.319	14.008	2.413	0.019	27.742	5.910	1.357	
0.8	0.022	54.122	15.182	2.648	0.018	34.638	7.773	1.695	0.013	19.484	3.279	0.953	
0.7	0.015	36.258	7.787	1.774	0.012	23.205	3.987	1.135	0.009	13.053	1.682	0.639	
0.6	0.009	22.833	3.603	1.117	0.008	14.613	1.845	0.715	0.006	8.220	0.778	0.402	
0.5	0.005	13.213	1.448	0.647	0.004	8.457	0.741	0.414	0.003	4.757	0.313	0.233	
<b>SF</b>	<b>2000 [rpm]</b>												
1.0	0.017	16.913	2.965	0.828									
0.9	0.013	12.330	1.751	0.603									
0.8	0.009	8.660	0.972	0.424									
0.7	0.006	5.801	0.498	0.284									
0.6	0.004	3.653	0.231	0.179									
0.5	0.002	2.114	0.093	0.103									

Scaled data calculated using the affinity laws based of the PUMPAL performance data for the full scale impeller.

**APPENDIX D**

**1D Test Rig Calculations**

**Appendix D-1: MATLAB code used to determine the effects of suction line length and diameter on NPSH<sub>a</sub>.**

```

% Calculates the effects of pipe length and diameter on NPSHa
% Fluid constants
rho = 1000;
mu = 0.000852;
% System constants
g = 9.81;
Q = 0.022;
e = 0.00003;
Hatm = 101325/(rho*g);
Hvap = 3158/(rho*g);
% Sets up arrays
Hs = 3.8;
NPSHa = zeros(5,26);
length = NPSHa;
D = NPSHa;
% Inputs array values
d = 0.08;
for i = 1 : 5
    len = 0;
    for j = 1 : 26
        length(i,j) = len;
        D(i,j) = d;
        len = len + 1;
    end
    d = d + 0.02;
end
% Calculates NPSHa based on pipe length and diameter
for i = 1 : 5
    A = (pi/4)*(D(i,1)^2);
    Re = Reynolds(rho, mu, Q, D(i,1), A);

```



```

    f = DarcyFrictionFactor(e, D(i,1), Re);
for j = 1 : 26
NPSHa(i,j) = Hs - Hvap - (f*length(1,j))/(2*g*D(i,1))*((Q/A)^2);
end
end

% 3D plot of NPSHa, pipe length and diameter
figure(1)
clf
surf(D,length,NPSHa)
-----

```

**Appendix D-2: MATLAB code used to calculate test rig inlet pressure.**

```

% Calculates test rig inlet pressure
% Fluid constants
rho = 1000;
mu = 0.000852;
% System constants
Patm = 101325;
Ps = 38000;
g = 9.81;
Nv = 4;
Kl = 0.2;
D = 0.108;
e = 0.00003;
L = 14.29;
% Calculates pipe area
A = pi*(D^2)/4;
% Sets up Q to be used in calculations
Q = 0 : 0.0025 : 0.035;
% Sets up inlet pressure results array
P1 = zeros(1,15);
% Calculates inlet pressure

```

```

fori = 1 : 15
    V = Q(i)/A;
    Re = Reynolds(rho, mu, Q(i), D, A);
    f = DarcyFrictionFactor(e, D, Re);
P1(i) = (Ps - rho*(V^2)/2 - (rho*f*L)/(2*D)*(V^2)...
    - (Nv*Kl*rho)*(V^2)/2)/100000;
end
% Plots inlet pressure as a function of flow rate
figure(1)
clf
plot(Q,P1)

```

-----

**Appendix D-3: MATLAB code used to calculate and plot test rig NPSH<sub>a</sub> and scaled test impeller NPSH<sub>r</sub> versus flow rate.**

```

% Calculates and plots NPSHa and NPSHr versus flow rate
% Fluid constants
rho = 1000;
mu = 0.000852;
% System constants
Patm = 101325;
Ps = 38000;
g = 9.81;
Pvap = 3158;
D = 0.108;
e = 0.00003;
L = 14.29;
Nv = 4;
Kl = 0.2;
% Calculates pipe area
A = pi*(D^2)/4;
% Sets up Q used in calculations
Q = 0 : 0.0025 : 0.035;

```

```

% Sets up NPSHa results array
NPSHA = zeros(1,15);

% Imports the NPSHr curves for the scaled test impeller
[NPSHR] = xlsread('C:\Users\208504902\Desktop\Dissertation\Chapter
4\Calculations\NPSHr.xlsx');

% Calculates NPSHa
for i = 1 : 15
    V = Q(i)/A;
    Re = Reynolds(rho, mu, Q(i), D, A);
    f = DarcyFrictionFactor(e, D, Re);
    NPSHA(i) = Ps/(rho*g) - (f*L)/(2*rho*D)*(V^2) - Pvp/(rho*g)...
        - (Nv*Kl)/(2*g)*(V^2);
end

% Plots NPSHa and NPSHr as a function of flow rate
figure(1)
clf
plot(Q,NPSHA,'r',NPSHR(1:7,1),NPSHR(1:7,2),'b',NPSHR(1:7,3),NPSHR(1:7,
4)...
,'b',NPSHR(1:7,5),NPSHR(1:7,6),'b',NPSHR(1:7,7),NPSHR(1:7,8),'b'...
,NPSHR(1:7,9),NPSHR(1:7,10),'b')

```

---

**Appendix D-4: MATLAB code used to calculate test rig system head and operational envelope.**

```

% Calculates the operational envelope of the test rig

% Fluid constants
rho = 1000;
mu = 0.000852;

% System constants
Patm = 101325;
P1s = 38000;
P2s = 38000;
g = 9.81;
D = 0.108;

```

```

e = 0.00003;

L1 = 14.29;

L2 = 9.48;

Nb = 9;

K1 = 0.2;

% Calculates pipe area
A = pi*(D^2)/4;

% Sets up Q for calculations
Q = 0 : 0.0025 : 0.035;

% Sets up system head results array
Hsys = zeros(1,15);

% Sets up max pipe pressure line
PipeMax = zeros(2);
PipeMax(1,1) = 0;
PipeMax(2,1) = 0.035;
PipeMax(1,2) = 100;
PipeMax(2,2) = 100;

% Sets up NPSHr line
NPSHcurve = zeros(4,2);
NPSHcurve(1,1) = 0.007218;
NPSHcurve(2,1) = 0.02055;
NPSHcurve(3,1) = 0.02683;
NPSHcurve(4,1) = 0.03082;
NPSHcurve(1,2) = 150;
NPSHcurve(2,2) = 71.9;
NPSHcurve(3,2) = 24.5;
NPSHcurve(4,2) = -5.3;

% Imports scaled test impeller performance curves and operating points
[Head] = xlsread('C:\Users\208504902\Desktop\Dissertation\Chapter
4\Calculations\HeadCurve.xlsx');

[OP] = xlsread('C:\Users\208504902\Desktop\Dissertation\Chapter
4\Calculations\OperatingPoint.xlsx');

% Calculates system head
for i = 1 : 15

```

```

V = Q(i)/A;

Re = Reynolds(rho, mu, Q(i), D, A);

f = DarcyFrictionFactor(e, D, Re);

Hsys(i) = (P2s - P1s)/(rho*g) + (f*(L1+L2))/(2*g*D)...
* (V^2) + (Nb*Kl)/(2*g)*(V^2);

end

% Plots the operational envelope of the test rig
figure(1)
clf
plot(Q,Hsys, 'r',PipeMax(1:2,1),PipeMax(1:2,2), 'r',OP(1:35,1),OP(1:35,2)
)...
, 'g',NPSHcurve(1:4,1),NPSHcurve(1:4,2), 'r',Head(1:7,1),Head(1:7,2), 'b'
...
,Head(1:7,3),Head(1:7,4), 'b',Head(1:7,5),Head(1:7,6), 'b',Head(1:7,7)...
.
,Head(1:7,8), 'b',Head(1:7,9),Head(1:7,10), 'b',Head(1:7,11),Head(1:7,12)
)...
, 'k',Head(1:7,13),Head(1:7,14), 'k')
axis([0 0.035 0 160])

% Plots the system head curve
figure(2)
clf
plot(Q,Hsys)

```

---

**Appendix D-5: MATLAB function used to calculate flow Reynolds number.**

```

function [Re] = Reynolds(rho, mu, Q, D, A)

% Calculates the Reynolds number of the flow

Re = (rho*Q*D)/(mu*A);

end

```

---

**Appendix D-6: MATLAB function used to calculate the Darcy friction factor.**

```

function [f] = DarcyFrictionFactor(e, D, Re)

```

% Calculates the Darcy friction factor using the Halaand Equation

$$f = 1 / (-1.8 * \log_{10}(((e/D) / 3.7)^{1.11} + (6.9/Re)))^2;$$

end

-----

**Table D.1: Scaled NPSH<sub>r</sub> data for the test impeller used to compare with NPSH<sub>a</sub>.**

6000 [rpm]		5000 [rpm]		4000 [rpm]		3000 [rpm]		2000 [rpm]	
Flow Rate [m <sup>3</sup> /s]	NPSH <sub>r</sub> [m]	Flow Rate [m <sup>3</sup> /s]	NPSH <sub>r</sub> [m]	Flow Rate [m <sup>3</sup> /s]	NPSH <sub>r</sub> [m]	Flow Rate [m <sup>3</sup> /s]	NPSH <sub>r</sub> [m]	Flow Rate [m <sup>3</sup> /s]	NPSH <sub>r</sub> [m]
0.0108	3.672	0.009	2.55	0.0072	1.632	0.0054	0.918	0.0036	0.408
0.01452	3.888	0.0121	2.7	0.00968	1.728	0.00726	0.972	0.00484	0.432
0.01848	4.176	0.0154	2.9	0.01232	1.856	0.00924	1.044	0.00616	0.464
0.0228	4.608	0.019	3.2	0.0152	2.048	0.0114	1.152	0.0076	0.512
0.02664	5.04	0.0222	3.5	0.01776	2.24	0.01332	1.26	0.00888	0.56
0.03048	5.58	0.0254	3.875	0.02032	2.48	0.01524	1.395	0.01016	0.62
0.03468	6.192	0.0289	4.3	0.02312	2.752	0.01734	1.548	0.01156	0.688

**Table D.2: Scaled performance data for test impeller used to plot operational envelope.**

6000 [rpm]		5000 [rpm]		4000 [rpm]		3000 [rpm]		2000 [rpm]	
Flow Rate [m <sup>3</sup> /s]	Head [m]	Flow Rate [m <sup>3</sup> /s]	Head [m]	Flow Rate [m <sup>3</sup> /s]	Head [m]	Flow Rate [m <sup>3</sup> /s]	Head [m]	Flow Rate [m <sup>3</sup> /s]	Head [m]
0.0108	141.1	0.0090	98.00	0.0072	62.72	0.0054	35.28	0.0036	15.68
0.0145	131.7	0.0121	91.50	0.0097	58.56	0.0073	32.94	0.0048	14.64
0.0185	120.9	0.0154	84.00	0.0123	53.76	0.0092	30.24	0.0062	13.44
0.0228	109.4	0.0190	76.00	0.0152	48.64	0.0114	27.36	0.0076	12.16
0.0266	97.20	0.0222	67.50	0.0178	43.20	0.0133	24.30	0.0089	10.80
0.0305	85.68	0.0254	59.50	0.0203	38.08	0.0152	21.42	0.0102	9.520
0.0347	73.44	0.0289	51.00	0.0231	32.64	0.0173	18.36	0.0116	8.160
4900 [rpm]		4363 [rpm]							
Flow Rate [m <sup>3</sup> /s]	Head [m]	Flow Rate [m <sup>3</sup> /s]	Head [m]						
0.0088	93.35	0.0078	73.42						
0.0118	87.16	0.0105	68.55						
0.0150	80.01	0.0133	62.93						
0.0185	72.39	0.0164	56.94						
0.0217	64.29	0.0192	50.57						
0.0248	56.67	0.0220	44.58						
0.0282	48.58	0.0250	38.21						

**Table D.3: Scaled design operating point used to plot operational envelope.**

<b>Flow Rate</b> [m <sup>3</sup> /s]	0	0.005	0.01	0.015	0.02	0.025	0.03	0.035
<b>Head [m]</b>	0	3.496901	13.9876	31.47211	55.95041	87.42252	125.8884	171.3481

Scaled data calculated using the affinity laws based of the PUMPAL performance data for the full scale impeller.

## **APPENDIX E**

### **Experimental Data and Calculations**



**Appendix E-1: MATLAB code used to calculate and plot the experimental suction performance data.**

```

% Calculates and plots suction performance test results

% Imports experimental data

[data] = xlsread('C:\Users\208504902\Desktop\Cavitation
Test\Cavitation Test\AllResults.xlsx');

% Sets up result arrays

NPSH = zeros(20,7);

TDHb = NPSH;

TDHh = NPSH;

CavNo = NPSH;

% Constants

rho = 998;

g = 9.81;

D1 = 0.15;

D2 = 0.125;

% Calculates pipe areas

A1 = (pi/4)*(D1^2);

A2 = (pi/4)*(D2^2);

% Sets up trendline arrays

Ah = zeros(45,2);

Bh = Ah;

Ch = Ah;

Dh = Ah;

Eh = Ah;

Fh = Ah;

Gh = Ah;

% Sets up NPSH3% line

NPSHr(1,1) = 0;

NPSHr(1,2) = 13.386;

NPSHr(2,1) = 13;

NPSHr(2,2) = 13.386;

```

```

% Calculates TDH in bar

k = 0;
for i = 1 : 7
for j = 1 : 20
TDHb(j,i) = (data(j,k+2)+(rho/200000)*((data(1,k+4)^2)...
            *(1/(A2^2)-1/(A1^2))))*(1450^2)/((data(j,k+5))^2);
end
        k = k + 6;
end

% Calculates TDH in meters

k = 0;
for i = 1 : 7
for j = 1 : 20
TDHh(j,i) = ((data(j,k+2)*100000)/(rho*g)+((data(1,k+4)^2)...
            *(1/(A2^2)-1/(A1^2))))/(2*g))*(1450^2)/((data(j,k+5))^2);
end
        k = k + 6;
end

% Calculates NPSH

k = 0;
for i = 1 : 7
for j = 1 : 20
Pv = VapourPressure(data(j,k+3));
NPSH(j,i) = (data(j,k+1)*100000)/(rho*g)...
            + (((data(1,k+4))/A1)^2)/(2*g) - Pv/(rho*g);
end
        k = k + 6;
end

% Calculates cavitation number

k = 0;
for i = 1 : 7
for j = 1 : 20

```

```

Pv = VapourPressure(data(j,k+3));
CavNo(j,i) = ((data(j,k+1)*100000) - Pv)/...
            (0.5*rho*(pi*D1*(data(j,k+5))/60)^2));
end
    k = k + 6;
end
% Calculates trend line based on coefficients calculate by MATLAB
k = 2;
for i = 1 : 45
    Ah(i,1) = k;
    Ah(i,2) = (-2.6563e-006)*(k^6)+(0.00046105)*(k^5)+(-
0.01777)*(k^4)...
            +(0.29422)*(k^3)+(-2.4034)*(k^2)+(9.5262)*k+(-0.77105);
    Bh(i,1) = k;
    Bh(i,2) = (1.0838e-005)*(k^7)+(-
0.00068088)*(k^6)+(0.018007)*(k^5)...
            +(-0.25924)*(k^4)+(2.1842)*(k^3)+(-10.702)*(k^2)+(28.089)*k+(-
16.559);
    Ch(i,1) = k;
    Ch(i,2) = (2.2341e-006)*(k^7)+(-
0.00020164)*(k^6)+(0.0067007)*(k^5)...
            +(-0.11132)*(k^4)+(1.0139)*(k^3)+(-
5.0833)*(k^2)+(13.048)*k+(0.51766);
    Dh(i,1) = k;
    Dh(i,2) = (-9.6348e-005)*(k^6)+(0.0048243)*(k^5)+(-
0.096641)*(k^4)...
            +(0.98428)*(k^3)+(-5.337)*(k^2)+(14.582)*k+(-1.7807);
    Eh(i,1) = k;
    Eh(i,2) = (0.00014504)*(k^5)+(-
0.0060459)*(k^4)+(0.096883)*(k^3)...
            +(-0.74986)*(k^2)+(2.8417)*k+(9.9268);
    Fh(i,1) = k;
    Fh(i,2) = (-2.8117e-005)*(k^6)+(0.0015246)*(k^5)+(-
0.033058)*(k^4)...
            +(0.36601)*(k^3)+(-2.1808)*(k^2)+(6.6494)*k+(5.9582);
    Gh(i,1) = k;

```

```

Gh(i,2) = (0.00028955) * (k^5) + (-0.012394) * (k^4) + (0.20333) * (k^3) ...
          + (-1.5901) * (k^2) + (5.9128) * k + (5.7112);
k = k + 0.25;
end

% Plots pressure rise versus inlet pressure for various flow rates
figure(1)
clf
subplot(4,2,1)
plot(data(1:20,1),TDHb(1:20,1),'p')
axis([0 1.5 1.1 1.45])
subplot(4,2,2)
plot(data(1:20,7),TDHb(1:20,2),'p')
axis([0 1.5 1.1 1.45])
subplot(4,2,3)
plot(data(1:20,13),TDHb(1:20,3),'p')
axis([0 1.5 1.2 1.45])
subplot(4,2,4)
plot(data(1:20,19),TDHb(1:20,4),'p')
axis([0 1.5 1.2 1.45])
subplot(4,2,5)
plot(data(1:20,25),TDHb(1:20,5),'p')
axis([0 1.5 1.2 1.45])
subplot(4,2,6)
plot(data(1:20,31),TDHb(1:20,6),'p')
axis([0 1.5 1.2 1.45])
subplot(4,2,7)
plot(data(1:20,37),TDHb(1:20,7),'p')
axis([0 1.5 1.2 1.45])

% Plots head rise versus NPSH for various flow rates
figure(2)
clf
subplot(4,2,1)

```

```

plot(NPSH(1:20,1),TDHh(1:20,1),'p')
axis([0 13 12.5 14.5])
subplot(4,2,2)
plot(NPSH(1:20,2),TDHh(1:20,2),'p')
axis([0 13 12.5 14.5])
subplot(4,2,3)
plot(NPSH(1:20,3),TDHh(1:20,3),'p')
axis([0 13 12.5 14.5])
subplot(4,2,4)
plot(NPSH(1:20,4),TDHh(1:20,4),'p')
axis([0 13 12.5 14.5])
subplot(4,2,5)
plot(NPSH(1:20,5),TDHh(1:20,5),'p')
axis([0 13 12.5 14.5])
subplot(4,2,6)
plot(NPSH(1:20,6),TDHh(1:20,6),'p')
axis([0 13 12.5 14.5])
subplot(4,2,7)
plot(NPSH(1:20,7),TDHh(1:20,7),'p')
axis([0 13 12.5 14.5])
% Plots head rise trendline versus NPSH with NPSH3% line
figure(3)
clf
subplot(4,2,1)
plot(Ah(1:45,1),Ah(1:45,2),NPSHr(1:2,1),NPSHr(1:2,2))
axis([0 13 11 14.7])
subplot(4,2,2)
plot(Bh(1:45,1),Bh(1:45,2),NPSHr(1:2,1),NPSHr(1:2,2))
axis([0 13 12.8 14.5])
subplot(4,2,3)
plot(Ch(1:45,1),Ch(1:45,2),NPSHr(1:2,1),NPSHr(1:2,2))
axis([0 13 13 14.5])

```

```

subplot(4,2,4)
plot(Dh(1:45,1),Dh(1:45,2),NPSHr(1:2,1),NPSHr(1:2,2))
axis([0 13 13 14.5])
subplot(4,2,5)
plot(Eh(1:45,1),Eh(1:45,2),NPSHr(1:2,1),NPSHr(1:2,2))
axis([0 13 13 14.5])
subplot(4,2,6)
plot(Fh(1:45,1),Fh(1:45,2),NPSHr(1:2,1),NPSHr(1:2,2))
axis([0 13 13 14.5])
subplot(4,2,7)
plot(Gh(1:45,1),Gh(1:45,2),NPSHr(1:2,1),NPSHr(1:2,2))
axis([0 13 13 14.5])
% Plots vibration versus NPSH for various flow rates
figure(4)
clf
subplot(4,2,1)
plot(NPSH(1:20,1),data(1:20,6),'p')
axis([0 15 0 3.5])
subplot(4,2,2)
plot(NPSH(1:20,2),data(1:20,12),'p')
axis([0 15 0 3.5])
subplot(4,2,3)
plot(NPSH(1:20,3),data(1:20,18),'p')
axis([0 15 0 3.5])
subplot(4,2,4)
plot(NPSH(1:20,4),data(1:20,24),'p')
axis([0 15 0 3.5])
subplot(4,2,5)
plot(NPSH(1:20,5),data(1:20,30),'p')
axis([0 15 0 3.5])
subplot(4,2,6)
plot(NPSH(1:20,6),data(1:20,36),'p')

```

```

axis([0 15 0 3.5])

subplot(4,2,7)

plot(NPSH(1:20,7),data(1:20,42),'p')

axis([0 15 0 3.5])

```

---

**Appendix E-2: MATLAB code used to calculate and plot the time and frequency domain noise signals.**

```

% Defines the number of samples and sampling time

s = 40000;

t = 2;

samples = s*t;

% Imports noise signal with no cavitation

[audiodataNF1] =
xlsread('C:\Users\208504902\Desktop\Dissertation\Chapter
5\Calculations\5\NF\audio1.xlsx');

TNF1 = audiodataNF1(1:samples,1);

SNF1 = audiodataNF1(1:samples,2);

[audiodataLP1] =
xlsread('C:\Users\208504902\Desktop\Dissertation\Chapter
5\Calculations\5\LP\audio1.xlsx');

TLP1 = audiodataLP1(1:samples,1);

SLP1 = audiodataLP1(1:samples,2);

[audiodataBP1] =
xlsread('C:\Users\208504902\Desktop\Dissertation\Chapter
5\Calculations\5\BP\audio1.xlsx');

TBP1 = audiodataBP1(1:samples,1);

SBP1 = audiodataBP1(1:samples,2);

[audiodataHP1] =
xlsread('C:\Users\208504902\Desktop\Dissertation\Chapter
5\Calculations\5\HP\audio1.xlsx');

THP1 = audiodataHP1(1:samples,1);

SHP1 = audiodataHP1(1:samples,2);

% Imports noise signal at cavitating conditions

[audiodataNF2] =
xlsread('C:\Users\208504902\Desktop\Dissertation\Chapter
5\Calculations\5\NF\audio5.xlsx');

TNF2 = audiodataNF2(1:samples,1);

```

```

SNF2 = audiodataNF2(1:samples,2);

[audiodataLP2] =
xlsread('C:\Users\208504902\Desktop\Dissertation\Chapter
5\Calculations\5\LP\audio5.xlsx');

TLP2 = audiodataLP2(1:samples,1);

SLP2 = audiodataLP2(1:samples,2);

[audiodataBP2] =
xlsread('C:\Users\208504902\Desktop\Dissertation\Chapter
5\Calculations\5\BP\audio5.xlsx');

TBP2 = audiodataBP2(1:samples,1);

SBP2 = audiodataBP2(1:samples,2);

[audiodataHP2] =
xlsread('C:\Users\208504902\Desktop\Dissertation\Chapter
5\Calculations\5\HP\audio5.xlsx');

THP2 = audiodataHP2(1:samples,1);

SHP2 = audiodataHP2(1:samples,2);

% Plots time domain signal

figure(1)

clf

subplot(2,2,1)

plot(TNF1,SNF2,TNF1,SNF1)

subplot(2,2,2)

plot(TNF1,SLP2,TNF1,SLP1)

subplot(2,2,3)

plot(TNF1,SBP2,TNF1,SBP1)

subplot(2,2,4)

plot(TNF1,SHP2,TNF1,SHP1)

% Calculates the FFT of each signal

SfNF1 = fft(SNF1);

SfLP1 = fft(SLP1);

SfBP1 = fft(SBP1);

SfHP1 = fft(SHP1);

SfNF2 = fft(SNF2);

SfLP2 = fft(SLP2);

SfBP2 = fft(SBP2);

SfHP2 = fft(SHP2);

```



```

% Sets up frequency axis
f = s/samples*(0:samples/2-1);

% Calculates the power spectrum
PSfNF1 = SfNF1.*conj(SfNF1)/samples;
PSfLP1 = SfLP1.*conj(SfLP1)/samples;
PSfBP1 = SfBP1.*conj(SfBP1)/samples;
PSfHP1 = SfHP1.*conj(SfHP1)/samples;
PSfNF2 = SfNF2.*conj(SfNF2)/samples;
PSfLP2 = SfLP2.*conj(SfLP2)/samples;
PSfBP2 = SfBP2.*conj(SfBP2)/samples;
PSfHP2 = SfHP2.*conj(SfHP2)/samples;

% Plots the difference in power spectrums for the two cavitation
conditions
figure(2)
clf
subplot(2,2,1)
plot(f,PSfNF2(1:samples/2)-PSfNF1(1:samples/2))
subplot(2,2,2)
plot(f,PSfLP2(1:samples/2)-PSfLP1(1:samples/2))
subplot(2,2,3)
plot(f,PSfBP2(1:samples/2)-PSfBP1(1:samples/2))
subplot(2,2,4)
plot(f,PSfHP2(1:samples/2)-PSfHP1(1:samples/2))

% Imports RMS noise levels
[data] = xlsread('C:\Users\208504902\Desktop\Dissertation\Chapter
5\Calculations\5\Matlab\CompleteData.xlsx');

NPSH = zeros(10,1);

% Pipe diameters
D1 = 0.15;
D2 = 0.125;

% Calculates pipe area
A1 = (pi/4)*(D1^2);
A2 = (pi/4)*(D2^2);

% Fluid constants

```

```

rho = 998;
g = 9.81;
% Calculates NPSHa
fori = 1 : 10
Pv = VapourPressure(data(i,6));
NPSH(i,1) = (data(i,1)*100000)/(rho*g)...
            + ((0.005/A1)^2)/(2*g) - Pv/(rho*g);
end
% Sets up head rise trendline array
Dh = zeros(45,2);
% Calculates the head rise trendline
k = 2;
fori = 1 : 45
Dh(i,1) = k;
Dh(i,2) = (-9.6348e-005)*(k^6)+(0.0048243)*(k^5)+(-0.096641)*(k^4)...
          + (0.98428)*(k^3)+(-5.337)*(k^2)+(14.582)*k+(-1.7807);
            k = k + 0.25;
end
% Plots head rise and RMS noise level versus NPSHa
figure(3)
subplot(2,2,1)
plotyy(NPSH(1:10,1),data(1:10,2),Dh(1:45,1),Dh(1:45,2))
subplot(2,2,2)
plotyy(NPSH(1:10,1),data(1:10,3),Dh(1:45,1),Dh(1:45,2))
subplot(2,2,3)
plotyy(NPSH(1:10,1),data(1:10,4),Dh(1:45,1),Dh(1:45,2))
subplot(2,2,4)
plotyy(NPSH(1:10,1),data(1:10,5),Dh(1:45,1),Dh(1:45,2))

```

---

**Appendix E-3: MATLAB code used to calculate and plot the experimental performance,  $NPSH_{3\%}$  and vibration  $NPSH_v$  curves.**

```

% Plots performance curve,  $NPSH_{3\%}$  and vibration results

```

```

% Imports the experimental and supplier performance data

[PC] = xlsread('C:\Users\208504902\Desktop\Dissertation\Chapter
5\Calculations\PumpCurve.xlsx');

% Plots the performance curve results

figure(1)

clf

plot(PC(1:12,1),PC(1:12,2),'p',PC(13:14,1),PC(13:14,2))

axis([0 35 10 15])

% Imports NPSH data

[NPSH] = xlsread('C:\Users\208504902\Desktop\Dissertation\Chapter
5\Calculations\NPSH.xlsx');

% Plots experimental and supplier NPSH3% data

figure(2)

clf

plot(NPSH(1:7,1),NPSH(1:7,2),'p',NPSH(8:11,1),NPSH(8:11,2),'p')

axis([0 260 0 10])

% Plots NPSH3% and vibration data

figure(3)

clf

plot(NPSH(1:7,1),NPSH(1:7,2),'p',NPSH(1:7,1),NPSH(1:7,3),'p')

```

---

**Appendix E-4: MATLAB function used to calculate vapour pressure.**

```

function [Pv] = VapourPressure(T)

% Calculates the vapour pressure of water using the Antoine equation

Pv = 133.3223684211*10^(8.07131-(1730.63/(233.426+T)));

end

```

---

**Table E.1: Pump curve experimental data.**

<b>Flow Rate [m<sup>3</sup>/h]</b>	0.00	4.61	7.89	10.27	13.30	16.61	19.42	22.71	24.96	26.41	29.78	34.83
<b>Head [m]</b>	13.80	13.88	13.84	13.89	13.83	13.95	13.94	13.94	13.82	13.92	13.90	13.88

Table E.2: Supplier and experimental NPSH<sub>3%</sub> and NPSH<sub>r</sub> based on vibration, data.

Flow Rate [m <sup>3</sup> /h]	NPSH <sub>3%</sub>	NPSH <sub>r</sub> Vibration
<b>Experimental Data</b>		
7.2	3.8	8.4
10.8	3	7.9
14.4	2.5	7.8
18	2.5	6.2
21.6	2.4	5.9
25.2	2.5	5.3
28.8	2.6	5.5
<b>KSB Supplier Data</b>		
100	2.3	
150	2.3	
200	3	
250	5	

Table E.3: Suction performance experimental data for 2 l/s.

Data for Suction Performance Test (2 l/s)					
P1 (abs) [bar]	P2 [bar]	TDH [bar]	T1 [°C]	T2 [°C]	Vibration (RMS) [mm/s]
1.380	1.739	1.359	23.049	23.392	0.809
1.367	1.736	1.368	23.904	24.290	0.659
1.330	1.703	1.374	23.922	24.245	0.641
1.228	1.592	1.365	23.168	23.567	0.827
1.097	1.430	1.333	23.217	23.542	0.822
1.082	1.480	1.398	23.888	24.184	0.710
0.970	1.338	1.368	23.861	24.207	0.797
0.928	1.295	1.367	23.337	23.654	0.717
0.876	1.198	1.322	23.359	23.677	0.763
0.856	1.210	1.353	23.415	23.719	0.747
0.702	1.049	1.346	23.469	23.814	1.064
0.702	1.049	1.347	23.814	24.135	1.028
0.627	0.927	1.300	23.502	23.814	1.236
0.502	0.857	1.355	23.563	23.901	1.152
0.444	0.774	1.330	23.778	24.156	1.193
0.406	0.712	1.306	23.650	23.975	1.583
0.289	0.417	1.128	23.752	24.060	1.936
0.281	0.492	1.211	23.674	23.976	1.843
0.270	0.402	1.132	23.715	24.070	2.120
0.269	0.437	1.168	23.724	24.025	2.320

**Table E.4: Suction performance experimental data for 3 l/s.**

<b>Data for Suction Performance Test (3 l/s)</b>					
<b>P1 (abs) [bar]</b>	<b>P2 [bar]</b>	<b>TDH [bar]</b>	<b>T1 [°C]</b>	<b>T2 [°C]</b>	<b>Vibration (RMS) [mm/s]</b>
1.387	1.739	1.352	23.905	24.204	0.684
1.335	1.702	1.366	24.641	24.882	0.793
1.319	1.672	1.353	23.924	24.290	0.705
1.276	1.624	1.348	23.974	24.292	0.781
1.202	1.578	1.376	24.592	24.866	0.816
1.199	1.568	1.370	24.043	24.374	0.788
1.113	1.486	1.372	24.587	24.855	0.769
1.072	1.444	1.373	24.563	24.770	0.877
0.976	1.339	1.363	24.567	24.771	0.944
0.910	1.279	1.369	24.196	24.366	0.785
0.810	1.154	1.344	24.558	24.757	1.177
0.807	1.165	1.358	24.124	24.330	0.772
0.622	0.964	1.342	24.233	24.527	1.328
0.526	0.854	1.328	24.320	24.575	1.248
0.430	0.763	1.334	24.505	24.774	1.302
0.389	0.697	1.309	24.367	24.688	1.697
0.377	0.722	1.345	24.502	24.755	1.475
0.338	0.646	1.308	24.339	24.605	1.469
0.288	0.494	1.205	24.408	24.663	1.771
0.258	0.413	1.156	24.384	24.685	2.003

**Table E.5: Suction performance experimental data for 4 l/s.**

<b>Data for Suction Performance Test (4 l/s)</b>					
<b>P1 (abs) [bar]</b>	<b>P2 [bar]</b>	<b>TDH [bar]</b>	<b>T1 [°C]</b>	<b>T2 [°C]</b>	<b>Vibration (RMS) [mm/s]</b>
1.356	1.717	1.361	23.514	23.730	1.069
1.308	1.680	1.371	23.567	23.806	1.083
1.287	1.666	1.379	23.604	23.743	1.077
1.218	1.598	1.379	23.659	23.879	1.041
1.206	1.581	1.376	24.073	24.303	1.092
1.153	1.518	1.366	23.686	23.886	1.040
1.018	1.393	1.375	24.029	24.258	1.045
1.016	1.392	1.376	23.703	23.918	1.099
0.886	1.258	1.372	23.746	23.959	1.153
0.758	1.111	1.353	24.029	24.236	1.381

0.725	1.080	1.354	23.772	23.998	1.033
0.654	1.004	1.350	23.793	24.059	1.772
0.588	0.919	1.330	24.001	24.200	1.617
0.530	0.874	1.344	23.828	24.075	1.790
0.418	0.748	1.330	24.001	24.219	1.467
0.347	0.675	1.328	23.873	24.135	1.650
0.314	0.637	1.323	23.885	24.098	2.294
0.286	0.617	1.332	23.931	24.208	2.112
0.259	0.531	1.271	23.932	24.171	1.998
0.228	0.472	1.244	23.977	24.202	1.803

**Table E.6: Suction performance experimental data for 5 l/s.**

Data for Suction Performance Test (5 l/s)					
P1 (abs) [bar]	P2 [bar]	TDH [bar]	T1 [°C]	T2 [°C]	Vibration (RMS) [mm/s]
1.366	1.728	1.363	24.009	24.231	1.067
1.281	1.651	1.371	24.059	24.262	1.165
1.239	1.619	1.380	24.568	24.751	1.203
1.217	1.602	1.385	24.117	24.337	1.251
1.147	1.535	1.388	24.134	24.323	1.273
1.108	1.498	1.390	24.553	24.777	1.223
1.081	1.454	1.373	24.164	24.353	1.152
1.048	1.419	1.371	24.189	24.405	1.174
0.867	1.232	1.365	24.236	24.412	1.184
0.781	1.146	1.365	24.252	24.427	1.230
0.761	1.143	1.382	24.543	24.717	1.242
0.620	0.977	1.357	24.323	24.513	1.180
0.553	0.903	1.351	24.496	24.719	1.446
0.549	0.889	1.340	24.282	24.422	2.871
0.473	0.802	1.329	24.362	24.535	2.028
0.454	0.794	1.341	24.406	24.622	1.683
0.299	0.620	1.322	24.418	24.597	2.556
0.287	0.602	1.315	24.492	24.672	2.364

0.267	0.539	1.273	24.449	24.685	2.302
0.230	0.443	1.213	24.456	24.751	2.184

**Table E.7: Suction performance experimental data for 6 l/s.**

Data for Suction Performance Test (6 l/s)					
P1 (abs) [bar]	P2 [bar]	TDH [bar]	T1 [°C]	T2 [°C]	Vibration (RMS) [mm/s]
1.324	1.695	1.370	20.892	21.096	1.216
1.315	1.678	1.363	21.028	21.141	1.261
1.292	1.662	1.370	21.047	21.193	1.188
1.261	1.636	1.376	21.094	21.298	1.237
1.209	1.569	1.360	21.255	21.390	1.155
1.172	1.552	1.380	21.871	22.013	1.289
1.144	1.508	1.364	21.238	21.472	1.180
1.079	1.453	1.374	21.865	21.985	1.321
1.058	1.442	1.384	21.302	21.451	1.218
0.967	1.343	1.376	21.792	21.914	1.289
0.881	1.263	1.382	21.354	21.494	1.227
0.794	1.162	1.368	21.792	21.912	1.233
0.673	1.047	1.374	21.429	21.546	1.256
0.609	0.990	1.382	21.452	21.570	1.014
0.581	0.952	1.371	21.570	21.635	1.116
0.403	0.745	1.341	21.532	21.710	2.057
0.402	0.754	1.352	21.610	21.788	2.571
0.294	0.634	1.339	21.696	21.885	2.564
0.291	0.636	1.345	21.695	21.808	2.798
0.238	0.519	1.282	21.639	21.831	2.855

**Table D.8: Suction performance experimental data for 7 l/s.**

Data for Suction Performance Test (7 l/s)					
P1 (abs) [bar]	P2 [bar]	TDH [bar]	T1 [°C]	T2 [°C]	Vibration (RMS) [mm/s]

1.308	1.672	1.365	20.067	20.183	1.507
1.261	1.629	1.369	20.178	20.205	1.263
1.226	1.583	1.357	20.195	20.277	1.324
1.176	1.535	1.358	20.177	20.320	1.389
1.122	1.483	1.361	20.663	20.849	1.244
1.045	1.404	1.358	20.225	20.344	1.504
0.983	1.357	1.373	20.242	20.386	1.166
0.947	1.318	1.371	20.670	20.774	1.200
0.850	1.212	1.363	20.272	20.423	1.201
0.849	1.214	1.365	20.671	20.753	1.107
0.774	1.134	1.361	20.309	20.445	1.204
0.703	1.069	1.366	20.345	20.466	1.263
0.623	0.989	1.366	20.571	20.749	1.258
0.545	0.907	1.362	20.392	20.491	3.108
0.430	0.787	1.358	20.428	20.547	1.744
0.392	0.741	1.349	20.592	20.707	2.808
0.340	0.686	1.347	20.450	20.627	2.244
0.269	0.582	1.313	20.519	20.647	2.795
0.240	0.514	1.274	20.518	20.661	3.056
0.234	0.506	1.271	20.515	20.697	2.850

**Table D.9: Suction performance experimental data for 8 l/s.**

<b>Data for Suction Performance Test (8 l/s)</b>					
<b>P1 (abs) [bar]</b>	<b>P2 [bar]</b>	<b>TDH [bar]</b>	<b>T1 [°C]</b>	<b>T2 [°C]</b>	<b>Vibration (RMS) [mm/s]</b>
1.283	1.634	1.352	20.043	20.151	1.217
1.261	1.621	1.360	20.085	20.201	1.252
1.225	1.583	1.358	20.132	20.222	1.335
1.165	1.528	1.363	20.204	20.261	1.427
1.108	1.468	1.360	20.216	20.287	1.183
1.062	1.430	1.367	20.205	20.322	1.214
1.020	1.390	1.370	20.253	20.321	1.300
0.959	1.318	1.359	20.266	20.379	1.338



0.820	1.174	1.353	20.299	20.414	1.375
0.814	1.167	1.353	20.651	20.750	1.088
0.797	1.162	1.365	20.343	20.455	1.345
0.712	1.075	1.363	20.326	20.483	1.223
0.661	1.010	1.349	20.612	20.755	1.209
0.628	0.994	1.365	20.392	20.520	1.188
0.544	0.897	1.354	20.471	20.586	3.010
0.476	0.831	1.355	20.481	20.556	2.415
0.426	0.779	1.353	20.606	20.668	2.414
0.390	0.738	1.347	20.537	20.584	3.285
0.309	0.644	1.335	20.594	20.621	2.597
0.247	0.495	1.248	20.606	20.663	3.230